

NOVEL LIGHT TRAPPING AND NONLINEAR DYNAMICS IN
NANOPHOTONIC DEVICES

A Dissertation

Submitted to the Faculty

of

Purdue University

by

Shaimaa I. Azzam

In Partial Fulfillment of the

Requirements for the Degree

of

Doctor of Philosophy

August 2020

Purdue University

West Lafayette, Indiana

THE PURDUE UNIVERSITY GRADUATE SCHOOL
STATEMENT OF DISSERTATION APPROVAL

Dr. Alexander V. Kildishev

School of Electrical and Computer Engineering

Dr. Alexandra Boltasseva

School of Electrical and Computer Engineering

Dr. Vladimir M. Shalaev

School of Electrical and Computer Engineering

Dr. Zubin Jacob

School of Electrical and Computer Engineering

Approved by:

Dr. Dimitrios Peroulis

Head of the School of Electrical and Computer Engineering

To the memory of my father.

ACKNOWLEDGMENTS

I am very grateful for all the opportunities and support I received at Purdue. I would like to start by thanking my advisor, Prof. Alexander Kildishev, for his tremendous help during my PhD journey as well as his continuous support and encouragement. I want to thank my committee member and mentor, Prof. Alexandra Boltasseva, for her endless support and guidance and her valuable advice throughout my time at the nanophotonics group at Purdue. I would also like to thank Prof. Vladimir Shalaev for all the opportunities he has given me and his continuous help and direction. I am thankful to Prof. Zubin Jacob, my committee member and collaborator, for his help and to collaborator Prof. Young Kim for giving me access to his labs and equipment. I particularly want to thank Birck's Nanotechnology center's management, staff, and custodians for all their hard work to make our work as smooth as possible. Special thanks to Mary Jo, Tracy, Brenda, Sheryl, and Olga.

Last but definitely not least, my deep love and sincere appreciation go to my family and friends back home and here at Purdue. To Enas, Amr, Hala, and Mohamed for making me feel part of their families. To Ghada and Nagwa, my sisters and my best friends for their unparalleled love and support. To my parents for all that they have given me and the experiences that made me the person I am today. I am forever grateful for everything they have done for our family. To my husband, my rock and my best friend, Esat, for being there for me in the bad and the good, for all the stimulating discussions we had and for your continuous love, support, and encouragement. I wouldn't want to imagine my PhD journey nor my life without you. And finally to the absolute joy of my life, my dear daughter, Celine, for her miraculous ability to turn my difficult moments to the biggest of smiles, brightening my days, and filling my heart with more happiness than I thought it was capable of. For you, I look forward to tomorrow and the adventures it holds for us.

TABLE OF CONTENTS

	Page
LIST OF FIGURES	viii
ABSTRACT	xi
1 INTRODUCTION	1
1.1 Bound states in the radiation continuum	2
1.2 Atomic multi-level models for nonlinear light-matter interactions	3
2 FORMATION OF BOUND STATES IN THE CONTINUUM IN HYBRID PLASMONIC-PHOTONIC SYSTEMS	6
2.1 Introduction	6
2.2 Results and discussion	8
2.2.1 Quality factors of the BIC resonances	13
2.2.2 Band engineering in the hybridized system	13
2.3 Conclusion	16
3 SINGLE AND MULTI-MODE DIRECTIONAL LASING FROM ARRAYS OF DIELECTRIC NANORESONATORS	17
3.1 Introduction	17
3.2 High-Q resonances in dielectric metasurfaces	17
3.3 Lasing in dielectric metasurfaces	20
3.4 Modal engineering near BIC states	22
3.5 Discussion	28
3.6 Methods	28
3.6.1 Metasurface Fabrication	28
3.6.2 Characterization	30
3.6.3 Lasing measurements	31
3.6.4 FDTD simulations of lasing dynamics	31

	Page
3.7 Conclusion	32
4 EXPLORING TIME-RESOLVED MULTIPHYSICS OF ACTIVE PLAS- MONIC SYSTEMS WITH EXPERIMENT BASED GAIN MODELS	33
4.1 Theoretical models	36
4.1.1 Four-level system	37
4.1.2 Six-level system	39
4.2 Results and discussion	41
4.2.1 Parameters retrieval using film transmission	41
4.2.2 Dynamic processes in the metal nanoholes array with gain . . .	42
4.2.3 Compensation of losses in Kretschmann-Raether configuration .	47
4.3 Conclusions	51
5 TIME DOMAIN DYNAMICS OF REVERSE SATURABLE ABSORBERS WITH APPLICATION TO PLASMON-ENHANCED OPTICAL LIMITERS	52
5.1 Introduction	52
5.2 RSA models	55
5.2.1 Beer-Lambert's law	56
5.2.2 Four-level atomic system	57
5.3 Numerical Details and Results	59
5.3.1 Plasmon-enhanced optical limiters	63
5.4 Conclusion	65
6 TIME-DOMAIN DYNAMICS OF SATURATION OF ABSORPTION US- ING MULTILEVEL ATOMIC SYSTEMS	66
6.1 Introduction	66
6.2 Saturable absorption models	68
6.2.1 Two-level saturable absorption atomic model	69
6.2.2 Four-level saturable absorption atomic model	70
6.3 Results and analysis	71
6.4 Conclusions	75
7 SUMMARY	76

	Page
REFERENCES	78
A Appendix I	89
A.1 Silver optical properties	89
A.2 Numerical details	90
A.3 Nature of supported modes	90
B Appendix II	95
B.1 Nature of the supported modes in the metasurface	95
B.2 Dependence of the Electric Dipole, Magnetic Dipole and the BIC State on the Geometrical Parameters	95
B.3 FDTD simulations of lasing dynamics	96
VITA	107
PUBLICATIONS	109

LIST OF FIGURES

Figure	Page
2.1 BICs due to the coupling of plasmon polaritons with photonic modes . . .	9
2.2 BIC formation in the hybrid plasmonic-photonic system	10
2.3 The avoided crossing and linewidth vanishing due to the hybridization of plasmonic and photonic modes at different angles of incidences.	12
2.4 Quality factor vs. angle of incidence for different BIC types	14
2.5 Band diagrams of the plasmonic grating coupled to waveguides of different thicknesses	15
3.1 High-Q resonances in arrays of dielectric nanoresonators with electric and magnetic dipoles.	21
3.2 Lasing action with near-BIC feedback.	23
3.3 Directionality of the lasing emission.	24
3.4 The simulated reflectance vs. the angle of incidence and wavelength. . . .	26
3.5 Dual-mode lasing action from dielectric arrays.	27
4.1 Scheme of a population transfer process of the four-level (a) and six-level (b) systems for an optically excited dye molecule and the governing rate equations.	39
4.2 Pump-probe experimental setup and saturated transmission results per- formed with pump wavelength at 595 nm	41
4.3 Schematic view of the silver nanoholes array structure covered by R101- PVA film	43
4.4 Evolution of the emission spectra with increasing pumping power	44
4.5 The simulated electric field distribution at different pumping powers at the lasing wavelength	45
4.6 The simulated results of the steady state population inversion distribution	46
4.7 Schematic of the Kretschmann-Raether SPP excitation configuration with the reflectivity at no gain and with gain at different pump energies	48

Figure	Page
4.8 Temporal dynamics of the induced macroscopic polarizations, and the population densities at different levels	50
5.1 RSA physical mechanism and Jablonski diagram	55
5.2 RSA behavior and time dynamics of the four-level system	58
5.3 Effect of triplet quantum yield on the RSA efficiency	61
5.4 Transmittance vs. pump fluence	62
5.5 Enhancement of optical limiters using plasmonic structures	64
6.1 Saturable absorption in a dielectric thin film modeled by a two-level system	67
6.2 Jablonski diagrams of two-level and four-level atomic systems	70
6.3 Dynamics of a dielectric saturable absorber modeled using the two-level system	73
6.4 Dependence of the absorption on the film thickness and carriers' concentrations	74
6.5 A saturable absorber dielectric film modeled using the four-level system . .	74
A.1 Real and imaginary parts of the polycrystalline silver permittivity as a function of the wavelength.	89
A.2 Cross-section of the hybrid plasmonic-photonic structure in the simulation domain.	91
A.3 Band-diagram of the silver grating with extended SiO ₂ top layer.	92
A.4 Band diagram of the hybrid silver grating-silica waveguide system under TM and TE light illumination.	93
A.5 Band-diagram of a TiO ₂ grating on top of a 100-nm silver film coupled to a 500-nm SiO ₂ waveguide under TM and TE illumination.	94
B.1 The simulated reflectance of a metasurface with a radius of 100 nm at normal incidence and the vector plots of the electric field inside a cross-section of the nanoresonator at the different reflectance dips.	98
B.2 Nature of electromagnetic fields at the different modes supported by the metasurface.	99
B.3 Simulated reflectance spectra of the metasurface with an array periodicity of 400 nm vs. the resonator height.	100
B.4 Transmittance of three samples with R_{cyl} of 85, 90 and 95 nm at normal incidence.	101

Figure	Page
B.5 Jablonski diagram of a four-level gain medium. Solid lines indicate stimulated transmissions (absorption and emission) and dashed lines represent non-radiative transitions.	102
B.6 Schematic showing the different steps of the fabrication process of the metasurfaces.	103
B.7 Schematic of the experimental setup used to collect the lasing emission from the metasurface samples.	104
B.8 Back focal plane images at analyzer angles of (a) 0° , (b) 30° , (c) 60° and (d) 90°	105
B.9 Triple-mode lasing with a BIC metasurface feedback showing three lasing peaks at 612.9 nm, 616.2 nm, and 624.4 nm alongside the evolution of each lasing peak with the pump fluence showing a sharp threshold behavior for each lasing wavelength.	106

ABSTRACT

Azzam, Shaimaa I. Ph.D., Purdue University, August 2020. Novel Light Trapping and Nonlinear Dynamics in Nanophotonic Devices . Major Professors: Alexander V. Kildishev.

Numerous fundamental quests and technological advances require trapping light waves. Generally, light is trapped by the absence of radiation channels or by forbidding access to them. Unconventional bound states of light, called bound states in the continuum (BICs), have recently gained tremendous interest due to their peculiar and extreme capabilities of trapping light in open structures with access to radiation. A BIC is a localized state of an open structure with access to radiation channels, yet it remains highly confined with, in theory, infinite lifetime and quality factor. There have been many realizations of such exceptional states in dielectric systems without loss. However, realizing BICs in lossy systems such as those in plasmonics remains a challenge. This thesis explores the realization of BICs in a hybrid plasmonic-photonic structure consisting of a plasmonic grating coupled to a dielectric optical waveguide with diverging radiative quality factors. The plasmonic-photonic system supports two distinct groups of BICs: symmetry protected BICs and Friedrich-Wintgen BICs. The photonic waveguide modes are strongly coupled to the gap plasmons in the grating leading to an avoided crossing behavior with a high value of Rabi splitting of 150 *meV*. Additionally, it is shown that the strong coupling significantly alters the band diagram of the hybrid system, revealing opportunities for supporting stopped light at an off- Γ wide angular span.

In another study, we demonstrate the design of a BIC-based all-dielectric metasurface and its application as a nanolaser. Metasurfaces have received an ever-growing interest due to their unprecedented ability to control light using subwavelength struc-

tures arranged in an ultrathin planar profile. However, the spectral response of metasurfaces is generally broad, limiting their use in applications requiring high quality (Q) factors. In this study, we design, fabricate, and optically characterize metasurfaces with very high Q-factors operating near the BIC regime. The metasurfaces are coated with an organic lasing dye as an active medium, and their lasing action is experimentally characterized. The proposed BIC-based metasurfaces nanolaser have very favorable characteristics including low threshold, easily tunable resonances, polarization-independent response, and room temperature operation.

The second part of the thesis deals with the nonlinear phenomenon in nanophotonic structures. We developed an advanced full-wave framework to model nonlinear light-matter interactions. Rate equations, describing atomic relaxations and excitation dynamics, are coupled to the Maxwell equations using a Lorentzian oscillator that models the kinetics-dependent light-matter interaction in the form of averaged polarization. The coupled equations are discretized in space and time using a finite-difference time-domain method that provides a versatile multiphysics framework for designing complex structures and integrating diverse material models. The proposed framework is used to study gain dynamics in silver nanohole array, reverse saturable absorption dynamic in optical limiters, and saturable absorption in random lasers. This framework provides critical insights into the design of photonic devices and their complementary optical characterization, and serve as an invaluable utility for guiding the development of synthetic materials. It allows accurate physics-based numerical modeling and optimization of the devices with complex micro- and nano-structured materials and complex illumination sources such as non-paraxial structured beams.

1. INTRODUCTION

This dissertation discusses two independent, yet correlated, topics in the field of optics and photonics. The first part of this dissertation deals with the trapping of light waves in nanophotonic structures using what is known as bound states in the continuum (BICs). Trapping of electromagnetic waves in general, and light waves in particular, has always been of great interest due to the numerous fundamental as well as technological advantages. Fields like lasers, quantum electrodynamics, sensors, spectral filtering, and many more rely heavily on high quality (Q) resonances at which light can be confined in a "cavity" for an extended time. The discovery of bound states in the continuum or high-Q resonances that don't necessarily live in regular cavities have been revolutionizing in many areas of science. A little over a decade ago, the concepts of BICs have been introduced in photonic systems and have found an immense interest and a wide variety of applications due to the flexibility they provide in cavity design.

The second part of this dissertation deals with the numerical modeling of light-matter interaction in nonlinear materials. Most light-matter interactions are linear and can be captured using the dielectric function of the material. However, as the intensity of light increases, either externally or through enhancing light localization, nonlinear phenomenon starts to emerge. This part of the dissertation elaborates on the computational framework that we developed to provide physics-based nonlinear material models. It provides a comprehensive understanding of the dynamics of nonlinear interactions of light with photonic systems. This framework offers critical insights into the design of transformative photonic devices and their complementary optical characterization. It also serves as an invaluable utility for guiding the development of synthetic absorbing materials.

1.1 Bound states in the radiation continuum

Bound states in the continuum (BICs) are localized state of the wave equation that coexist with the radiation continuum. However, BICs remain highly localized with theoretically infinite quality factors. With any deviation from the ideal system, the BIC would collapse to a Fano resonance with a finite lifetime – a regime known as quasi-BIC [1,2]. This is generally the states realizable practically since, in theory, true BICs can only be achieved in systems with at least one dimension extending to infinity [2]. If the Hamiltonian describing the system differs slightly from the one which would produce a BIC, a sharp resonance arises in all scattering and reaction cross-sections, which is known as “near-BIC” state [3–5]. The near-BIC regime’s central advantages are that, unlike regular guided modes below the light-line, the modes in this regime can be excited by free propagating plane waves. Moreover, near-BIC resonances have very high Q factors. They can be obtained throughout the continuous parameter values, in contrast to BICs, which are generally achieved at a single value of the parameter. This provides stability to fabrication tolerances and other imperfections [1].

So far, the majority of realizations of BICs are in dielectric systems [6–11]. The proposals for realizing BICs in systems with losses such as plasmonics have been limited to either working at the limit of vanishing metal losses [12] or compensating the losses with gain from an active medium [11]. In this thesis, I explore the formation of BICs in a hybrid plasmonic-photonic structure with realistic material loss. In Chapter 2, I show that a silver grating coupled to a photonic waveguide can support two distinct types of BICs: symmetry-protected BICs, and Friedrich-Wintgen BIC. The symmetry protected states arise due to incompatibility with the radiation leading to the decoupling and hence the localization of the state. Friedrich-Wintgen BICs appear at off- Γ locations due to destructive interference of the resonances at the right phase-matching conditions [13]. An apparent strong coupling behavior is observed in the system between the plasmonic and the photonic modes manifested in the avoided

resonances crossing with a large Rabi splitting. This is a signature of the hybridization of the plasmon polaritons and the optical waveguide mode leading to the formation of a new polaritonic-optical quasi-particle [14,15] as well as the BIC. I believe that these hybrid structures are great platforms for many applications that would benefit from high-field localization and the extreme quality factors such as low-threshold lasers, sharp spectral filters, enhancement of nonlinear phenomena, and sensors.

In a different project, I study the lasing action in dielectric metasurfaces consisting of nanoresonators based on BICs. One of the current prominent fields of applications of BICs is the enhancement of nonlinear light-matter interactions near the BIC points. This has the potential to bring the advantages of BIC states to many fields, including all-optical and quantum computing. However, until now, the experimental realization of bound states in the continuum in the visible regime has been quite limited.

In Chapter 2, I report on the experimental realization of BICs in the visible in an all-dielectric metasurface. It is demonstrated that high-quality factor resonances can be achieved in dielectric metasurfaces using a simplistic unit cell consisting of only a single resonator. The locations of the resonances are tunable by geometrical design through controlling the metasurface periodicity.

Utilizing the high-quality factor resonance near BICs, I demonstrate a low-threshold, room-temperature lasing action in dielectric resonators in the visible wavelength range. The generated lasing emission shows highly directional spatial patterns. I also experimentally investigate mode engineering in all-dielectric metasurfaces and demonstrate multi-wavelength, directional lasing.

1.2 Atomic multi-level models for nonlinear light-matter interactions

Modeling of the nonlinear phenomena has primarily relied on the perturbation theory to extend the linear response to account for nonlinearities [16]. This is a very powerful approach that enabled the solution of many nonlinear processes. However, with the increasing advances in nonlinear materials and unprecedented increase in

the strength of nonlinear interactions [17, 18], the perturbation theory is no longer able to provide an adequate description for nonlinearities [17, 19, 20].

In this thesis, I developed an advanced full-wave numerical model for nonlinear light-matter interaction in the time-domain. The model couples the rate equations, describing the atomic excitation and relaxations, with the Maxwell equations describing the electromagnetic field. A full spatiotemporal picture of the nonlinear dynamics in photonic devices can be obtained using this model. The presented novel technique provides a versatile multiphysics framework for designing complex structures and integrating diverse material models that were not previously possible.

In Chapter 4, the atomic multi-level system is used to systematically investigate lasing, and net amplification in plasmonic structures with a finite-difference time-domain method (FDTD) coupled to the rate equations of four-level and six-level atomic systems. I used experimentally-based kinetic parameters as input to our model to study the mechanism of the coupling of metamaterials and metasurfaces with the gain medium. With the help of such an accurate model, net amplification, and time-resolved lasing dynamics for the plasmonic systems coupled with gain can be clearly distinguished. The lasing emission characteristics and threshold behavior for the nanoholes array system predicted by the model are in excellent agreement with the experiment. The simulations further reveal the temporal details of the energy transfer process in the lasing regime. Such detailed and accurate models are necessary for understanding, predicting, and designing new types of nanoscale lasers and gain-compensated plasmonic systems.

In Chapter 5, I present a time-domain model for reverse saturable absorbers using the same multiphysics framework. This approach allows us to capture the behavior of the reverse saturable absorber materials embedded in artificial photonic nanostructures that cannot be analyzed with established techniques such as the Beer-Lambert's Law. To showcase the importance of the full-wave reverse saturable absorbers analysis coupled to carrier kinetics, I examine two plasmon-enhanced optical limiters: a metal grating and a Fabry-Perot cavity-like structure where the unenhanced limiter

threshold can be decreased by a factor of 3 and 13, respectively. This is a promising approach for developing reverse saturable absorbers devices that can operate at reduced illumination levels, and hence, significantly expand their applicability.

Chapter 6 deals with the application of the atomic multi-level system to the modeling of saturable absorbers. Due to the importance of saturable absorbers in passive mode-locking [21] and Q-switching [22] to generate ultrashort laser pulses, accurate models describing the saturable absorption in the time domain are imperative to the development of these devices. I used the proposed multi-level approach to explore the saturation of absorption as the interplay of the carrier population kinetics in a multi-level atomic system with classical electromagnetic fields. The proposed methodology offers the ability to model multiple absorption peaks based on the material spectral response. This framework could enable a further comprehensive understanding of the foundations of the materials physics and empower accurate optimization of future nonlinear photonic devices.

In Chapter 7, I will conclude and provide some future direction to the research carried out so far in this thesis. The materials presented in the chapters of this thesis are mostly adopted from our papers published on the respective topics [5, 23–25].

2. FORMATION OF BOUND STATES IN THE CONTINUUM IN HYBRID PLASMONIC-PHOTONIC SYSTEMS

2.1 Introduction

In 1929, von Neumann and Wigner predicted the existence of localized eigenstates of the single-particle Schrödinger equation embedded in the continuum of eigenvalue state solutions, now known as embedded eigenstates or bound states in the continuum (BICs) [26]. Later, there have been many explanations for the formation mechanisms leading to the different types of BICs, including symmetry-incompatibility [10,27,28], and destructive interference of resonances [2,29–32]. According to Friedrich and Wintgen, when two resonances pass each other as a function of a continuous parameter, the two channels interfere, resulting in an avoided crossing of their resonances. Typically, at a given value of the continuous parameter, one of the channels vanishes entirely, becoming a BIC with an infinite quality (Q) factor [13]. With any perturbation in the ideal system, the BIC would collapse to a Fano resonance with a finite lifetime – a regime known as quasi-BIC [1,2]. Generally, practical realizations are limited to the quasi-BIC regime as, theoretically, true BICs can only be achieved in systems with at least one dimension extending to infinity [2].

Another imperative regime is the so-called “near-BIC” at which very high Q factors are still attainable in the vicinity of the BIC. These high-Q resonances can be explained using the Theory of Resonance Reactions by Fonda [3,4]; a bound state can exist in the continuum at an energy where some channels are open even when the open and closed channels are strongly coupled. If the actual Hamiltonian dif-

This chapter is based on S. I. Azzam, V. M. Shalaev, A. Boltasseva, and A. V. Kildishev, “Formation of bound states in the continuum in hybrid plasmonic-photonic systems,” *Physical Review Letters*, vol. 121, no. 25, p. 253901, 2018, and is reproduced with publisher’s permissions.

fers inconsiderably from the one which would produce such a bound state, a sharp resonance arises in all scattering and reaction cross-sections. Central advantages of the near-BIC regime are that, unlike regular guided modes below the light-line, the modes in this regime can be excited by free propagating plane waves. Moreover, near-BIC resonances can be obtained throughout the continuous parameter values, in contrast to BICs, which are generally achieved at a single value of the parameter. This provides stability to fabrication tolerances and other imperfections [1].

BICs in photonic systems were realized for the first time in 2008 [33], and since then, there has been growing interest in their implementations as well as practical applications [7, 10, 34–44]. There have been numerous realizations of BICs in dielectric systems [6–11, 45]. However, metallic structures that support BICs have remained limited due to their intrinsic losses [11]. Proposals for realizing BICs in systems with metallic components have been restricted to either working at the limit of vanishing metal losses [12] or compensating the losses with gain from an active medium [11]. Very recently, the realization of BICs in hybrid transition metal dichalcogenides and a dielectric photonic crystal slab has been studied [46]. Extensive efforts have been made to realize high-Q plasmonic systems [47–49, 49, 50]. Plasmonic cavities with relatively high Q factors have been achieved based on defect modes [50], collective plasmon resonances [48], metallic trench Fabry-Perot resonator [51], high aspect ratio metallic mirrors [52], or plasmonic nanocavities [53]. However, the demonstrated Q factors of the plasmonic cavities have thus far been limited to a few hundred due to both the radiation and metallic losses.

In this work, the radiative losses in plasmonic structures have been eliminated by the careful design of a structure that strongly couples surface plasmon polaritons to photonic modes to form BICs [5, 54]. The two interacting channels in the system are: the photonic modes of a dielectric slab waveguide and the plasmonic modes supported by a one-dimensional (1D) periodic silver grating, Fig. 2.1(a). When the two channels strongly couple, two distinct features can be observed. First, an avoided crossing of the two angular dispersion lines with a reasonably large Rabi splitting – a signature

of the strong coupling between the modes leading to the formation of a polaritonic-optical quasi-particle [14, 15]. Second, the vanishing of one of the spectral lines at a specific angle of illumination – a distinct feature of the BIC formation caused by the destructive interference of the resonances.

2.2 Results and discussion

A schematic of the resonances' interactions is depicted in Fig. 2.1(b). The unperturbed resonances of the plasmonic (blue) and photonic (red) modes are shown as dotted lines, while the hybrid system's coupled modes are depicted as solid lines. The angular dispersion of surface plasmons excited on the surface of the grating is a result of a hybridization of the classical surface plasmon-polariton with a plasmonic grating. Subsequently, a bandgap opens up at a wavelength determined by the grating periodicity [55]:

$$\kappa_{sp} = \frac{2\pi n_{\text{eff}}}{\lambda_0} = \frac{2\pi}{\lambda_0} \sin \theta \pm \frac{2\pi m}{\Lambda}, \quad (m = 0, 1, \dots) \quad (2.1)$$

where κ_{sp} is the momentum of the surface plasmon, λ_0 is the free space wavelength, n_{eff} is the effective refractive index of the plasmonic mode, θ is the angle of incidence, Λ is the grating pitch, and m is the grating diffraction order.

Likewise, the hybridization of the dielectric slab waveguide with the grating results in the excitation of the photonic modes with a narrow spectral width [56]. Overall, the hybrid system supports two distinct types of BICs: symmetry-protected and Friedrich-Wintgen BICs. The former appears at the Γ -point at normal incidence due to the symmetry incompatibility with the outgoing fields, leading to the decoupling from the free-space propagating waves and hence the localization of the state. We denote the BIC originating from the symmetry of the plasmonic modes as symmetry-protected plasmonic BIC, while that arising from the symmetry of the photonic modes as symmetry-protected photonic BIC. Friedrich-Wintgen BIC appears at an off- Γ point due to destructive interference of the resonances at the correct

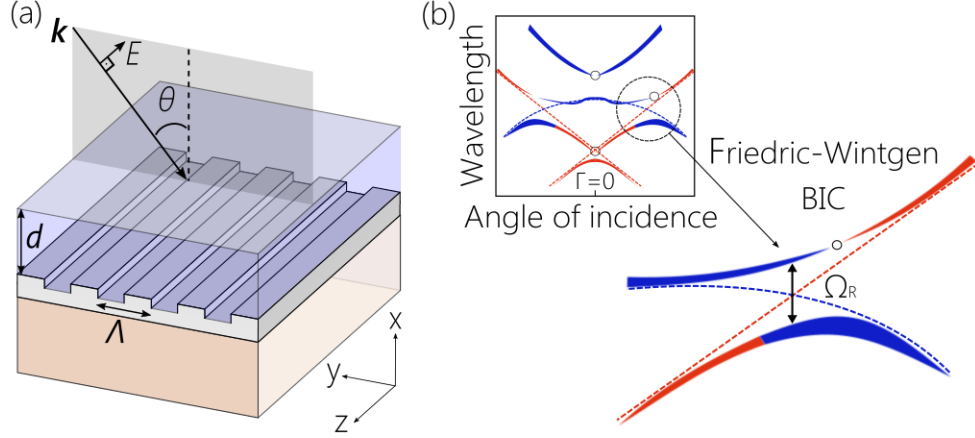


Fig. 2.1. BICs due to the coupling of plasmon polaritons with photonic modes. (a) A hybrid plasmonic-photonic structure with a silver grating (pitch $\Lambda = 400$ nm) coupled to a SiO_2 slab (thickness $d = 500$ nm). The periodic ridges of the grating are 30-nm high and 100-nm wide. The back silver film is 100-nm thick. (b) A sketch of the band structures of the hybrid system with coupled plasmonic (blue) and photonic (red) resonances. Dotted lines indicate the unperturbed resonances, and solid ones are the coupled resonances. Small circles show the BIC points, and the large dotted circle highlights the strong coupling with Rabi splitting (Ω_R) and showing the off- Γ Friedrich-Wintgen BIC.

phase-matching conditions [13]. This type of bound states is also sometimes referred to as an “accidental” BIC [8]. In the absence of strong coupling, the dispersion of the photonic and the plasmonic modes will merely cross each other at a particular angular position. However, due to the strong coupling of the modes, an avoided resonance crossing is observed with a Rabi splitting Ω_R , Fig. 2.1(b). This is a signature of the hybridization of the plasmon polaritons and the optical waveguide mode leading to the formation of a new polaritonic-optical quasi-particle [14, 15] as well as the BIC. An essential characteristic of the Friedrich-Wintgen BIC achieved in the proposed structure is that it originates from the interference of two resonances with different natures, namely a photonic mode and a plasmon polaritons. This provides high flexibility in the engineering of the resonances’ dispersion enabling high control on their spectral positions, angular span, and linewidth.

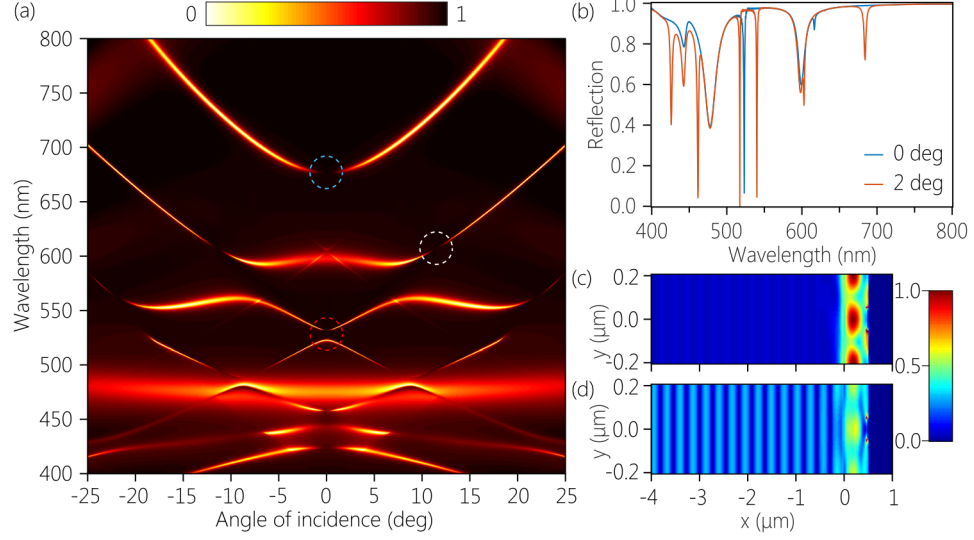


Fig. 2.2. BIC formation in the hybrid plasmonic-photonic system. (a) Reflection spectrum as a function of the angle of incidence (band diagram) of the coupled system. BICs are highlighted by dotted circles showing two symmetry protected BICs due to plasmonic (blue) and photonic (red) modes and Friedrich-Wintgen BIC due to the interference of plasmonic and photonic resonances (white). (b) Cross-sections of the reflection coefficient at 0° and 2° incidence angles show the appearance of the collapsed symmetry protected BICs to sharp Fano resonances. Blue and red arrows point to the plasmonic and the photonic collapsed symmetry-protected BICs. Normalized electric fields at 2° at (c) 540.2 nm (at the resonance) and (d) 541.2 nm (1 nm away from the resonance) showing the field localization.

The proposed structure is composed of a silver grating (with pitch $\Lambda = 400$ nm) on top of a silica glass substrate coupled to a silicon dioxide (SiO_2) slab with thickness $d = 500$ nm. The geometrical parameters are selected to ensure the spectral overlap of the plasmonic resonances and the photonic modes to achieve coupling. The periodic ridges of the grating are 30-nm high and 100-nm wide while the back silver film is 100-nm thick. The dielectric constant of SiO_2 is fixed at 2.25, and the permittivity of the silver is taken from ellipsometric measurement (see details in Appendix I). The simulated reflection spectrum as a function of the angle of incidence (band diagram) is presented in Fig. 2.2(a). We use the finite difference time domain method for

calculating band diagrams and electromagnetic fields. More details on the numerical simulations and the simulation domain can be found in Appendix I.

In this dissertation, BICs are described as features of the transmission spectrum at certain angles (wavevectors). However, it is worth mentioning that BICs are the eigensolutions to the source-free Maxwell equations characterized by real eigenvalues above the lightline [57]. Therefore, the angle of incidence is not associated with a source, but rather with the wavevector in the solution. The symmetry-protected plasmonic and photonic BICs are shown in Fig. 2.2(a) inside blue and red dotted circles, respectively. Both BICs appear at the normal incidence. More notably, the Friedrich-Wintgen BIC, inside a white circle, resulting from the interference and the strong coupling of the photonic and the plasmonic modes, appears at 11.4° angle of incidence. The calculated reflection coefficients are plotted at angles 0° and 2° , Fig. 2.2(b), demonstrating the noticeable and sudden appearance of sharp Fano resonances when moving away from the symmetry-protected BIC. This is a clear manifestation of the theory of resonances when operating at the near-BIC regime [3,4]. Also, vertical cross-sections of the electric field at the near-BIC point at 540.2 nm at 2° is shown in Fig. 2.2(c) to verify in-plane light confinement. The localization of the field inside the dielectric layer and minimal radiation is visible even with available access to the radiation channels. However, even a small deviation (by just 1 nm) from the near-BIC resonance of Fig. 2.2(d) would result in significant radiation to the air and nearly one order of magnitude drop in the max field enhancement (not shown).

The ability to confine and enhance light at the near-BIC is very crucial for enhancing light-matter interaction. However, more importantly, light confined at this regime, unlike regular guided modes below the light-line, can be excited by the free propagating plane wave. The reflection coefficients at selected angles of incidence are scaled and plotted in Fig. 2.3 illustrates the avoided crossing between the hybridized plasmonic and photonic modes. It shows a relatively high Rabi splitting of around 150 meV. The types of the modes are swapped due to the strong coupling, and at an angle of 11.4° , the spectral width of one resonance entirely vanishes. The band dia-

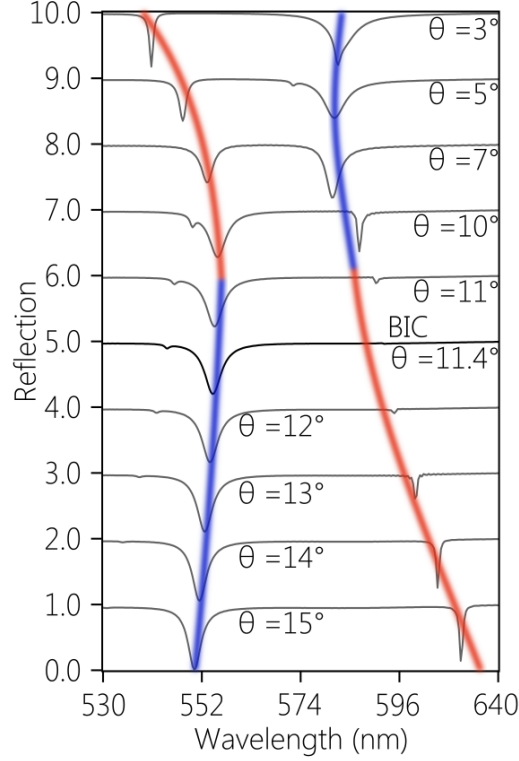


Fig. 2.3. The avoided crossing and linewidth vanishing due to the hybridization of plasmonic and photonic modes at different angles of incidences.

gram of the silver grating covered with an extended SiO_2 layer shows the dispersion of only plasmonic modes due to the absence of mode hybridization and strong coupling. Also, the nature of the plasmonic component is explored by calculating the band diagram of a high-index dielectric grating on top of a silver back-reflector. The band diagram still shows narrow resonances due to the excitation of the photonic modes in the top waveguiding layer due to the additional momentum provided by the grating. However, we observe resonance crossing and no strong coupling in the system. This suggests that the origin of surface plasmon modes involved in the coupling is not the propagating surface plasmon but the gap plasmon.

2.2.1 Quality factors of the BIC resonances

As the linewidth of the resonance disappears, its Q factor diverges, which manifests the formation of a BIC. Generally, the Q factor of a plasmonic mode is dictated by the intrinsic metallic loss and the optical radiative loss. At (near) the BIC points, the radiation into free space is inhibited (minimized); therefore, the Q factors of the hybrid plasmonic-photonic modes around BICs are only metal loss-limited. The Q factors of the resonances around the three BICs discussed earlier are calculated by fitting the reflection coefficients to the Fano formula [58] and shown in Fig. 2.3. The Q factors of the symmetry-protected plasmonic and photonic BICs are depicted in Fig. 2.3(a) and 2.3(b), respectively.

The nature of the mode is reflected in the electric fields plotted in the insets at an angle of 5° and 697.1 nm wavelength for the plasmonic mode, Fig. 2.3(a), and 2° and 540.1 nm for the photonic one in Fig. 2.3(b). The Q factor of the hybrid (Friedrich-Wintgen) BIC is shown in Fig. 2.3(c) with the type of interacting modes exchanged at the BIC point. The BIC appears at 11.4° , and the hybridization is evident from the field plots given at the insets of Fig. 2.3(c) showing a plasmonic nature (at 5° and 596.3 nm) and photonic nature (at 5° and 630.3 nm). More simulations exploring the nature of the interacting modes are given in Appendix I. At the BIC points, the radiative Q-factor diverges, which causes the total Q to be limited by the loss in the system. Therefore, the overall Q of the symmetry-protected photonic BIC will diverge to infinity due to the lack of material loss, Fig. 2.3(c). However, both symmetry-protected plasmonic BIC and Friedrich-Wintgen BIC will have finite, yet very high, Q values.

2.2.2 Band engineering in the hybridized system

Varying the thickness of the waveguiding layer changes the number of the supported waveguide modes and strongly modifies the reflectance spectra. Fig. 2.4 shows the reflection spectra vs. angle of incidence for the hybrid structure with a top dielec-

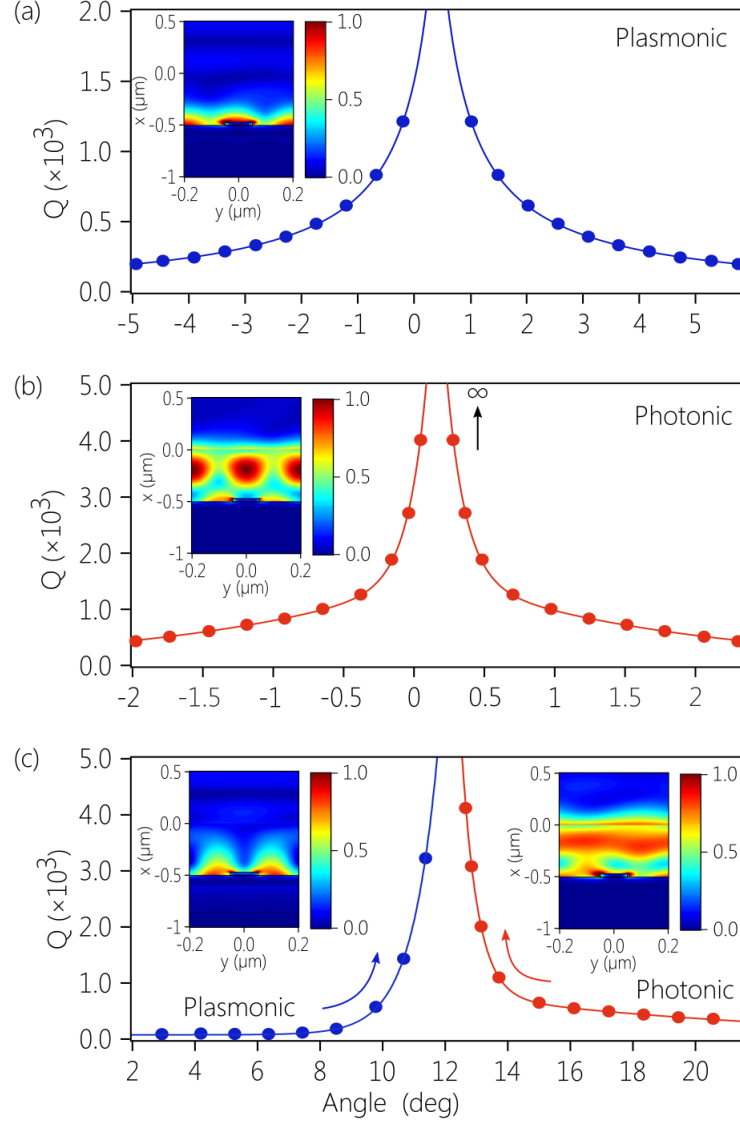


Fig. 2.4. Quality factor vs. angle of incidence for different BIC types. Q factor rapidly increasing towards the Γ -point for (a) plasmonic and (b) photonic resonances. Insets show the electric fields at (a) 697.1 nm at 5° and (b) 540.1 nm at 2°. (c) Friedrich-Wintgen BIC appears at 11.4°. Insets show fields of the plasmonic channel at 5° 596.3 nm (left) and the photonic one 15° 630.3 nm (right).

tric layer thickness of 200-nm [Fig. 2.4(a)] and 800-nm [Fig. 2.4(b)]. Several intriguing features can be noted from Fig. 2.4. First, the hybridization of the plasmonic and

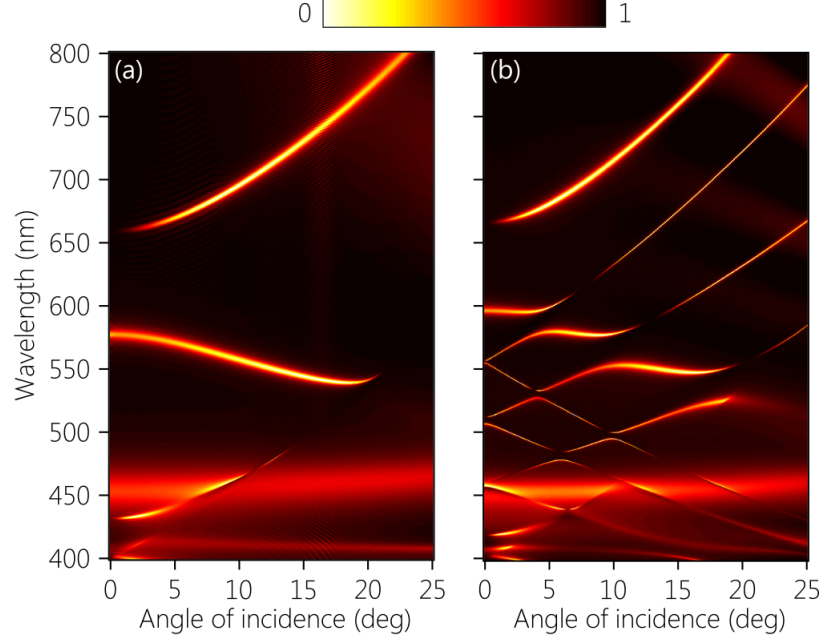


Fig. 2.5. Band diagrams of the plasmonic grating coupled to a SiO_2 waveguiding layer with thicknesses of (a) 200 nm and (b) 800 nm. Optically thicker waveguide supports more guided modes allowing more interactions of resonances.

photonic modes allows for bandgap engineering depending on the number of modes supported by the system and their spectral overlap. From the modal analysis, a 200-nm thick silica slab waveguide surrounded by air would support a single TM mode at 600 nm wavelength. That explains the single band is appearing at Fig. 2.4(a). However, the 800-nm slab supports 3 TM modes at 600 nm, which is manifested by the multiple interactions and avoided crossings depicted in Fig. 2.4(b) showing a more complicated behavior with multiple Friedrich-Wintgen BICs appearing at different θ values. These results demonstrate the possibility of bandgap engineering by designing the dispersion of either the photonic or the plasmonic component of the system. Moreover, the system supports slow light, not only at the band edge (around Γ -point) but also at multiple other θ values. More interestingly, the spectral bandwidth along which the slow light can be supported is substantially increased. We can

clearly observe three distinct bands in Fig. 2.4(b) at which the slope of the resonance is almost zero, indicating slow light. Unlike conventional plasmonic gratings where the slow light is supported at the band edge for only a single angle of incidence, here, the engineering of the band diagram with the mode hybridization allows extending this range significantly. The three slow light bands are centered at 550 nm, 577 nm, and 595 nm, with their angular bandwidths of 8° , 5° , and, 5° , respectively. Therefore, the proposed structure is capable of selecting the central angle at which the slow light exists, extending its angular span, and providing means to select where the slow light is supported spectrally.

2.3 Conclusion

In conclusion, we have demonstrated the formation of BICs in systems with a realistic intrinsic loss. Due to the strong coupling and the destructive interference of the photonic and the plasmonic modes, the losses are significantly reduced due to the suppression of radiation. Two different types of BICs are accessible in the hybrid plasmonic-photonic system due to the symmetry incompatibility with the radiation as well as the destructive reactions of resonances. A distinct characteristic of the Friedrich-Wintgen BIC achieved in this study is that it originates from the interference of two resonances with different natures. The system studied exhibits an exquisite set of phenomena including the formation of localized states with, in principle, infinite lifetimes, strong coupling with large Rabi splitting, optical bandgap engineering, and slow light with broad spectral robustness. We believe that these hybrid structures are perfect candidates for low-threshold lasers, sharp spectral filters, enhancement of nonlinear phenomena as well as sensors.

3. SINGLE AND MULTI-MODE DIRECTIONAL LASING FROM ARRAYS OF DIELECTRIC NANORESONATORS

3.1 Introduction

Bound states in the continuum (BICs) are dark states that stay localized even though they coexist with the structure’s radiation continuum [2, 8, 10, 13, 26–28, 40]. Ideal BICs have infinite lifetime and require at least one dimension of the structure to extend to infinity [2]. In practical realizations, due to perturbations and finite extent, the BIC collapses to a Fano resonance with a limited (yet still very long) lifetime – a regime known as quasi-BIC [1, 2]. Besides, in the vicinity of the BIC, near-BIC high-Q resonances can be attained by slightly detuning the system from the BIC point [3–5]. Near-BIC resonances are generally stable to fabrication imperfections as they can be obtained at a relatively broad interval of a system parameter values compared to BICs, which are typically achieved at a single point [3, 4]. Photonic structures supporting BICs have been intensively studied over the last decade as they offer unique ways for engineering and enhancing the light-matter interactions [2, 5, 6, 8, 11, 32, 33, 40]. Photonic BICs have to date enabled a plethora of applications, including light routing [59], nonlinear enhancement [60], sensing [61], and lasing [9, 44, 62]. However, the experimental realizations of BICs and their applications in the visible wavelength range have been considerably limited and started to gain interest only recently [62].

3.2 High-Q resonances in dielectric metasurfaces

The emergence of dielectric nanoresonators with strong electric and magnetic responses has enabled fundamentally new ways of engineering light-matter interactions [58, 63]. The interplay between electric and magnetic resonances in a dielectric

nanoresonator enables control over the direction of scattering, along with the spectral position, strength, and quality factor of the resonance [64]. This control can be realized in a single scatterer by tuning its shape to support a desired electromagnetic response [65]. Additionally, arranging the nanoresonators in a lattice can influence their spectral response providing more degrees of control over light-matter interaction [66, 67]. Coupling between the electric dipole (ED) and magnetic dipole (MD) in individual dielectric resonators can be controlled by placing the resonators in close proximity to engage their near field interaction. However, due to the high refractive index of dielectric nanoresonators' materials, the electromagnetic field is generally tightly confined inside the resonator and near field coupling is relatively low. Collective diffractive coupling of EDs and MDs has been proposed as a more effective way of controlling the response of dielectric nanoresonators arrays [67]. This can be achieved through the coupling of ED and MD resonances in an array of dielectric scatterers to the Rayleigh anomaly of the array.

In this work, we investigate the experimental realization of high-Q factor coupled ED and MD resonances supported in the visible range by the array of dielectric nanoresonators due to their collective interaction. Furthermore, we demonstrate lasing action within the visible spectrum, relying on the high-Q resonances supported by arrays of nanoresonators. The laser operates at room temperature with high beam directionality and low-threshold. In addition, we experimentally investigate the BIC-assisted mode engineering in arrays of dielectric nanoresonators, and we show multi-wavelength directional lasing. Two- and three-mode lasers have been demonstrated experimentally, showing the potential for this type of structure to support controllable multi-wavelength on-chip microlasers.

Two orthogonal orientations of dipole modes are generally supported in a dielectric resonator; a horizontal (electric dipole, ED) and vertical (magnetic dipole, MD) (Fig. 3.1(a)). Here, we study an array comprising TiO_2 cylindrical nanoresonators with a height of 300 nm arranged in a square lattice with a period of 400 nm on a silica glass substrate, Fig. 3.1(b). The structure is covered with a polymer, index-matched to

the substrate. Our choice of materials and dimensions are to achieve resonances in the visible wavelength range.

Figure 3.1(c) shows the reflectance spectra of the array as a function of the radius of the nanoresonators. Three resonances corresponding to the ED, MD as well as a magnetic quadrupole (MQ) can be observed in the reflectance spectra, as indicated in Fig. 3.1(c). The resonance classification is accomplished based on the displacement current loops and E-field profiles; more information can be found in Section 1 Appendix II. The Rayleigh anomaly (RA) of the array is depicted as a dashed white line in Fig. 3.1(c). As the radius of the nanoresonators decreases, the linewidth of the MD resonance gets narrower and the position of the MD approaches that of the Rayleigh anomaly. Both observations are distinctive features of the diffractive coupling [67]. We also notice that the spectral position of the MQ follows the Rayleigh anomaly closely. The ED and MD modes spectrally overlap a radius of 82 nm, and a wavelength of 610 nm, highlighted by the dashed circle in Fig. 3.1(c) confirming the realization of Kerker's condition. Almost zero light reflection is realized at the Kerker point with a near-unity unidirectional transmission. Another feature that results from the diffractive coupling of the dipoles to the Rayleigh anomaly is the enhancement of electromagnetic fields (Fig. B2) which is very advantageous in boosting the non-linear phenomenon. More insight can also be gained from studying the effect of the nanoresonator height on the spectral positions and widths of the ED, MD, and MQ in Section 2 of the Appendix II.

A scanning electron microscope (SEM) image of the fabricated structure is given in Fig. 3.1(d). For details of the fabrication, see Methods and Fig. B5. Transmittance at normal incidence from a few samples with different R_{cyl} was characterized using spectroscopic ellipsometry, Fig. 3.1(e). A single resonance is observed at a radius value of 85 nm where the ED and MD start to overlap, as can be noticed from Fig. 3.1(e). At larger radii values, 90 nm and 95 nm, two dips corresponding to the ED and MD are observed. The measured transmittance is in a very good agreement with the simulated spectra, Fig. B4. However, due to the non-uniformity in the radii of the

fabricated sample, the measured resonances are broadened, and their dip positions are slightly shifted compared to the simulated ones with around 5 nm.

3.3 Lasing in dielectric metasurfaces

After the successful demonstration of the passive nanoresonator arrays with high-Q factor resonances, we employ them to provide feedback for lasing action in the visible spectrum. First, the index matching coating is washed off. Then, the array is spin-coated with polyvinyl alcohol (PVA) solution of an organic gain medium (Rhodamine 101) with a concentration of 10 mM, which acts as an active material. The spin coating yields an active layer with a thickness of $\sim 2 \mu\text{m}$. To characterize the lasing action, the sample is pumped with the second-harmonic output from an Nd:YAG laser (532 nm, 1-Hz repetition rate, and 400-ps pulse duration). The emitted light is collected through fiber and directed to a spectrometer to get the emission spectrum to demonstrate the two critical effects of lasing; threshold and spectral narrowing. The setup schematic is given in Fig. B7 and details of the experiment can be found in Methods.

Figure 3.2(a) depicts the evolution of the collected emission spectra as the pump fluence increases showing a narrow lasing peak emerging around 614 nm. An apparent threshold behavior is observed where the emission transitions from enhanced spontaneous to stimulated emission at around $40 \mu\text{J}/\text{cm}^2$, as evident from the experimental (Fig. 3.2(b)) and simulated (Fig. 3.2(c)) data. This process is accompanied by a significant narrowing of the emission spectral width from $> 30 \text{ nm}$ to $< 1 \text{ nm}$, as observed in the experiment (Fig. 3.2(d)), and numerical simulations (Fig. 3.2(e)). The emission directionality is characterized using back focal plane measurements, see Methods. Below the lasing threshold, the enhanced spontaneous emission is illustrated with a back focal plane cross-section and the emission pattern of Fig. 3.3(a) with the cross-section showing a relatively wide spatial spread. However, above the threshold, the same measurements (see, Fig. 3.3(c)) indicate tightly focused spots

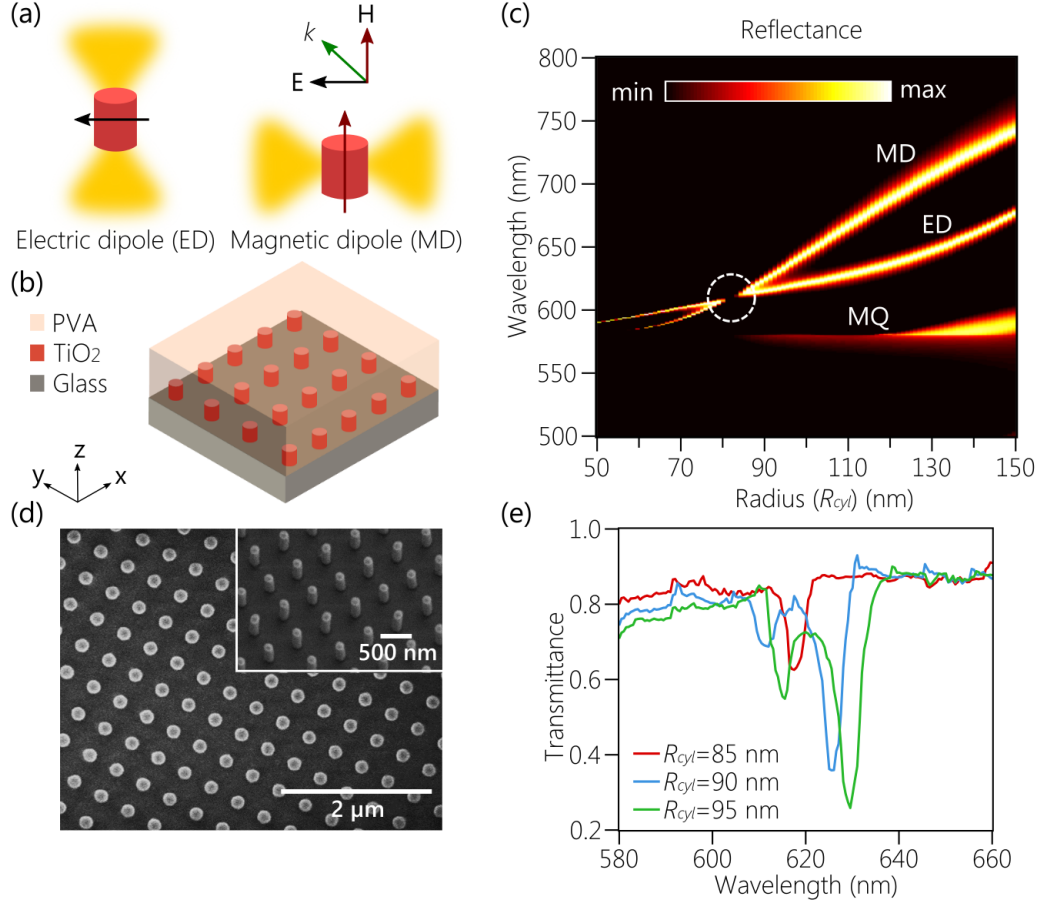


Fig. 3.1. High-Q resonances in arrays of dielectric nanoresonators with electric and magnetic dipoles. a) Electric and magnetic dipole resonances supported by a dielectric nanoresonator. b) A schematic of the array structure with a square lattice of 400 nm period made of titanium oxide (TiO₂) cylindrical nanoresonators with a height of 300 nm on a glass substrate and covered with polyvinyl alcohol (PVA). c) Simulated reflectance as a function of the nanoresonator radius (R_{cyl}). The dashed white circle shows the disappearance of the resonance, indicating the realization of the Kerker condition at $R_{cyl} = 82$ nm and $\lambda = 610$ nm. The three resonances correspond to the magnetic dipole (MD), electric dipole (ED) and the magnetic quadrupole (MD), respectively and the dashed white line shows the Rayleigh anomaly (RA) of the array. d) An SEM image of the fabricated structure. e) The measured transmittance of the array with radii of 85, 90, and 95 nm.

and narrow beams at 3.5° with a less than 0.8° in beamwidth. It is worth mentioning that due to our structure's square lattice, the back focal plane image should consist of two points along the x-axis and two along the y-axis. However, Fig. 3.2(c) shows only a pair of bright spots along the x-axis, which is a result of the polarization of the pump. When an analyzer with orthogonal orientation (along the y-axis) is introduced in the lasing emission path before collection, we observe four bright spots in the back focal plane emission as expected, Fig. B8. All our experimental studies are guided and supported by the advanced multiphysics numerical framework built on coupling carrier kinetics with a full-wave time-domain Maxwell equation solver [23]. Details of the numerical simulations can be found in Methods and Section 2 of Appendix II.

To the best of our knowledge, this is the first report of lasing action in the visible spectrum with feedback from an all-dielectric high-Q factor nanoresonator array. Unique features of the proposed system include a low threshold, tunable-by-design high-Q factor resonances, and room temperature operation with no need for complex cryogenic infrastructure. All these advantages suggest the suitability of the proposed laser for integration into a multitude of applications such as sensors, biological probes, and on-chip light sources.

3.4 Modal engineering near BIC states

By engineering the geometrical and material parameters of a unit-cell dielectric resonator, we can selectively excite distinct resonant modes and also tune their spectral properties [68,69]. Therefore, an optimal unit-cell design can enable an excellent control over the band-diagram of the entire structure array. In general, band-diagram engineering can be accomplished through geometrical optimization which when applied to metasurfaces, results in complex shapes with astringent unit cell geometries and dimensions leading to further fabrication constraints [68–70]. To perform mode engineering in our study, we intentionally limit the structure design to a simple, easy-to-fabricate square array of TiO_2 cylinders. A unit-cell of this type appears to be

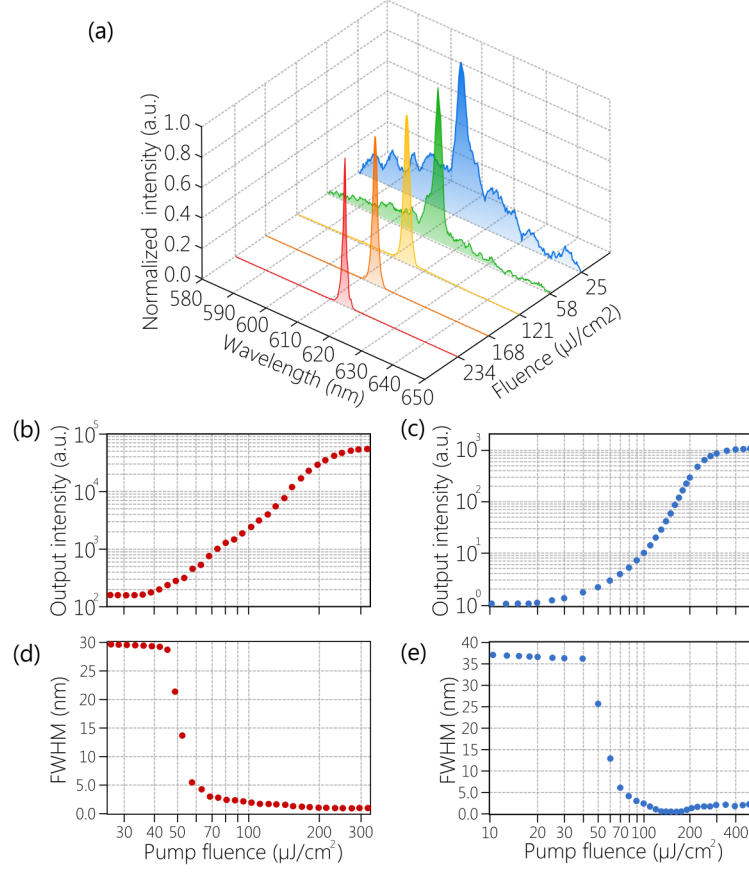


Fig. 3.2. Lasing action with near-BIC feedback. (a) The evolution of the emission spectra collected from the gain-coated structure with the increased pump fluence, showing a transition from amplified spontaneous emission to lasing. The experimental (b) and simulated (c) output intensities vs. the pump fluence. The experimental (d) full width at half-maximum (FWHM) and simulated (e) FWHM as a function of pump fluence.

an ideal prototype for analyzing the interplay between the electric and magnetic responses in a dielectric nanoresonator, studying the array effect, as well as exploiting the intriguing physics of BICs.

Figure 3.4(a) shows the simulated reflectance of an array comprising nanoresonators with $R_{cyl} = 80$ nm as a function of the angle of incidence and wavelength. The resonance at the Γ point around 610 nm corresponds to the point where the ED

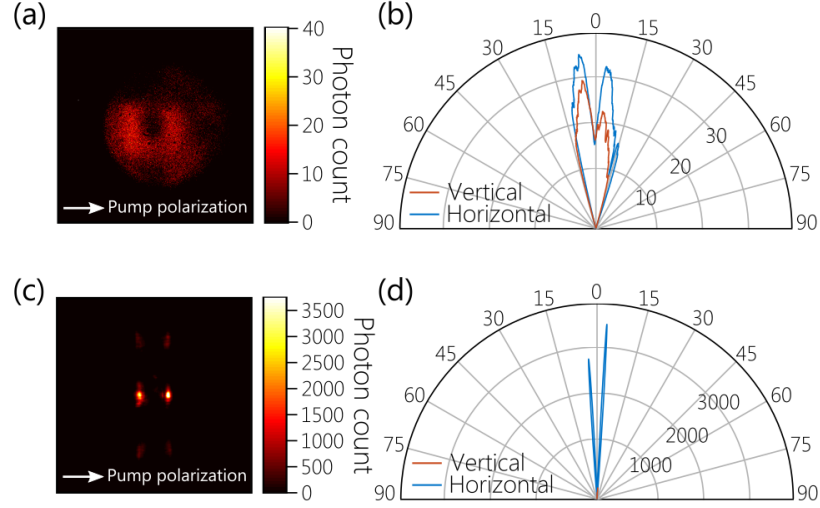


Fig. 3.3. Directionality of the lasing emission. Back focal plane images and the radiation patterns, which are vertical and horizontal cross-sections of the focal plane image, of the laser emission below (a,b) and above (c,d) lasing threshold. White arrows in (a) and (c) show the polarization of the pump laser.

and the MD start to overlap, which we used as a feedback for the single-mode lasing demonstrated in Fig. 3.2. It is worth noting that the array supports two types of BIC states, one at the Γ point with wavelength 669.2 nm, which is a symmetry-protected state. Additionally, an off- Γ Friedrich-Wintgen (FW) BIC is also supported at 8° at a wavelength of 741 nm [2,13]. The FW BIC is highlighted with a dotted white circle in Fig. 3.4(a) and magnified in the inset. This emphasizes the ability of an array with such a simple unit cell structure to support multiple types of resonances with different underlying physics. Not only can this structure support simple "band-edge" mode at the Γ point, but it also provides access to the non-trivial FW BIC states that are not symmetry-protected and hence are more resilient to structural imperfections.

The structure with $R_{cyl} = 100$ nm shows a different reflectance response with two resonances observed at the Γ point corresponding to the electric dipole at and the magnetic dipole resonances at 622 nm and 646.5 nm, respectively. As can be seen in

Fig. 3.4(b) the array with $R_{cyl} = 100$ nm supports a symmetry-protected BIC at 683 nm, inside the dashed yellow circle as well as an FW BIC at 824 nm and 11.5° inside the dotted white circle. The stark difference between the optical response of the two designs confirms an excellent opportunity to engineer the band-edge and bandgap of metasurfaces by tuning their geometrical parameters.

We use this concept to achieve two- and three-mode lasing from arrays of dielectric nanoresonators. On-chip multi-mode lasers are invaluable tools for many applications such as optical signal processing, quantum computing, wavelength multiplexing for telecommunication, and others. In this section, we explore the engineering of the various resonance in play in our structure to realize multi-mode lasing. We design, fabricate and experimentally demonstrate dual- and triple-mode laser solely based on the optimal choice of the radius of the dielectric resonators in the BIC-type metasurface array.

Figure 3.5 shows the lasing dynamics from an array with nanoresonators with $R_{cyl} = 95$ nm and a ~ 2 μm active cover layer of Rhodamine 101 in PVA. With increased pump intensity, one laser peak emerges at a threshold of ~ 60 $\mu\text{J}/\text{cm}^2$ around 610 nm. At a pump fluence of 140 $\mu\text{J}/\text{cm}^2$, another peak appears at 617.5 nm, as seen in Fig. 3.5(a). The evolution of the intensity of both laser peaks vs. the pump fluence can be seen in Fig. 3.5(b). A rotating analyzer is used before feeding the collected emission to the spectrometer to study the polarization properties of the laser emission. Back-focal plane images of the laser emission at different analyzer angles are depicted in Fig. 3.5(c). At 0° analyzer angle, Fig. 3.5(c) (left) shows that laser emission takes the shape of two spatial beams. However, an analyzer angle of 90° , Fig. 3.5(c) (right) shows the appearance of two additional beams. The change of the measured peak values of both lasing wavelengths, 610 nm and 617 nm, is plotted in Fig. 3.5(d). We can note that the laser peak at 617.5 nm shows little sensitivity to the analyzer rotation, dropping to only half of its maximum value at the analyzer angle of 90° . However, the peak at 610 nm is much more sensitive to the analyzer orientation. At an analyzer angle of 90° , the peak intensity of the 610 nm beam drops to $\sim 10\%$ of its

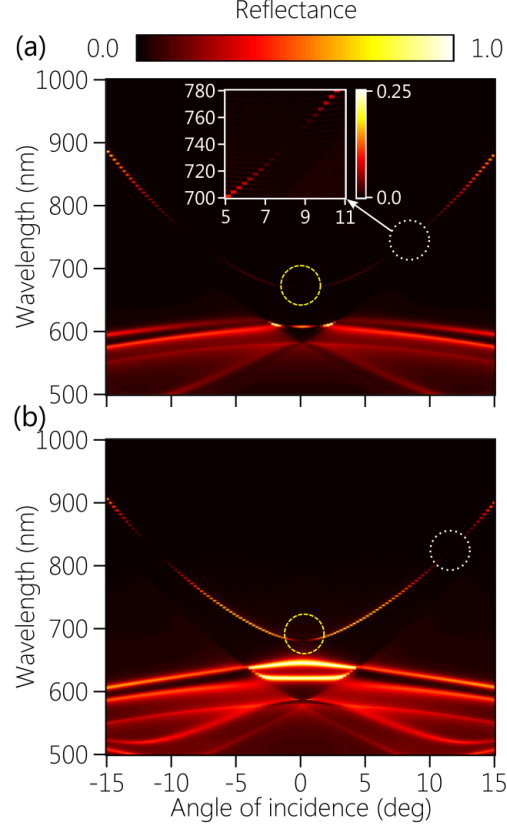


Fig. 3.4. The simulated reflectance vs. the angle of incidence and wavelength. a) The reflectance of an array with TiO_2 cylinder nanoresonators ($R_{cyl} = 80$ nm). The dashed yellow circle at the Γ point highlights the symmetry-protected BIC at 669 nm. The dotted white circle highlights the off- Γ (Friedrich-Wintgen, FW) BIC, which is zoomed in in the inset at 741 nm. b) An array with $R_{cyl} = 100$ nm exhibiting the symmetry-protected BIC at the Γ point and 683 nm (dashed yellow circle) and an FW BIC at 824 nm and 11.5° (dotted white circle).

maximum value (at 0° angle). From Fig. 3.5(d), we can see that when the analyzer angle is set to 90° , the peak amplitude of the two laser wavelengths is almost equal. From this, we conclude that each wavelength emits in a different spatial direction. The beam at 610 nm emits at 4.6° with a beamwidth of 2° , and the laser peak at 617.5 nm has a spatial beam around 7.9° with a 1.6° beamwidth as calculated from

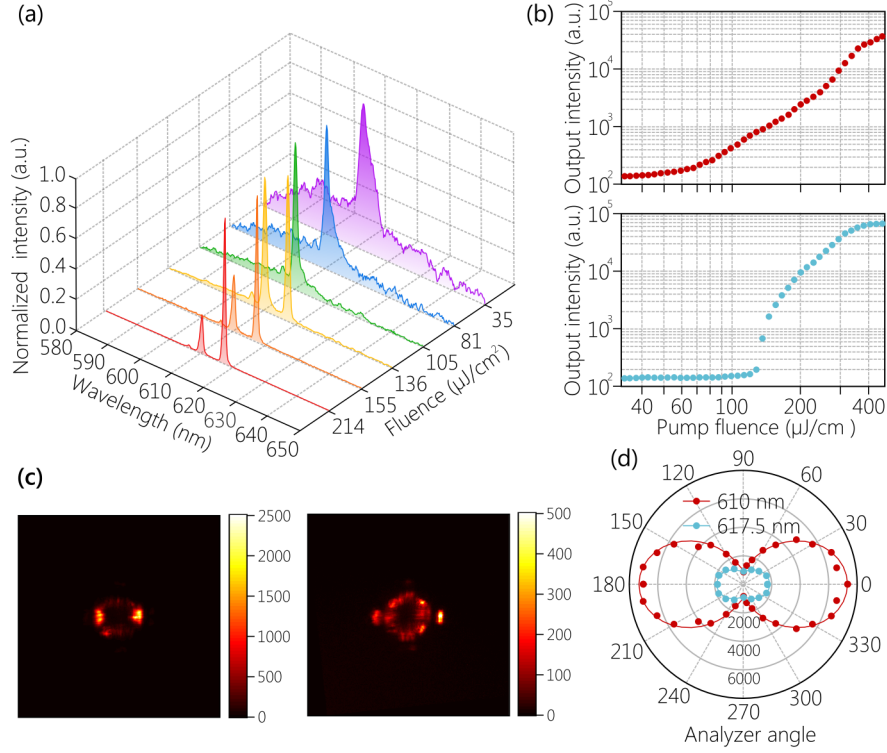


Fig. 3.5. Dual-mode lasing action from dielectric arrays. a) The evolution of the lasing spectrum with pump fluence. b) The output intensity of the lasing peak at 610 nm (top) and 617.5 nm (bottom) as a function of pump fluence. c) Back-focal plane image of the laser emission above the threshold at an analyzer angle of 0 (left) and 90 (right). d) The intensity of the dual laser emission as a function of the polarizing analyzer angle.

the back-focal plane image in Fig. 3.5(c) (right). Triple-mode lasing has also been observed and reported in Fig. B9.

It is worth mentioning that our choice for the unit cell for the multi-mode operation is a proof-of-concept and is simply based on the number of supported resonances. Further optimized unit cells can be investigated to provide equal peak amplitude, controllable threshold, and spectral separation. Achieving multi-mode on-chip lasing will open up a multitude of opportunities in optical computing, sensing, and telecommunications. Our design and methodology represent a step on the way to realize low threshold room-temperature nanolasers with multiple wavelengths and high direction-

ality. Future directions will include optimization mechanisms that take full advantage of the interplay between the electric and magnetic responses in dielectric resonators alongside the rich physics of BICs to gain control on the characteristics of each lasing peak as well as their spectral separation.

3.5 Discussion

In summary, we design, fabricate, and experimentally demonstrate high-Q factor resonances in arrays of dielectric nanoresonators in the visible wavelength range. We utilize the proposed all-dielectric arrays to experimentally demonstrate highly-directional, low-threshold lasing action in an organic dye coating layer. To the best of our knowledge, this is the first demonstration of room temperature lasing in the visible spectrum with an all-dielectric array of nanoresonators. Our experimental studies are guided and supported by the advanced multiphysics numerical framework built on coupling carrier kinetics with a full-wave time-domain Maxwell equation solver. Using the developed framework to engineer the electric and magnetic dipole modes in dielectric resonators, we utilize the feedback from the high-Q factor structures to experimentally realize and explore multi-mode lasing. Our results open exciting paths for combining different physical mechanisms in a single dielectric array without intricate resonator designs. We believe that our study could enable advanced, controllable engineering of light-matter interactions with prospective applications to the topological states engineering and quantum light generation.

3.6 Methods

3.6.1 Metasurface Fabrication

The fabrication process starts with creating the required pattern on a silica substrate using a positive-tone resist (ZEP 520A) using electron beam lithography. The silica glass substrates (commercially available optical quality glass from PG&O) are

cleaned in solvent (toluene, acetone, IPA) followed by a dehydration bake at 160°C for 2-5 minutes. At this stage, ZEP 520A electron-beam resist (commercially available from ZEON Chemicals) is spin-coated onto the dry substrate and cured at 180°C for 3 minutes. The thickness of the resist should match the desired nanocylinder height. The spin process conditions are varied according to the spin-sheet to arrive at the desired thickness denoted as h . Before exposing the resist to electron-beam, a very thin ($\sim 5\text{ nm}$) layer of Cr metal is deposited onto the resist coated substrate using the e-beam deposition technique to avoid charging related writing discrepancies on a dielectric substrate (Fig. B6(a)). Following the deposition, the sample is immediately loaded onto the load lock of the electron beam lithography (EBL) instrument to prevent further oxidation of the Cr thin film. After electron beam exposure, the first Cr layer is etched away using Cr-16 chromium etchant solution and followed by a DI rinse. Next, the resist was developed in ZDMAC developer for 90 seconds and rinsed in IPA. Some undeveloped residual resist may remain at the bottom of the narrow cylinder holes which are then cleaned off by ashing the resist in a barrel etcher in O_2 plasma (at 100W, 1.2T) for 1 minute. This may lead to some reduction of the resist thickness from top-down etching as well as an increase in the diameter of the cylinders. Initial resist thickness and written diameter of the cylinders can be adjusted to account for this step. At this point, the sample should have an array of cylindrical holes in the resist (Fig. B6(b)).

Next, the sample is loaded onto an atomic layer deposition (ALD) tool for the growth of the TiO_2 . ALD allows for uniform and highly conformal layer by layer growth and therefore ensures complete coverage of all the holes (Fig. B6(c)). The TiO_2 thickness is decided by the maximum diameter of the cylinders (d) on the sample. Due to conformal growth from all sides thickness of $d/2$ would be enough to fill the cylinders (Fig. B6(d)). However, we keep a margin of growing an additional 10-15 nm . In order to ensure the stability of the polymer-based resist, the ALD operating temperature is kept much below the resist curing temperature, in this case, at a 120°C . A low growth rate of 0.6 nm/cycle is achieved in this low-temperature

process. In addition, other process parameters such as precursor and water pulse times, purge times, pressure, etc. are also optimized to arrive at a reasonably good optical quality of the grown TiO_2 film. At this stage, TiO_2 covers not only the cylinder holes but also the top surface of the resist. To planarize the top surface and also to expose the resist layer from the top, at this step, the excess TiO_2 cover is etched away using a plasma RIE technique. A combination of BCl_3 , Cl_2 , and Ar gas chemistry is used at 650W RF power, 80W bias power, and 0.8T pressure (Fig. B6(e)).

The remaining resist matrix can then be removed in NMP (N-Methyl Pyrrolidine) heated at 120°C followed by rinsing the sample in acetone and IPA. This concludes the fabrication of the high aspect ratio (Fig. B6(f)).

3.6.2 Characterization

The fabricated metasurfaces are characterized by measuring the transmittance spectra at normal incidence for both *p-* and *s-* polarizations. This takes place after the TiO_2 etching but before the removal of resist. The resist polymer has a refractive index of around 1.45 and therefore satisfies the index matching condition with the substrate. Optical characterization is performed using the J.A. Woollam V-VASE UV-VIS-NIR variable angle spectroscopic ellipsometer. The measured transmittance spectra at different R_{cyl} of the resonators are given in Fig. B4(a) with solid lines showing the p-polarization and dashed lines corresponding to the s-polarization of the incident light. We can clearly observe that under normal illumination, the metasurfaces responses are polarization-independent. Additionally, the simulated transmittance as a function of R_{cyl} and wavelength is shown in Fig. B4(b). Dashed lines indicate the radii corresponding to the measurements in Fig. B4(a) with red, blue and green indicating $R_{cyl} = 85 \text{ nm}$, $R_{cyl} = 90 \text{ nm}$ and $R_{cyl} = 95 \text{ nm}$, respectively. As evident from Fig. B4, the measured transmittance of different samples is generally in good agreement with the predictions from the simulations. Deviations between experimental and simulated data are believed to be due to the fabrication imperfections as we observed

non-uniformity in the radii values of the nanoresonators of the same sample. This led to spectral broadening, causing a reduction in the Q-factors as well as a shift in the location of the resonances.

3.6.3 Lasing measurements

To study lasing properties with the metasurface feedback, we use a frequency-doubled Nd: YAG picosecond laser. The laser generates pulses with a carrier wavelength of 532 nm, a pulse width of 400 ps, and a repetition rate of 1 Hz. A schematic of the setup is shown in Fig. B7. The laser beam that pumps the metasurface is focused down to 100 μ m with a 5 \times objective. The light emission from the sample is collected with a fiber, which is then fed to a spectrometer equipped with a charge-coupled device (CCD). A notch filter centered around 532 nm is used to block the pump. All lasing measurements are done in air at room temperature. Another CCD is used to image the sample plane for sample selection and alignment and also to ensure an accurate estimation of the pump spot size. Back focal plane measurements have been carried out with the same setup as lasing by redirecting the laser emission from the spectrometer to a CCD through a lens that is adjusted to form a back focal plane image at the camera sensor.

3.6.4 FDTD simulations of lasing dynamics

We utilize an in-home built framework of a multi-level system [23–25] incorporated in a commercial software finite difference time domain (FDTD) solver [71] to model nonlinear light-matter interactions [72, 73]. The multi-level framework allows for capturing the behavior of the gain materials embedded in photonic nanostructures and have an accurate estimate of their threshold and spectral response. In this work, the gain medium (Rhodamine 101) is modeled using a four-level system, and the electromagnetic waves are treated classically with Maxwell’s equations [23]. The

four-level atomic system used is depicted in Fig. B5. More details can be found in Section 3 of Appendix II.

3.7 Conclusion

To summarize, we design, fabricate, and experimentally demonstrate the high-Q, BIC-operating metasurfaces for the visible wavelength range for the first time. We utilize the proposed all-dielectric metasurfaces to experimentally demonstrate highly-directional, low-threshold lasing action in an organic dye coating layer. To the best of our knowledge, this is the first demonstration of room temperature lasing in the visible spectrum with an all-dielectric metasurface. Our experimental studies are guided and supported by the advanced multiphysics numerical framework built on coupling carrier kinetics with a full-wave time-domain Maxwell equation solver. Using the developed framework to engineer the electric and magnetic dipolar modes in dielectric resonators to achieve BICs, we utilize the feedback from the high-Q metasurfaces to explore multi-mode lasing. Our results open exciting paths for the fascinating physics of BICs into the area of lasing devices operating in the visible wavelength range. The proposed near-BIC lasers could enable advanced, controllable engineering of light-matter interactions with prospective applications to the topological states engineering and quantum light generation.

4. EXPLORING TIME-RESOLVED MULTIPHYSICS OF ACTIVE PLASMONIC SYSTEMS WITH EXPERIMENT BASED GAIN MODELS

The emerging field of plasmonics has stimulated the development of composite optical materials and transformative nanophotonic devices with the potential for significant societal and technological impact [74]. The fundamental requirement in all these applications is to route and manipulate photons actively at the nanoscale [75]. Therefore, there is a high demand for coherent nanoscale optical sources in high-speed and deeply-integrated photonic circuits [76,77]. While all-dielectric optical sources are restricted by the diffraction limit, surface plasmons (SPs), the oscillations of free electrons in plasmonic materials (e.g., the noble metals), allow overcoming the diffraction limit with the subwavelength confinement of light. On the other hand, losses introduced by electron scattering in metals can greatly degrade the performance of a plasmonic system. As a result, active plasmonic devices can be designed by combining a plasmonic material (i.e., metal) and a gain medium (i.e., organic dyes, quantum wells, quantum dots, etc.) to either just compensate for metal losses [78, 79], or to create a nanoscale coherent light generation with SP amplification by stimulated emission of radiation (spaser) [80–82]. Overcoming the diffraction limit with plasmonic nanostructures in spasers is used in several ways. First, replacing a reflective resonator built on a photonic mode (of the wavelength scale) inside a dielectric cavity by a resonator based on a plasmonic mode (of the subwavelength scale) confined at the surface of the metal nanoparticle substantially reduces the spaser dimensions. Also, the feedback loop in the spaser provided by the near-field interaction between

This chapter is based on S. I. Azzam, J. Fang, J. Liu, Z. Wang, N. Arnold, T. A. Klar, L. J. Prokopeva, X. Meng, V. M. Shalaev, and A. V. Kildishev, “Exploring time-resolved multi-physics of active plasmonic systems with experiment-based gain models,” *Laser & Photonics Reviews*, vol. 13, no. 1, p. 1800071, 2019, and is reproduced with publisher’s permissions.

the metal and gain parts of the structure along with the high scattering cross-section offered by the plasmonic structures are utilized to form plasmonic random lasers or random spasers [83]. So far, numerous active studies of the spaser have been reported. The first nanoscale coherent generation of SPs was reported in ensemble measurements for Au nanospheres with dielectric gain shells randomly suspended in water [82]. In addition, a great number of diverse spaser configurations has been explored, such as nano-wires [84, 85], coaxial pillars [86], nano-cavity arrays [87–89], metamaterials [90], as well as novel lasing mechanisms and feedback such as lasing using stopped light [91], lasing via plasmonic leaky modes [92], etc. All of them have revealed line-width narrowing and nonlinear output behavior under optical pumping. Perhaps, the very initial use of periodic nano-cavity arrays dates back to 2000 when Vučković et al. [93, 94] used a silver nanoholes array to enhance LED efficiency. Just a few years later, Stuart [95] got a patent to use a similar structure for lasing. Vučković-Stuart’s design was successfully implemented for a lasing device by van Beijnum et al. [81] with InGaAs as a gain material, though no gain was used inside the nanoholes due to fabrication constraints. Simultaneously, an organic injection lasing utilizing gold nano-disc arrays was demonstrated in [96].

Along with lasing, gain media are also used to compensate losses in nanoplasmonic devices [78, 79, 97]. If gain is introduced to the system, one can observe amplified SPs coupled with photons. This would allow efficient plasmonic interconnects and low-loss metamaterial structures. The amplification of SPs and full compensation of optical losses have been proposed in various plasmonic devices such as long-range SPP waveguide [98], active split-ring resonators [99, 100] and active negative-index metamaterials [79, 101] studied in time and frequency domains.

In order to unlock the temporal details of the spaser and SP amplifier, numerous theoretical and numerical methods have been proposed [102–104]. Among them, due to the accurate treatment of quantum properties of the gain medium, the time domain multiphysics approach is viewed as the most powerful method, in which a finite-difference, finite-volume, or a finite element time-domain method is coupled

to a multi-level system through auxiliary differential equations [105]. Using a classical finite-difference time-domain (FDTD) scheme, this approach has been applied to investigate lasing dynamics [106, 107], and interpret lasing experiments [87, 103]. Recently, the Maxwell-Bloch-Langevin (MBL) approach has been introduced and broadly used by the Hess group [108–110] to account for the spatial and temporal fluctuations providing a more accurate means of simulating amplified spontaneous emission. For example, the use of the MBL approach provided insight on the lasing dynamics in an active nanofishnet structure [109], indicating that the bright mode is subject to a nonlinear competition with the dark plasmonic mode, leading to a steady-state emission where bright and dark modes coexist and could be used to control the system. Adding the concept of the stopped-light to plasmonic nanolasers [91] and employing the MBL approach allow to perform a detailed study of the spatio-temporal dynamics of coherent amplification and lasing [110].

Although most of the simulations provide self-consistent results, few works simulate lasing dynamics using kinetic parameters directly retrieved from analysis of the gain media [111]. In addition, all these schemes rely on a four-level atomic system that may not be accurate enough in some more complex gain media that exhibit non-negligible split transitions, e.g., organic dyes [112]. In this work, we provide a detailed study on lasing and net amplification for plasmonic devices with gain. First, we use a model developed here to investigate and confirm our recent experimental work on lasing from silver nanoholes arrays coated with Rhodamine-101 (R101) dye [89]. Then, we investigate the compensation of surface plasmon polariton (SPP) losses in a Kretschmann-Raether configuration with adjacent Firefly*Fluorescent Green dye [112]. However, the approaches used here can be applied to general cases of modeling active plasmonics with multi-level gain systems.

To address the need for modeling the gain media in time domain accurately, we study solid films of the organic dyes (R101 and Fluorescent Green dye) using a pump-probe setup and match the measurements with the numerical models to retrieve the kinetic parameters of the dyes. The pump-probe results indicate the dependence of

population inversion and effective gain on the pumping power. The retrieved kinetic parameters are then fed into a full-wave FDTD model to study the dynamic process in the plasmonic and gain medium coupled systems [89, 97]. For both experiments and numerical models, we observed net amplification and fast gain saturation, which is directly linked to the plasmonic field enhancement. For the silver nanoholes array, as more gain is introduced to the coupled system, the simulated emission shows a clear lasing threshold behavior matched with the experiment. We observe the clamping of the population inversion and consequently gain depletion, which manifests as coherent emission of SPs. Furthermore, for the Kretschmann-Raether configuration, no lasing can be observed due to the absence of feedback. Therefore, as the gain in the system is increased, clamping of the population inversion and consequent gain depletion occurs, but in this case, it corresponds to the amplification of the SPPs, and hence loss compensation is attained. We believe our time-domain simulations with calibrated kinetic parameters are particularly instrumental for acquiring insight in the time dynamic physics of plasmonic structures/nanostructures with gain [23]. The remainder of this chapter is organized as follows: after presenting the kinetic models of four and six-level systems in Section 2, we also provide a brief comparison of their similarities and differences. We then proceed with the review of primary results and their analysis in Section 3 as we apply the proposed model to two different systems where net gain and lasing are studied.

4.1 Theoretical models

The interaction between the electromagnetic field and the gain medium is modeled using a semi-classical approach in which the atoms/molecules of the gain medium are treated quantum mechanically using a four-level or a six-level quantum system based on the type of the dye (shown in Fig. 4.1), and the electromagnetic waves are treated classically with Maxwell's equations.

4.1.1 Four-level system

Four-level quantum system is shown in Fig. 4.1(a). Total population density of the non-excited atoms or molecules of the gain medium N are generally initially hosted in the ground level $|0\rangle$. They can then be pumped with the Gaussian pump pulse to the highest level $|3\rangle$. A fast non-radiative transition occurs between the highest level $|3\rangle$ and upper lasing level $|2\rangle$. Molecules can be transferred from the upper to the lower lasing levels (from $|2\rangle$ to $|1\rangle$) via spontaneous and stimulated emissions. A proper coupling between the gain medium and substantial local field enhancement might result in a population inversion between energy levels $|2\rangle$ and $|1\rangle$, where the stimulated lasing action is intended to take place.

We assume that initially the system is at the ground level $|0\rangle$. Population density at a given energy level E_i varies with time and position $N_i(r, t)$, where $i \in \{1, 2, 3, 4\}$. The total population is universally conserved: $N_0(\vec{r}, t) + N_1(\vec{r}, t) + N_2(\vec{r}, t) + N_3(\vec{r}, t) = N$. The system's relaxation from higher to lower levels follows an exponential decay, where upward transitions can be neglected in the visible energy range (due to detailed balance and Boltzmann distribution). Then the dynamics of the population densities at different energy levels shown in Fig. 4.1(a) satisfies Eqs. (4.1),

$$\begin{aligned}\dot{N}_3 &= -\tau_{32}^{-1}N_3 + f_{30}, \\ \dot{N}_2 &= -\tau_{21}^{-1}N_2 + \tau_{32}^{-1}N_3 + f_{21}, \\ \dot{N}_1 &= -\tau_{10}^{-1}N_1 + \tau_{21}^{-1}N_2 - f_{21}, \\ \dot{N}_0 &= \tau_{10}^{-1}N_1 - f_{30}.\end{aligned}\tag{4.1}$$

Time evolution of the population densities at different levels N_i is governed by the relaxations (with "−") from an upper level to a lower level, the inflow rate (with "+") to a lower level population due to relaxation from an upper level, and the transition rate due to stimulated energy transfer between electromagnetic fields and the gain medium. Only the dominant relaxation channels with a decay time τ_{ij} for each ij level pair are included. They have both radiative and non-radiative contributions defined as $\tau_{ij}^{-1} = \tau_{r,ij}^{-1} + \tau_{nr,ij}^{-1}$. In the current model we assume that the relaxation

from $|3\rangle$ to $|0\rangle$ can be neglected in comparison with the much faster channel $|3\rangle$ to $|2\rangle$.

The driving terms f_{ij} modeling the stimulated energy transfer are given by Eq. (4.2) [105],

$$f_{ij} = \frac{1}{\hbar\omega_{ij}}\mathbf{E}\dot{\mathbf{P}}_{ij}, \quad ij \in \{21, 30\}, \quad (4.2)$$

where ω_{ij} , \mathbf{P}_{ij} are the Lorentzian frequency and the macroscopic polarization of the transition from $|i\rangle$ to $|j\rangle$, respectively. Each macroscopic polarization $\mathbf{P}_{ij}(r, t)$ satisfies the Lorentz ordinary differential equation given by Eq. (4.3)

$$\ddot{\mathbf{P}}_{ij} + \gamma_{ij}\dot{\mathbf{P}}_{ij} + \omega_{ij}^2\mathbf{P}_{ij} = \kappa_{ij}[N_j - N_i]\mathbf{E}, \quad ij \in \{21, 30\}, \quad (4.3)$$

where the excitation term is proportional to the difference in populations $N_j - N_i$, γ_{ij} is the dephasing rate for the polarization \mathbf{P}_{ij} . Here the coupling coefficients are $\kappa_{ij} = 6\pi\epsilon_0 c^3 / (\tau_{r,ij}\omega_{ij}^2\sqrt{\epsilon_h})$, where $\tau_{r,ij}$ is the radiative lifetime of the transition ij in the host material and ϵ_h is the permittivity of the host medium. It is worth mentioning that the coupling coefficients κ_{ij} are derived from the the dipole matrix element between levels $|i\rangle$ and $|j\rangle$ as $\kappa_{ij} = 2\omega_{ij}\mu_{ij}^2/\hbar$ [105]. It is also essential to note that these values of coupling coefficients assume that all the dipoles of the active medium are fully aligned with the field. A more realistic scenario is that the dipoles are randomly oriented, and hence the values of the coupling coefficients are three times smaller.

The macroscopic polarization density $\mathbf{P}(\vec{r}, t)$ is coupled to the Maxwell equations through $\mathbf{D}(\vec{r}, t) = \epsilon_0\epsilon_h\mathbf{E}(\vec{r}, t) + \mathbf{P}(\vec{r}, t)$ where ϵ_0 is the free-space electric permittivity and ϵ_h is the relative permittivity of the host material. The rate equations, the macroscopic polarization driving equation, and the Maxwell equations are then solved in sync within a joined numerical multiphysics framework on a standard FDTD Yee grid, providing a detailed nonlinear interplay between the populations dynamics and local electromagnetic fields.

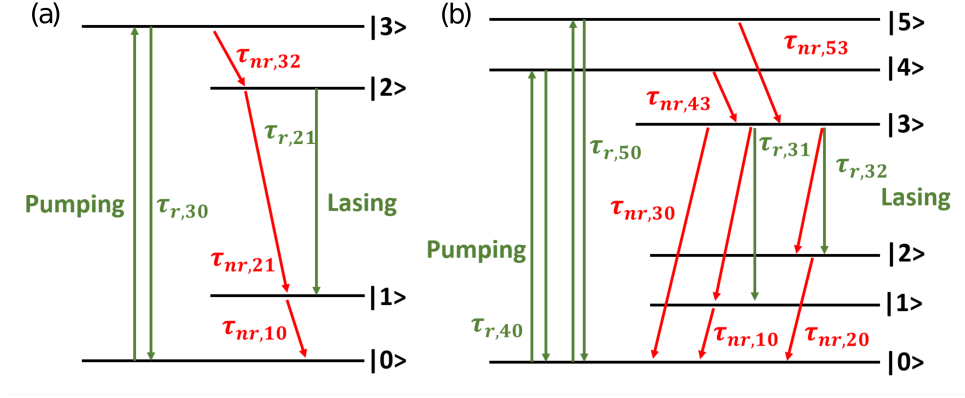


Fig. 4.1. Scheme of a population transfer process of the four-level (a) and six-level (b) systems for an optically excited dye molecule and the governing rate equations.

4.1.2 Six-level system

Spectra of more complex organic dyes exhibit multiple vibronic peaks. Therefore, their emission and/or absorption can't be modeled with a single Lorentzian as in the four-level system. We propose a more realistic six-level kinetic system that can take into account the effect of the non-negligible split transitions in such dyes. This provides a more physical and accurate description of a given gain medium, resulting in a better fit to the experimental measurements of absorption and emission spectra of a given host-embedded dye, which allows for a more detailed analysis of pump-probe experiment dynamics.

Figure 4.1 (b) shows the dominant considered transitions for the atoms/molecules modeled by the six-level kinetic system which are governed by the rate equations given in Eq. (4.4). Driving terms f_{ij} and macroscopic polarizations \mathbf{P}_{ij} are described by Eq. (4.2) and Eq. (4.3), respectively, with $ij \in \{31, 32, 40, 50\}$.

$$\begin{aligned}
\dot{N}_5 &= -(\tau_{53}^{-1} + \tau_{50}^{-1})N_5 + f_{50}, \\
\dot{N}_4 &= -(\tau_{43}^{-1} + \tau_{40}^{-1})N_4 + f_{40}, \\
\dot{N}_3 &= -(\tau_{30}^{-1} + \tau_{31}^{-1} + \tau_{32}^{-1})N_3 + \tau_{43}^{-1}N_4 + \tau_{53}^{-1}N_5 + f_{31} + f_{32}, \\
\dot{N}_2 &= -\tau_{20}^{-1}N_2 + \tau_{32}^{-1}N_3 + f_{32}, \\
\dot{N}_1 &= -\tau_{10}^{-1}N_1 + \tau_{31}^{-1}N_3 - f_{31}, \\
\dot{N}_0 &= \tau_{10}^{-1}N_1 + \tau_{20}^{-1}N_2 + \tau_{30}^{-1}N_3 + \tau_{40}^{-1}N_4 + \tau_{50}^{-1}N_5 - f_{40} - f_{50}.
\end{aligned} \tag{4.4}$$

Differences and similarities with respect to our four-level scheme are worth noting. Both absorption and emission initiate from the ground states of the vibronic structures of their electronic levels but may end at different vibronic levels (highly overlapping with the vibrational wave-function of the initial state). That is why we split only the final states of the electronic transitions. These states then quickly non-radiatively relax to their corresponding vibrational ground states. In principle, the relaxations from $|3\rangle$ to $|2\rangle$ and from $|3\rangle$ to $|1\rangle$ may have both radiative and non-radiative components, although by far the fastest non-radiative relaxation of the upper lasing level is from $|3\rangle$ to $|0\rangle$, to the bottom of the ground state of the lower electronic level. Similar to four-level scheme, the non-radiative parts of the transitions from $|5\rangle$ to $|0\rangle$ and $|4\rangle$ to $|0\rangle$ are neglected in our six-level system computations, but could be easily included. This simplification is of little consequence, as $|5\rangle$ to $|3\rangle$ and $|4\rangle$ to $|3\rangle$ pathways are typically much faster (and faster than the radiative relaxations to level $|0\rangle$ as well). Coupling between the induced macroscopic polarization and the Maxwell equations, as well as the numerical implementation of the system, is the same as in Sec. 2.1. Following the details of the numerical models presented in this Section, we will proceed with the results of the time-domain modeling of two different plasmonic systems in Section 3.

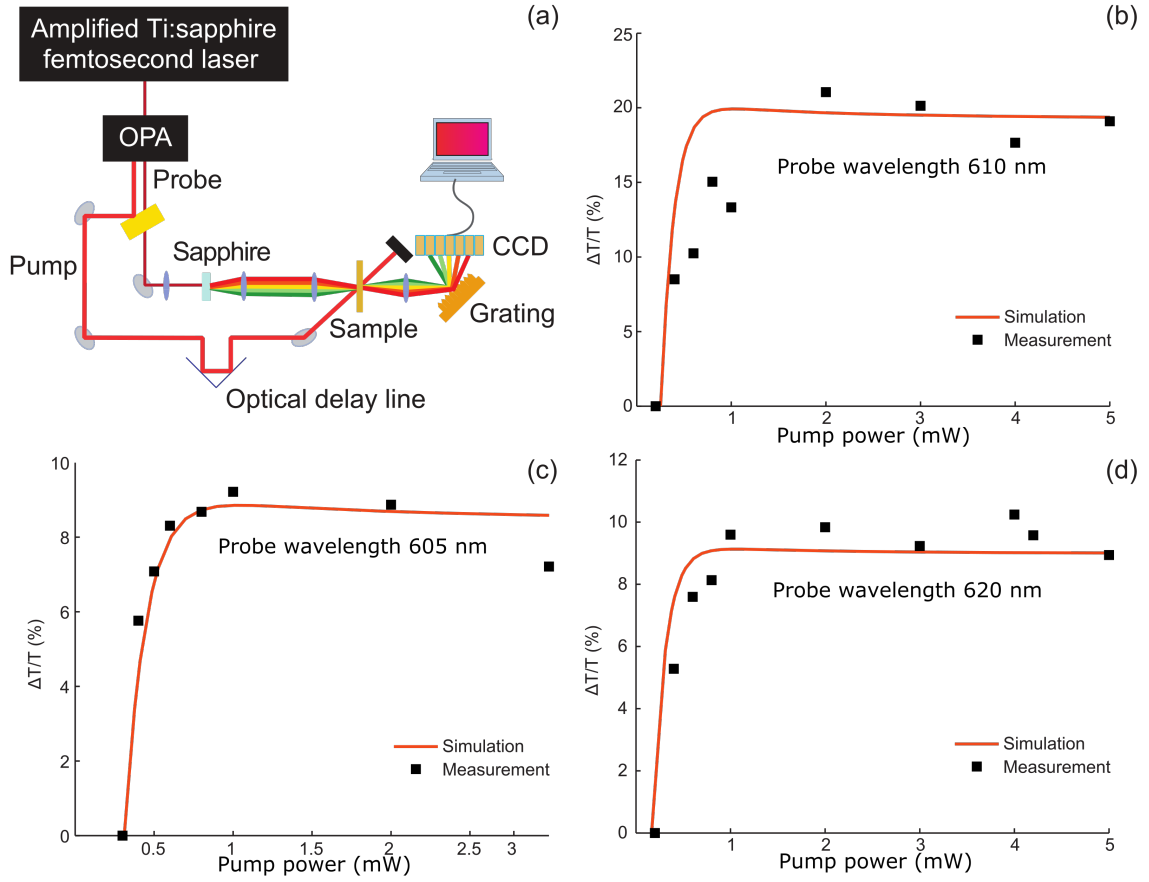


Fig. 4.2. (a) Pump-probe experimental setup, and saturated transmission results (both measurement and simulation) performed with pump wavelength at 595 nm and probe wavelength at (b) 605 nm, (c) 610 nm, and (d) 620 nm.

4.2 Results and discussion

4.2.1 Parameters retrieval using film transmission

The samples are R101 dye embedded in a thin film of polyvinyl alcohol (PVA) on an ITO-coated glass substrate and a Fluorescent Green dye in a thin Poly(methyl methacrylate) (PMMA) film on a glass substrate. The kinetic parameters of the R101-PVA and the Fluorescent Green-PMMA film samples are obtained by matching the pump-probe simulations with experiments as they are fitted to four-level and six-

level systems, respectively. The scheme for the pump-probe experiment is shown in Fig. 4.2(a) while the detailed setups are explained elsewhere [111]. The objective is to feed the retrieved kinetic parameters into a full-wave FDTD model to study the mechanism of the coupling between the plasmonic structures and the gain medium in the net amplification and lasing regimes.

The 2 μm -thick R101-PVA sample is illuminated by two beams, a 595 nm narrow band pump beam and femtosecond probe beam delayed by 2 ps . Total R101 chromophore density is 10 mM ($N = 6.0221 \times 10^{24} m^{-3}$). We calculate the differential transmittance $\Delta T/T$ by taking the difference of the measured transmission with and without pumping divided by the transmission without pumping. This treatment will minimize the influence of the background fluorescence effect, which is inevitable in experiments. To improve the fitting fidelity, we run multiple simulations at various pump powers and probe wavelengths. A collection of measurements with corresponding simulations is shown in Fig. 4.2(b)-(d). We retrieved the following four-level system parameters: transition wavelengths $\lambda_{30} = 575 \text{ nm}$ and $\lambda_{21} = 605 \text{ nm}$; dephasing times $T_{2,30} = 9 \text{ fs}$ and $T_{2,21} = 25.5 \text{ fs}$; decay times $\tau_{r,30} = 5 \text{ ns}$, $\tau_{nr,32} = 0.3 \text{ ps}$, $\tau_{r,21} = 6 \text{ ns}$, $\tau_{nr,21} = 7.33 \text{ ns}$, and, $\tau_{nr,10} = 0.35 \text{ ps}$. It is important to note that all simulations have been performed with parameters identical to those obtained from the experiment, which are: pump and probe pulses durations of 150 fs , a delay between the pump and probe signals of 2 ps and a repetition rate of 1000 Hz . Since there is no resonant feedback involved, we observe a saturation in transmission value with increasing pumping levels that is due to the saturation of pumping transition, which limits the inversion available to the lasing.

4.2.2 Dynamic processes in the metal nanoholes array with gain

Since dye emission characteristics can depend on the local environment, we re-evaluate the retrieved kinetic parameters for the gain medium incorporated in the nanoholes array. The updated kinetic parameters are crucial to the assessment of

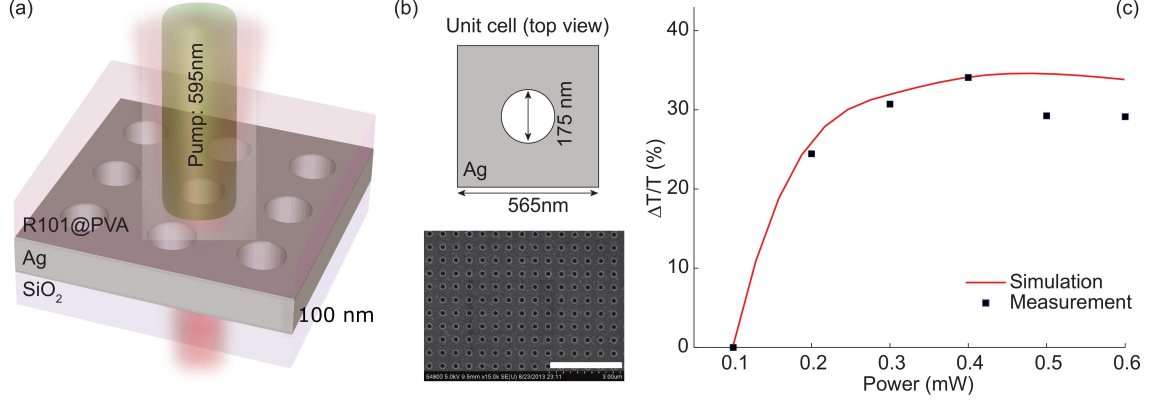


Fig. 4.3. (a) Schematic view of the silver nanoholes array structure covered by R101-PVA film (b) Top view of unit cell and SEM image of the fabricated sample (scale bar: $3 \mu\text{m}$) (c) Saturated transmission results of the nanoholes array structure (both measurement and simulation) performed with pumping wavelength at 595 nm and probing wavelength 605 nm .

the dynamic process of net amplification and lasing in the coupled system. The structure considered is an array of metal nanoholes with a periodicity of 565 nm , 175 nm diameter, and 100 nm thickness, which exhibits a resonance around 617 nm [89], close to the emission line (605 nm) of R101. A schematic of the structure and SEM image of the fabricated nanoholes array are shown in Fig. 4.3(a) and (b). The nanoholes array is made of silver with its permittivity modeled by a Drude-Lorentz response, which is implemented in the time domain through a generalized dispersion material (GDM) model [113]. The parameters of the Drude-Lorentz model for silver are adapted from an online database [114].

Due to the strong coupling between the pump pulse and gain medium, the plasmonic field enhancement affects the time dependence of the population inversion and subsequently increases the effective gain, leading to a dramatic increase in transmission. This results in rather fast gain saturation, on the order of 0.3 mW , as compared to 1 mW for the bare dye film (see Fig. 4.3(c) and Fig. 4.2(b)). The probe pulse forms SPP-Bloch waves at the interface between gain medium and silver

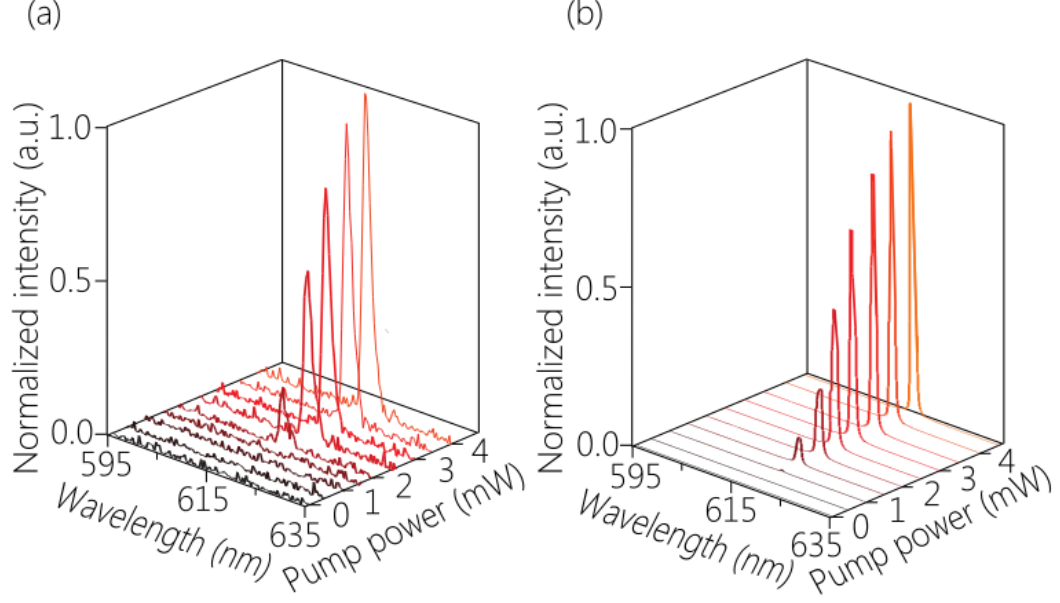


Fig. 4.4. Evolution of the emission spectra with increasing pumping power, (a) Experimental results, and (b) Simulations results.

nanoholes array, i.e., coherent constructive interference of SPP waves scattered at individual nanoholes [89]. This strong optical feedback introduces another plasmonic decay channel for the molecules in the excited state and hence depletes these states quickly. Therefore, the retrieval shows a more rapid non-radiative decay rate for the SP-gain coupled system, with the non-radiative lifetime of lasing transition $\tau_{nr,21}$ reduced from ~ 7 ns to ~ 4 ns, proving the existence of an additional decay channel due to the plasmonic coupling.

To study the dynamic processes in the metal nanoholes array with gain, we combine the systematic theoretical model described before with the experiments performed using the same configuration, as shown in Fig. 4.2(a). The silver nanoholes array is covered by the gain medium (R101-PVA film) with a thickness of $2 \mu m$, which we have previously reported to exhibit lasing [89]. The fitted simulation of

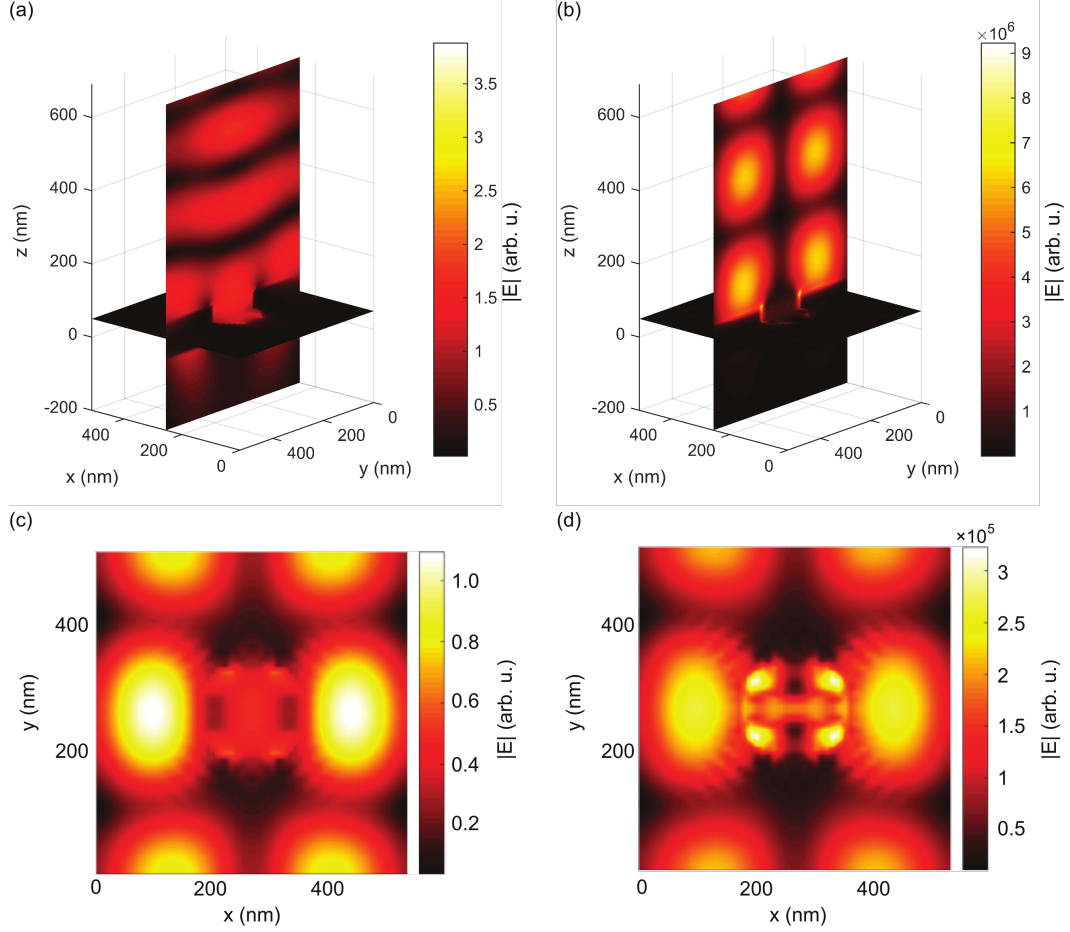


Fig. 4.5. The simulated electric field distribution at different pumping powers at the lasing wavelength (617 nm). Cross-section view of the time-averaged field distribution for pumping power of (a) 0.5 mW, (b) 3.5 mW. In-plane view of nanoholes array at $z=0$ nm for time-averaged field distribution at pumping power of (c) 0.5 mW, and (d) 3.5 mW.

the differential transmittance $\Delta T/T$ and the experimental measurement are shown in Fig. 4.3(c).

When the pump power increases, the experimentally measured emission remains at a noise level at first, and then exhibits a well-defined threshold behavior around 2 mW, as shown in Fig. 4.4(a). In Fig. 4.4(b) we simulate the interaction between the electromagnetic fields and the gain medium using the semi-classical framework,

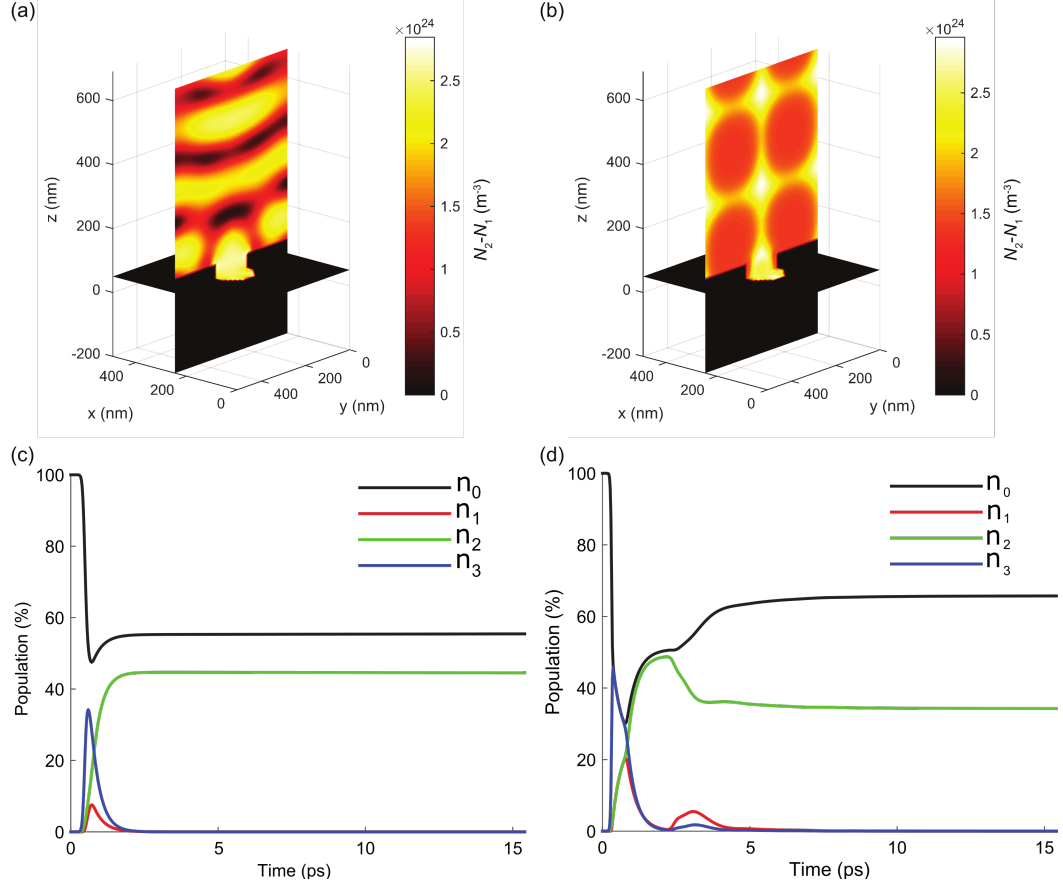


Fig. 4.6. The simulated results of the steady state population inversion distribution ($N_2 - N_1$) for pumping power of (a) 0.5 mW, (b) 3.5 mW; The time domain population evolution at the position ($x = 250$ nm, $y = 250$ nm, $z = 50$ nm) for pumping power of (c) 0.5 mW, and (d) 3.5 mW.

as explained in detail before. Normalized simulated emission spectra in Fig. 4.4(b) show a nonlinear increase of the self-emerging emission signal at 617 nm with pump power, in perfect match with experiment. Thus, the simulations accurately reproduce both the spectral and threshold behavior of the lasing emission. Furthermore, the calculations uncover the details of the temporal interaction between population inversion and electromagnetic fields in the lasing action. We perform a Fourier transform of the simulated time-domain emission field to obtain the time-averaged field amplitude distribution $|E(\vec{r})|$ at 617 nm and the population inversion $N_2(\vec{r}, t) - N_1(\vec{r}, t)$

at different levels of pumping power. For 3.5 *mW* pumping power (above threshold), the stimulated emission is several orders of magnitude higher than the spontaneously emitted electric fields for 0.5 *mW* pumping power (below threshold), as shown in Fig. 4.5. These findings confirm that the silver nanoholes array supports SPP-Bloch waves, which exhibit coherent constructive interference of SPP waves, and they are amplified by the gain medium. We further find that Fabry-Perot modes formed in the gain medium above the silver nanoholes array are amplified by six orders of magnitude (see Fig. 4.5(a),(b)). The hybridization of SPP-Bloch modes and photonic Fabry-Perot modes minimizes losses in the effective mode volume and supports coherent lasing emission. Below the threshold, a high population inversion is achieved in the system the regions with high electric fields (compare Fig. 4.5(a) and Fig. 4.6(a)). On the other hand, when the system is above threshold, the spatial profile of the population density ($N_2(\vec{r}, t) - N_1(\vec{r}, t)$) inversely correlates with the electromagnetic mode profile because of the inversion depletion by strong lasing fields (compare Fig. 4.5(b) and Fig. 4.6(b)). We further plot the temporal dynamics of the population density in the hot spots of electric fields in Fig. 4.6(c),(d). Below the lasing threshold, the population of the upper lasing level $|2\rangle$ stays at 45 % (the lower level $|1\rangle$ is almost empty). However, above the threshold, stimulated transitions in the strong localized electromagnetic fields produced by lasing deplete the population of the excited-state molecules from 48 % to 35 % of the total population.

4.2.3 Compensation of losses in Kretschmann-Raether configuration

In the second study, compensation of the SPP losses in the Kretschmann-Raether configuration [78] is analyzed. The retrieved kinetic parameters for the Fluorescent Green-PMMA film are fitted to the six-level atomic model (Fig. 4.1(b)) as follows. Transition wavelengths are $\lambda_{50} = 438 \text{ nm}$, $\lambda_{40} = 466 \text{ nm}$, $\lambda_{31} = 486 \text{ nm}$, and $\lambda_{32} = 513 \text{ nm}$. Dephasing time for all radiative transition is $T_2 = 10 \text{ fs}$ and decay times

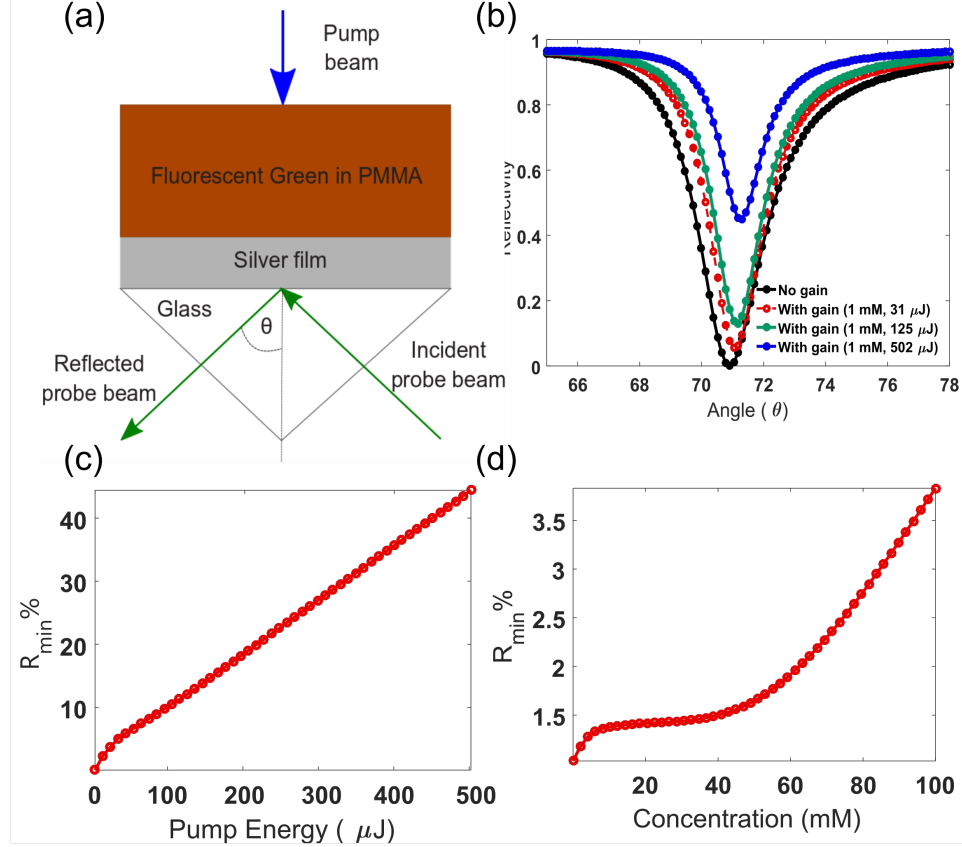


Fig. 4.7. (a) Schematic of the Kretschmann-Raether SPP excitation configuration. (b) Reflectivity at no gain and with gain at different pump energies. Dependence of the reflection minimum (R_{min}) on the (c) pump energy, and (d) dye molecule concentration.

are $\tau_{r,50} = 13 \text{ ns}$, $\tau_{r,40} = 55 \text{ ns}$, $\tau_{r,32} = 23 \text{ ns}$, $\tau_{r,31} = 84 \text{ ns}$, $\tau_{nr,53} = 1 \text{ ps}$, $\tau_{nr,43} = 1 \text{ ps}$, $\tau_{nr,32} = 300 \text{ ns}$, $\tau_{nr,31} = 300 \text{ ns}$, $\tau_{nr,30} = 2.9 \text{ ns}$, $\tau_{nr,20} = 1 \text{ ps}$ and, $\tau_{nr,10} = 1 \text{ ps}$.

The fitted system parameters are fed to a 2-D FDTD analysis of the experimental setup shown in Fig. 4.7(a). The structure is composed of a 500-nm layer of the Fluorescent Green dye in PMMA, coated on top of a 50-nm silver film. The prism is from the glass with a refractive index of 1.784, and the refractive index of the PMMA host is 1.5. The material properties of silver are taken from Johnson and Christy [115]. The dye is pumped at 438nm from the backside of the prism while the probe is incident through a glass prism. The pulse width for the pump signal is 1ps,

and for the probe, the signal is $10fs$, and the probe signal is delayed by $3ps$. For a $50-nm$ silver film, the SPP resonance condition at $513nm$ corresponds to an incidence angle of 70.9° , which is represented by the dip in the reflectivity curve shown in Fig. 4.7(b). The amount of loss compensation (SPP amplification) is a function of many factors that control how much gain is introduced to the system.

We study the effects of the concentration N of dye molecules and the pump energy on the system behavior. The passive system without gain exhibits a dip in reflectivity at $513nm$ and incidence angle of 70.9° with minimum reflection $R_{min} = 0.063\%$. Fixing the dye concentration at $1mM$ and varying the pump energy, the minimum reflection is enhanced by 11-fold at pump energy of $0.3\mu J$ and can go up to 44.4% , which is about 700-fold enhancement of the SPP dip at pump energy of $0.5mJ$, Fig. 4.7(b). The relation between R_{min} and the pump energy is shown in Fig. 4.7(c), which shows an almost linear dependence of R_{min} on the pump energy. Moreover, the dependence of R_{min} on the concentration of dye molecules is plotted in Fig. 4.7(d). We can conclude that the enhancement of the reflectivity with the change in concentration of the active media is not as strong as its dependence on the pump energy. $R_{min} = 3.83\%$ is observed at dye concentration as high as $100mM$ which corresponds approximately to 60-fold enhancement.

Temporal evolution of the macroscopic polarization and the population densities at all the six levels are recorded near the silver film and plotted in Fig. 4.8. The population inversion is achieved when $(N_3 - N_2) > 0$. The highlighted area in Fig. 4.8(b) shows the depletion of carriers in the upper lasing state N_3 from 57.8% to 52% , which corresponds to the energy transfer between the stored energy in the dye due to pumping and the SPP, which causes the amplification.

These findings can be elucidated by the frequency domain analysis, which shows that the introduction of gain increases the optimal Ag thickness for the minimal zero reflectivity from $50-nm$ to a thicker film. This minimum "can be thought of as being due to destructive interference between the totally reflected light and the light emitted by the SPP wave due to radiation damping", [116]. Gain decreases the internal

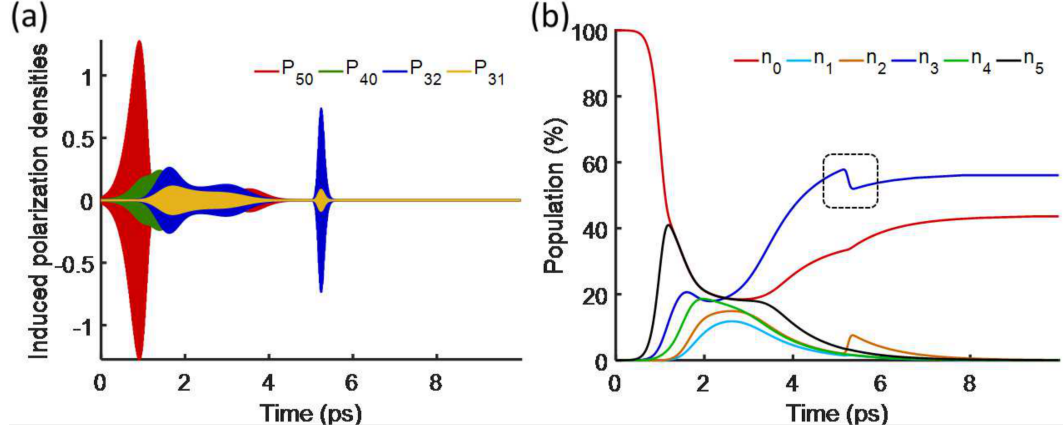


Fig. 4.8. Temporal dynamics of the (a) induced macroscopic polarizations, and (b) population densities at different levels. The dotted rectangle shows the energy transfer between the active medium and the SPP mode which is the essence of the loss compensation/amplification process.

damping of the surface plasmon on the PMMA-Ag interface. This necessitates the decrease of the "optimal radiative damping" that could be realized by the thickening of the Ag layer [117]. In addition, gain appreciably narrows the resonance, as the overall absorption of the system and its effective quality factor increase. These effects are observed with small to moderate gain values, insufficient to support reflective "lasing" in such a system.

Plasmon resonance corresponds to 0 in reflectance (R), or when the numerator of $R \rightarrow 0$. On the other hand, lasing corresponds to the pole in R , i.e., when $1/R \rightarrow 0$. Ideally, at higher active medium concentrations, the linear reflectivity goes to infinity, while absorption becomes infinitely negative, in full accord with the theory of scattering and absorption of spasers. A correct frequency domain analysis around the threshold should include saturation that makes all the quantities finite. In the present multiphysics time-domain framework, it is taken care of automatically with multi-level kinetic Eqs. (4.1) or (4.4). That makes the proposed numerical framework perfectly suitable for modeling spasers.

4.3 Conclusions

To conclude, we have studied the interaction between the light, plasmons, and gain media using a time-domain multiphysics numerical framework arranged of coupled kinetic equations for multi-level gain systems. We use calibrated kinetic parameters to investigate the net amplification and lasing behavior of two plasmon-enhanced gain systems. Our models predict amplification and fast gain saturation, which is induced by strong plasmonic coupling. As the pumping power increases, lasing emission and threshold behavior are obtained for the nanoholes array system, which is in excellent agreement with the experiment. The simulation further reveals the temporal details of the energy transfer process in the lasing regime. Such detailed and accurate models are necessary for understanding, predicting, and designing new types of nanoscale lasers and gain-compensated plasmonic systems. Based on this systematic approach, further studies could be applied to time-resolved physics of active plasmonic nanostructures. Our numerical framework can serve as a paradigm for in-depth investigation and optimal design of other metadevices coupled with gain. Since the MBL approach has not been implemented in our numerical models as of yet, we are planning to include the quantum fluctuations in future efforts specifically dealing with in-depth analysis of numerical metrics pertinent to enhanced spontaneous emission modeling. Future efforts may also include analysis of lasing dynamics in emerging two-dimensional materials.

5. TIME DOMAIN DYNAMICS OF REVERSE SATURABLE ABSORBERS WITH APPLICATION TO PLASMON-ENHANCED OPTICAL LIMITERS

5.1 Introduction

There has been a renewed interest in the optical community to protect optical sensors and more importantly human eyes from accidental or intentional harm caused by high-intensity light sources. This is accomplished by optical limiters, which have low absorption at low light intensities and high absorption at higher intensities. Multiple nonlinear processes could be utilized for optical limiting including nonlinear scattering, absorption, refraction, and multi-photon absorption [118]. Materials exhibiting nonlinear absorption, specifically reverse saturable absorption (RSA), are amongst the most popular for optical limiters [118]. RSA materials provide high transmission (low absorption) at low intensity of incident light, and low transmission when the intensity of incident light becomes high. Defined more rigorously, RSA occurs when the absorption cross-section of the excited states is larger than that of the ground states. RSA also requires the lifetime of the triplet state to be relatively long, which is reflected directly in the efficiency and the saturation intensity of the optical limiter. A wide range of materials that exhibit RSA includes metals [119], organic dyes [120,121], clustered metal particles [122,123], synthetic compounds [124], carbon nanotubes [125], and two-dimensional materials [126,127].

Unlike other nonlinear phenomena, there are surprisingly few efforts to develop complete multiphysics models of optical limiting devices based on RSA with resonant nanostructured optical elements. Such models would allow for the significant im-

This chapter is based on S. I. Azzam and A. V. Kildishev, “Time-domain dynamics of reverse saturable absorbers with application to plasmon-enhanced optical limiters,” *Nanophotonics*, vol. 8, no. 1, pp. 145–151, 2018, and is reproduced with publisher’s permissions.

provement of the size, weight and power metrics of this class of optical limiters. One of the most sought-after requirements is to obtain RSA at normal illumination levels, which would greatly expand their area of applicability such as protective eyewear, and automatically-dimmed windows [128, 129], and neuromorphic computing [130]. These models will also open up new opportunities for efficient RSA materials at a weak, incoherent light. Most RSA materials have extremely high saturation energies, defined as the energy required to reduce the linear transmittance to $1/e$ of its linear value. This limits the use of optical limiters based on those materials to very intense and/or very short laser pulses. Current efforts to optimize optical limiting properties are materials focused. Using material synthesis, chemical engineering and functionalization of materials to increase their triplet state lifetime have been widely explored to get enhanced RSA characteristics at sunlight power level [128, 129]. We believe that a critical limiting factor hindering the optimization and enhancement of optical limiters on the device level is the lack of material models that account for the quantum mechanical origin of RSA and its relevant representation in the time domain. Once an accurate model of RSA is available, boosting the performance of optical limiters using the current advances in nanophotonics and micro- and nano-fabrication should be made substantially more achievable. Thus far, there have been efforts to model saturable nonlinearities in the time domain using various methods such as a saturable harmonic oscillator [131] as well as two-level systems for saturable absorbers [132, 133]. For RSA, the physical mechanism causing the absorption is somewhat more involved and requires taking into account different time-scales as well as the absorption contributions of both the singlet and triplet states.

In this work, we propose an advanced time domain numerical simulation approach that models the RSA process as an atomic multi-level system in a 3D full-wave multi-physics framework. We integrate our material model as a proprietary ADE code in a commercial-grade solver based on the 3D finite-difference time-domain method. This approach allows for expanding the versatility of target problems through the advanced pre- and post-processing features of the commercial solver [71]. With this approach,

we can simulate the different relaxations taking place in the material and get an idea of how they affect the nonlinear optical material response. Additionally, we can also develop a deeper understanding of the excitation mechanisms, and then employ this comprehensive knowledge to optimize optical limiting devices and systems. Similar to the experiment-fitted time-domain kinetic models of gain media [134], feedback from optical experiments should always be recommended for accurate material modeling in the design and optimization of real-life RSA devices. Advantages of our scheme include: (i) self-consistent description of the excitation and relaxations dynamics, coupled to (ii) 3D full-wave multiphysics environment with the geometry discretization that can handle an arbitrary structural complexity, and accurately model focused/structured beams that match experimentally-used sources, without resorting to paraxial or non-paraxial approximations, and finally, (iii) in-depth post-processing of the simulated data – time-resolved tracking of E -fields, polarizations, and population kinetics – getting physical insights into the system dynamics not otherwise available through experiment. Moreover, we use our multiphysics framework to design the plasmon-enhanced optical limiter devices with an order of magnitude reduction in the saturation intensity. This is a critical improvement that brings the activation energies of the optical limiters to reduced illumination levels significantly expanding the area of application for these devices. Following this introduction, a particular topology of a multi-level atomic system for modeling RSA is introduced and explained with more details in Section 5.2. Then, the numerical framework and results obtained from the discretized models are discussed in Section 5.3. Time dynamics of the system along with the effects of controlling parameters on the system optical response are studied. Also, the results from our model are compared to the classical Beer-Lambert law by fitting the corresponding absorption cross-sections, thus verifying that our model reproduces the experimentally measured RSA data. Finally, two different designs of plasmon-assisted optical limiters are introduced and their saturation intensities are compared to that of a thin film of a given RSA material.

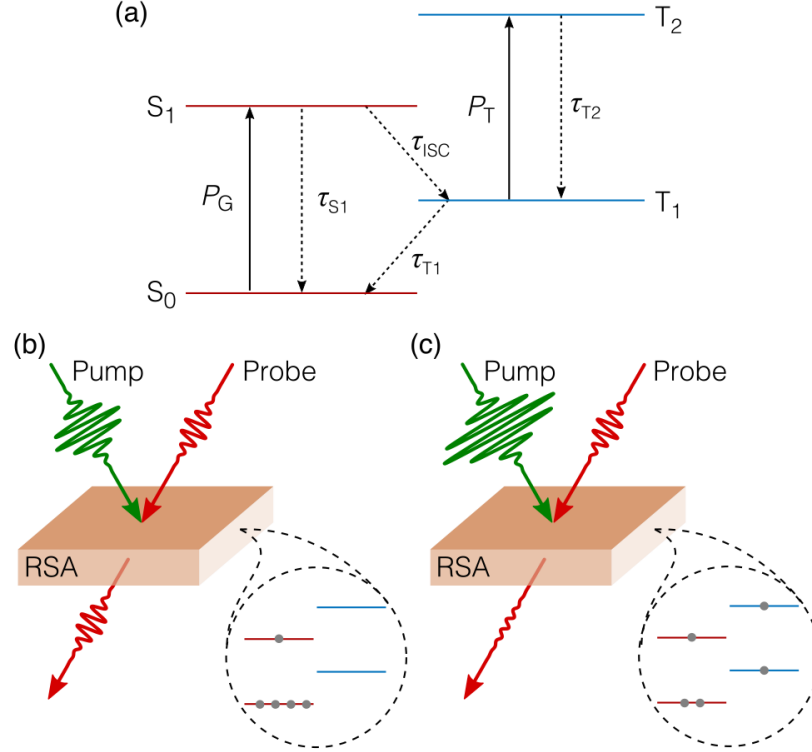


Fig. 5.1. RSA physical mechanism. (a) The Jablonski diagram of an absorbing medium represented by a four-level atomic system. $S_{0,1}$ and $T_{1,2}$ represent the singlet and triplet states respectively. (b) Linear regime: low-intensity pump with no sufficient population in the lower triplet state. (c) Nonlinear regime: high-intensity pump with absorption taking place in the triplet states leading to RSA behavior.

5.2 RSA models

The band diagram of a material with RSA can be represented by an atomic four-level system with the Jablonski diagram shown in Figure 5.1(a) [135]. When light illuminates an RSA medium, the atom is excited from the ground singlet state S_0 to the first singlet state S_1 by absorbing a photon of the incident light, Figure 5.1(b). The excited atom at S_1 can return back to S_0 by radiating the same photon or can exhibit an intersystem crossing (ISC) relaxation to the first triplet state T_1 . The atom at T_1 can either relax to S_0 or can be promoted to the second triplet state T_2

by absorbing a second photon if the incident light intensity is sufficient, Figure 5.1(c). The additional absorption associated with the elevations of atoms from T_1 to T_2 is the origin of the RSA. It can be thought of as an additional channel for absorption in addition to the ground state absorption channel (singlet pair) due to the match in their energy gap which is true for materials exhibiting RSA [120,121]. For the RSA to be efficient, a sufficient population of carriers should be transferred to T_1 , which requires efficient ISC and a long triplet state lifetime. Also, the absorption cross section of the excited triplet states must be larger than that of the ground singlet state.

5.2.1 Beer-Lambert's law

The Beer-Lambert law (BLL) is commonly used in spectroscopy and chemical analysis to relate the absorbance of a given absorbing material to its concentration in a host medium and the path length. The rate equations that model carrier kinetics at the different states are commonly employed to approximate the absorption coefficient of the materials [120,136,137]. Using the absorption coefficient with the BLL, the intensity decay in uniformly absorbing samples can be found. Assuming three allowed relaxations: intersystem crossing from S_1 to T_1 , relaxation from S_1 to S_0 and relaxation from T_1 to S_0 . The rate equations governing the transitions inside the material are given by:

$$\frac{dN_{S0}}{dt} = \frac{N_{S1}}{\tau_{S1}} + \frac{N_{T1}}{\tau_{T1}} - N_{S0} \frac{\sigma_G I}{\hbar \omega_0} \quad (5.1a)$$

$$\frac{dN_{S1}}{dt} = -\frac{N_{S1}}{\tau_{S1}} - \frac{N_{S1}}{\tau_{ISC}} + N_{S0} \frac{\sigma_G I}{\hbar \omega_0} \quad (5.1b)$$

$$\frac{dN_{T1}}{dt} = \frac{N_{S1}}{\tau_{ISC}} - \frac{N_{T1}}{\tau_{T1}} \quad (5.1c)$$

where N_{S0} , N_{S1} , and N_{T1} are the population densities in S_0 , S_1 , and T_1 , and where ω_0 is the frequency of the absorbed light. The time dependency of intensity in Eq.

(5.2) is omitted for simplicity. The intensity of the light inside the sample can then be calculated using:

$$\frac{\partial I}{\partial z} = -(N_{S0}\sigma_G + N_{T1}\sigma_T)I \quad (5.2)$$

where σ_G and σ_S are the ground state and the singlet state absorption cross-sections, respectively. Using this model, the time-dependent absorbance can be calculated, and the propagation of light intensity inside the sample can be straightforwardly obtained with a controlled accuracy and high efficiency even for tightly focused beams [136]. This approach, however, doesn't provide a material model that can be used to simulate more involved optical devices with dispersive or nonlinear materials and other multiphysics complications. Also, this simple, yet efficient, methodology does not allow access to the electric \mathbf{E} or magnetic \mathbf{H} vector fields, local population kinetics close to the device nanostructured boundaries, and may not account for pumping dynamics following structured illumination. All these limitations are addressed with our full-wave multiphysics numerical framework that includes a multi-level atomic model.

5.2.2 Four-level atomic system

As an example of a multi-level system, the atom or molecule of an RSA material is modeled using a four-level system with the Jablonski diagram shown in Figure 5.1(a). The rate equations that govern all allowed transitions in a four-level system are given by:

$$\frac{\partial N_{S0}}{\partial t} = \frac{N_{S1}}{\tau_{S1}} + \frac{N_{T1}}{\tau_{T1}} - \frac{1}{\hbar\omega_0} \mathbf{E} \cdot \frac{\partial \mathbf{P}_G}{\partial t} \quad (5.3a)$$

$$\frac{\partial N_{S1}}{\partial t} = -\frac{N_{S1}}{\tau_{S1}} - \frac{N_{S1}}{\tau_{ISC}} + \frac{1}{\hbar\omega_0} \mathbf{E} \cdot \frac{\partial \mathbf{P}_G}{\partial t} \quad (5.3b)$$

$$\frac{\partial N_{T1}}{\partial t} = -\frac{N_{T1}}{\tau_{T1}} + \frac{N_{S1}}{\tau_{ISC}} + \frac{N_{T2}}{\tau_{T2}} - \frac{1}{\hbar\omega_0} \mathbf{E} \cdot \frac{\partial \mathbf{P}_T}{\partial t} \quad (5.3c)$$

$$\frac{\partial N_{T2}}{\partial t} = -\frac{N_{T2}}{\tau_{T2}} + \frac{1}{\hbar\omega_0} \mathbf{E} \cdot \frac{\partial \mathbf{P}_T}{\partial t}. \quad (5.3d)$$

The population densities in the lower and upper singlet and triplet states, respectively, are N_{S0} , N_{S1} , N_{T1} , and N_{T2} . The total population, $N_d = N_{S0} + N_{S1} + N_{T1} + N_{T2}$, is

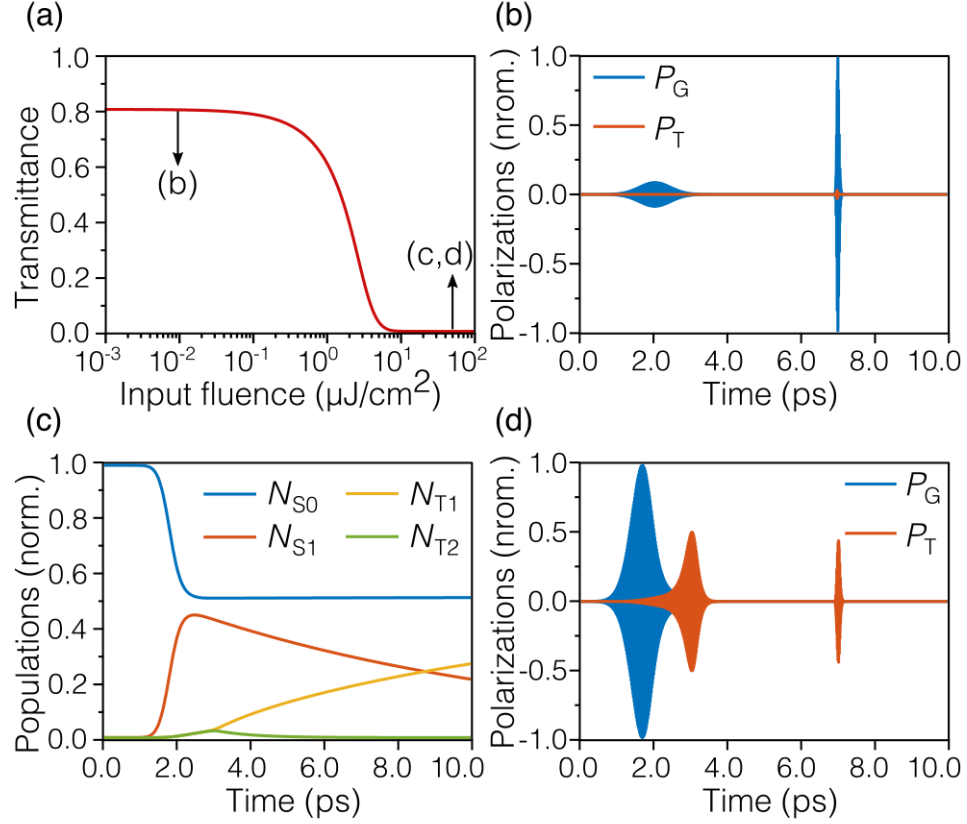


Fig. 5.2. RSA behavior and time dynamics of the four-level system. (a) Transmittance vs. input fluence of a $1\text{-}\mu\text{m}$ film (b) Induced polarizations densities inside the RSA at $0.01 \mu\text{J}/\text{cm}^2$, polarizations are governed by the ground state as the triplet state contribution in the linear regime is negligible (not shown). Nonlinear regime time dynamics for a pump fluence of $50 \mu\text{J}/\text{cm}^2$: (c) state densities and (d) polarizations.

conserved at all times, where N_d is the density of absorbing atoms. The lifetime of state S_1 is $1/(1/\tau_{S1} + 1/\tau_{ISC})$ where τ_{ISC} is the intersystem crossing lifetime. Lifetimes of the upper and lower triplet states are τ_{T2} and τ_{T1} . The term $\frac{1}{\hbar\omega_0} \mathbf{E} \cdot \frac{\partial \mathbf{P}_{ij}}{\partial t}$ represents the stimulated emission and absorption between levels $|i\rangle$ and $|j\rangle$.

The induced macroscopic polarizations due to the transitions satisfy the Lorentz ordinary differential equation given by:

$$\frac{\partial^2 \mathbf{P}_{ij}}{\partial t^2} + \gamma_{ij} \frac{\partial \mathbf{P}_{ij}}{\partial t} + \omega_0^2 \mathbf{P}_{ij} = \kappa_{ij} (N_j - N_i) \mathbf{E} \quad (5.4)$$

where γ_{ij} is the dephasing constant between levels $|i\rangle$ and $|j\rangle$. The energy spacing between the levels is $\Delta E_{S10} \approx \Delta E_{T21} = \hbar\omega_0$. The excitation term in Eq. (5.4) is proportional to product of the local electric field and the difference in populations between the upper and the lower levels of this transition with a proportionality constant κ_{ij} where $ij \in \{G, T\}$. The coupling coefficient κ_{ij} represents the dipole matrix element between levels $|i\rangle$ and $|j\rangle$ and is given by $\kappa_{ij} = 2\omega_{ij}|\mu_{ij}|^2/\hbar = 6\pi\epsilon_0 c^3/\omega_{ij}^2\tau_{ij}$, where ϵ_0 and c are the free space permittivity and speed of light, respectively, and τ_{ij} is the decay time constant between levels $|i\rangle$ and $|j\rangle$ [138, 139]. The polarization densities are then coupled to the Maxwell equations through the electric flux,

$$\nabla \times \mathbf{H}(t, \mathbf{r}) = \epsilon_0 \epsilon_h \frac{\partial \mathbf{E}(t, \mathbf{r})}{\partial t} + \frac{\partial \mathbf{P}(t, \mathbf{r})}{\partial t} \quad (5.5)$$

$$\nabla \times \mathbf{E}(t, \mathbf{r}) = -\mu_0 \frac{\partial \mathbf{H}(t, \mathbf{r})}{\partial t}, \quad (5.6)$$

and Eqs. (5.3)-(5.6) are solved simultaneously using a full-wave solver on a staggered Yee grid by applying the classical central finite-difference approximation to the spatial and time derivatives [72, 139]. The time dependent electromagnetic fields are recorded and converted to frequency domain using fast Fourier transform to obtain the transmission and reflection, and finally the absorption.

5.3 Numerical Details and Results

A dielectric 1 μm -thin film is modeled using the proposed four-level atomic model in a host medium with refractive index of 1. The life-time and scattering rate parameters of the model are: $\tau_{T2} = 1$ ps, $\tau_{T1} = 300$ ns, $\tau_{S1} = 1$ ns, $\tau_{ISC} = 10$ ps, and $\gamma_G = \gamma_T = 10^{14}$ Hz. The density of the absorptive molecules is 0.3 mM ($1.806 \times 10^{17} cm^{-3}$) and the $\omega_0 = 2\pi/\lambda_0$ where λ_0 is 532 nm. The sample is illuminated with two plane-wave, normally-incident pulses separated by a short delay of 5 ps: a strong 1-ps pump pulse followed by a weak 50-fs probe. The probe fluence is fixed at $100 nJ/cm^2$ while the fluence of the pump is varied from $10^{-3} \mu J/cm^2$ to $10^2 \mu J/cm^2$ to study the nonlinear transmission and absorption of the thin RSA film.

The wavelengths of both the pump and the probe are 532 *nm*. Transmission and reflection monitors are placed at least half-wavelength separation from the sample and the source. Spatial grid size are set to 10-*nm* inside the RSA medium. Figure 5.2 shows the RSA behavior and time dynamics of the thin film. In Figure 5.2(a), the transmission is linear (constant transmittance) at a low input (pump) fluence and nonlinear at higher values, the saturation fluence for the RSA film is around 2.5 $\mu J/cm^2$ in this example. The time dynamics of the system at two pump fluences of $10^{-2} \mu J/cm^2$ and 50 $\mu J/cm^2$ are depicted in Figure 5.2(b-d). At $10^{-2} \mu J/cm^2$, well into the linear regime, the normalized ground state population density is almost unity during all times, and consequently, the carrier build-up in the upper states is negligible (not shown). The time evolution of the macroscopic polarization densities of the ground (P_G), and excited triplet (P_T) states are shown in Figure 5.2(b) and, as expected, P_T is almost negligible in this case. All polarizations are normalized to the maximum value of P_G for clarity. Further, in the nonlinear regime with a pump fluence of 50 $\mu J/cm^2$, the carrier dynamics, Figure 5.2(c), show depopulation of the ground state and increased build-up of triplet state density, hence, P_T starts to contribute to the material response, Figure 5.2(d). We can clearly notice that the response of the system to the probe (around 7 *ps*) is completely dominated by the P_T which explains the enhanced absorption in this case.

Crossings of molecules from S_1 to T_1 requires undergoing a spin conversion in a process called intersystem crossing [140]. The efficiency of the intersystem crossing is determined by the triplet quantum yield $\Phi_T = (1/\tau_{ISC} + 1/\tau_{S1})/\tau_{ISC}$. The faster the intersystem rate ($1/\tau_{ISC}$), the higher the triplet quantum yield. Here, the effect of Φ_T on the system response is studied. The same sample as before is used while varying the intersystem crossing lifetimes to 1, 10, 100 and 1000 *ps* corresponding to Φ_T of 0.999, 0.99, 0.909, and 0.5, respectively. Transmittance versus input fluence at the four different cases is depicted in Figure 5.3(a). It can be noticed that for τ_{ISC} of 1, 10, and 100 *ps*, the material shows RSA behavior with increasing saturation fluence. However, at τ_{ISC} of 1 *ns*, the material acts as a saturable absorber. This matches the

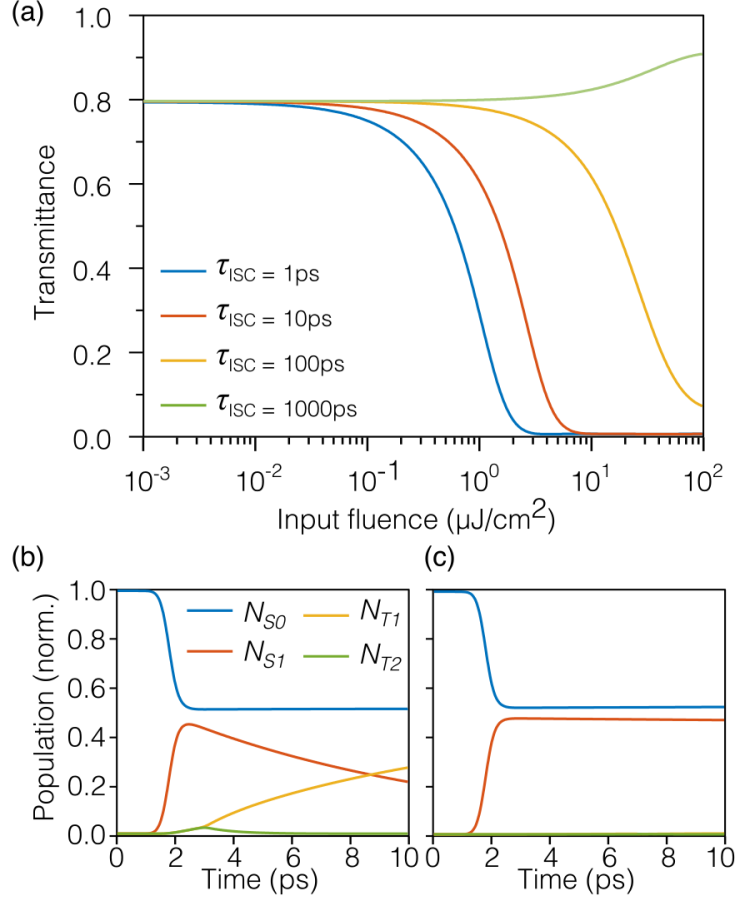


Fig. 5.3. Effect of triplet quantum yield on the RSA efficiency. (a) Transmittance vs. pump fluence at four different values of τ_{ISC} : 1, 10, 100 and 1000 *ps* corresponding to Φ_T of 0.999, 0.99, 0.909, and 0.5, respectively. (b), and (c) the population time dynamics at 10, and 1000 *ps* at pump energy of $50 \mu\text{J}/\text{cm}^2$.

system dynamics very well. As seen in Figure 5.3(b), at τ_{ISC} of 10 *ps*, the efficiency of the triplet quantum yield is high enough to allow for a sufficient population transfer to T_1 unlike at τ_{ISC} of 1 *ns*, Figure 5.3(c), where the population density at T_1 is almost negligible, and as a result, the carrier density at S_1 starts to saturate leading to saturation of system absorption and hence to increased transmission (see the green line in Figure 5.3(a)).

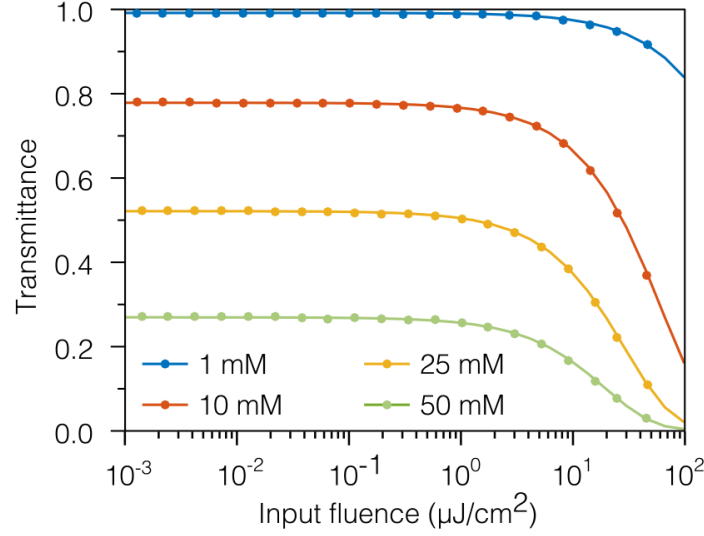


Fig. 5.4. Transmittance vs. pump fluence using full-wave atomic system simulations (solid lines) and BLL (dotted lines) at different molecule densities.

Next, we compare the results of a $1\text{-}\mu\text{m}$ -thin RSA film with varying N_d using a four-level atomic model and the classical BLL. The lifetimes of the films are $\tau_{T2} = 1\text{ ps}$, $\tau_{T1} = 1\text{ }\mu\text{s}$, $\tau_{S1} = 30\text{ ns}$, and $\tau_{ISC} = 0.1\text{ ns}$. The same lifetimes are used in both simulations while changing the absorption cross-sections to fit the two models. The fitted absorption cross-sections are $\sigma_G = 5.2 \times 10^{-20}\text{ m}^{-3}$ and $\sigma_S = 9 \times 10^{-15}\text{ m}^{-3}$. Figure 5.4 shows excellent agreement between the full-wave simulation (solid lines) and the BLL equations (dotted lines) calculations. Generally, the BLL has been successfully used to fit experimental results [136, 137] of uniform samples. Having an excellent match with the BLL implies the ability of our model to fit and further utilize experimentally measured RSA transmission data. From figure 5.4, the saturation intensity as well as the linear transmittance increases with decreasing molecular absorption densities which suggest the use of thinner films with larger N_d in optical limiters device engineering.

5.3.1 Plasmon-enhanced optical limiters

Reducing the light intensity required for activating optical limiters is crucial for the expanding their area of application. For example in protective goggles, optical limiter devices should be activated at normal levels of the incoherent light illumination. From RSA materials standpoint, this translates to a very long triplet lifetime. Thus far, most of the development in this direction has been focused on developing materials with these favorable properties. In addition to this, here we use the multi-level material models developed for RSA to optimize optical limiting devices where due to the local field enhancement from plasmonic structures, the nonlinear response from RSA materials is further intensified. This way, the light intensity required for activating a given RSA device is greatly reduced. As a proof of concept, we design two plasmonic structures with an embedded RSA material to study the reduction in the saturation energy. Figure 5.5(a) shows the RSA material, with the same parameters as before, with thickness d of 200 nm on top of a silver grating. The bottom silver film is 20-nm thin (t_2) and the periodic ridges of the grating are 10-nm high (t_1) and 50-nm wide (w). The pitch of the grating structure (Λ) is 500 nm, and the optical properties of silver are obtained from [115]. The second configuration is depicted in Fig. 5.5 (b) illustrating the same 200-nm RSA layer sandwiched between two silver films with thickness h of 10-nm. The geometrical parameters of the grating and the cavity are specifically chosen based on several parametric sweeps to maximize the linear transmission while reducing the saturation intensity. Spatial grid size are set to 10-nm inside the RSA medium and to 2.5 nm inside the silver. The linear transmittance is 0.93 in the case of bare RSA film, 0.46 in the case of RSA film on a grating, and 0.68 in the case of the RSA layer inside a cavity-like structure. Figure 5.5(c) shows the normalized transmittance as a function of the input fluence of all three structures: a bare 200-nm RSA, the 200-nm RSA film on a grating and the 200-nm RSA inside a cavity-like structure. The transmittance in each case is normalized to its maximum for more straightforward comparison. As observed in

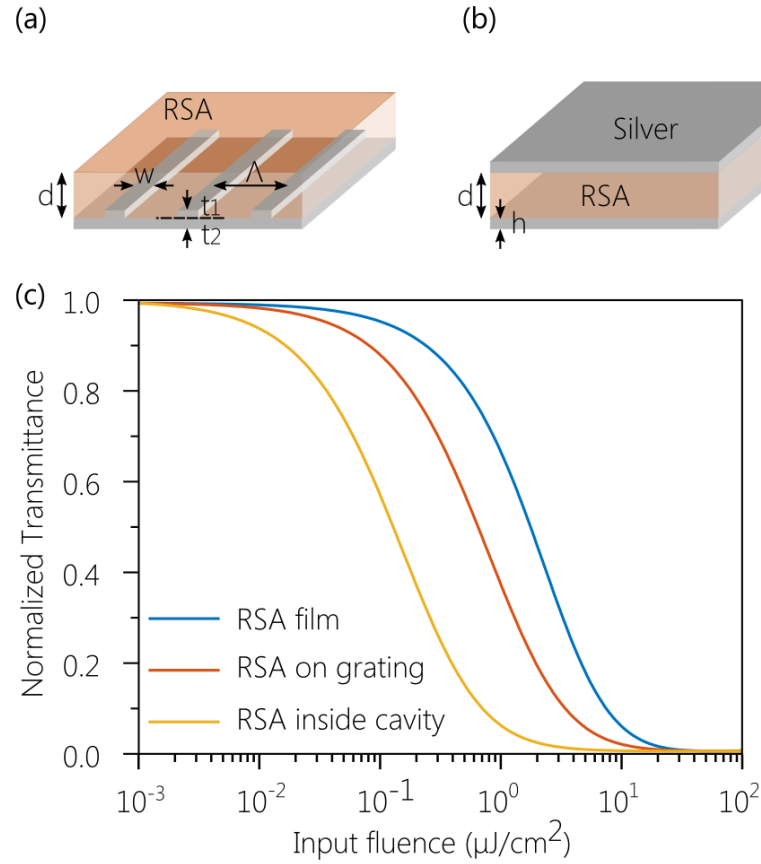


Fig. 5.5. Enhancement of optical limiters using plasmonic structures. RSA thin film of 200 nm thickness (a) coated on top of a silver grating and (b) sandwiched between two thin silver layers. (c) Normalized transmittance vs. pump fluence for all three configurations: bare RSA thin film, the same film on top of a silver grating, and same RSA film between two thin silver layers.

Fig. 5.5 (c), the saturation intensity for the bare RSA film is $2.651 \mu\text{J}/\text{cm}^2$, for the RSA film on a grating is $1.019 \mu\text{J}/\text{cm}^2$, and for the RSA film in a cavity-like structure is $0.2006 \mu\text{J}/\text{cm}^2$. This is a 2.6-fold reduction in the saturation intensity for the grating structure and 13.2-fold reduction in the cavity configuration.

5.4 Conclusion

A 3D full-wave analysis of the RSA devices with the ability to model light-matter interaction based on rate equations that could include non-paraxial structured beams, complex photonic structures with diverse material composition has been presented and validated. The results of the proposed model agree well with the classical Beer-Lambert equation used to fit the experimental RSA data while also providing a comprehensive physical understanding of the fields' and carriers' dynamics within the absorbing material. Examples of two plasmon-enhanced optical limiters that utilize the field enhancement to lower the saturation intensity are proposed. More than one order of magnitude reduction of the light fluence required to activate the RSA structures with plasmonic elements is achieved. Using our technique, the numerical modeling and optimization of the devices with complex micro- and nano-structured materials and illumination are made possible, which opens up new opportunities to explore high-sensitivity, low-threshold optical limiters beyond homogeneous RSA light-matter limitations. Future work will include other important effects into our model such as the Pauli exclusion principle for more accurate representation of RSA materials.

6. TIME-DOMAIN DYNAMICS OF SATURATION OF ABSORPTION USING MULTILEVEL ATOMIC SYSTEMS

6.1 Introduction

A saturable absorber (SA) is a material with a nonlinear absorption coefficient that decreases as the incident light intensity increases. When the low-intensity light is incident on the SA, a photon is absorbed, and a carrier is excited from the ground to a higher energy atomic level causing the absorption of light, Fig. 6.1(a). The material can still absorb more photons due to the abundance of absorbent carriers in the ground state. However, if the excited-state lifetime is long enough and the intensity of light is increasing, so that the excited-state carriers are not decaying fast enough to participate in the absorption process again, while more carriers are getting excited, the saturation of absorption occurs (Fig. 6.1(b)). SAs find applications in passive mode-locking [21] and Q-switching [22]. A broad range of materials exhibit saturable absorption including 2D materials such as graphene [141], carbon nanotubes [142], topological insulators [143], as well as dielectric [144] and metallic nanoparticles [145]. However, full-wave analysis of saturable absorption has been limited to either phenomenological descriptions that ignore transient response or simple models that do not account for multiphysics material response. The overall objective of this study is to provide a generalized time-domain (TD) coupled-physics method for numerical simulations of the saturation of absorption in a complex (e.g., nanopatterned, dispersive, and illuminated with a structured light) three-dimensional (3D) material systems. The availability of such a modeling tool can provide means to design and optimize nanophotonic structures that can engineer the nonlinear spatiotemporal light-matter

This chapter is based on S. I. Azzam and A. V. Kildishev, “Time-domain dynamics of saturation of absorption using multilevel atomic systems,” *Optical Materials Express*, vol. 8, no. 12, pp. 3829–3834, 2018, and is reproduced with publisher’s permissions.

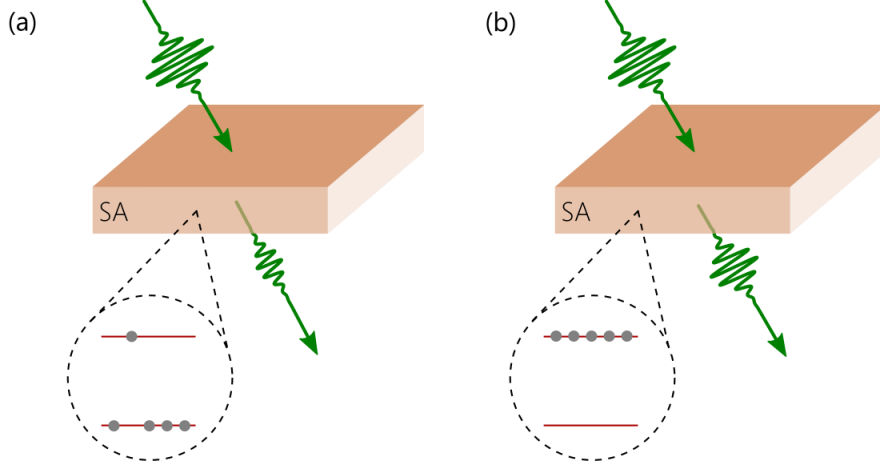


Fig. 6.1. Saturable absorption in a dielectric thin film modeled by a two-level system at: (a) low input fluence and (b) high input fluence where the ground state carriers are depleted and the excited-state lifetime is too long to allow for reabsorption.

interaction, and thus, control the functionality of the entire system. Following our objective, we explore the kinetics of the spatially-dependent carrier population and the coherent absorption using a set of rate equations (RE) derived for the multilevel system. The proposed technique simulates an averaged nonlinear material response as a polarization vector in a multiphysics simulation framework. Within this framework, the Maxwell equations are coupled with the RE – a set of spatially-dependent auxiliary differential equations (ADE) [105] – and share the same simulation domain, along with the same temporal and spatial discretization. A salient feature of the carrier kinetics model integrated into our simulation framework is that it offers a critical ability to predict multiple absorption peaks in the absorbing medium.

Following this introduction, we organize the rest of the chapter as follows: Section 6.2 introduces and provides details on different SA models built on two- and four-level transition topologies. Section 6.2 presents the analysis of thin-film dielectric SAs modeled using either two- or four-level atomic systems within our new multiphysics

framework with the multilevel RE-ADE. The results of the study are summarized in Conclusions.

6.2 Saturable absorption models

Saturable absorption is commonly modeled using a phenomenological description to account for the intensity dependence of the absorption of a material given by:

$$\alpha(I) = \frac{\alpha_0}{1 + \frac{I}{I_s}}, \quad (6.1)$$

where $\alpha(I)$ is the intensity-dependent material absorption coefficient, α_0 is the low-intensity absorption coefficient, I is the light intensity and I_s is the saturation intensity of the material.

This model puts forward many limitations, including the lack of a comprehensive description of the fundamental physics, the assumption of instantaneous response, which is nonphysical, lack of any direct access to electric or magnetic fields inside the medium, and the complete inability to predict the temporal dynamics of a saturable absorber. To overcome these shortcomings, more physics-based models built on the population kinetics with the REs have been introduced [146, 147]. Initially, only steady-state solutions were considered in those studies [146, 147]. An important nonlinear generalization of the Lorentz model has been applied by Varin et al. to model 2nd and 3rd-order optical nonlinearity [131, 148] with FDTD. Recently, Mock et al. made a vital contribution to modeling the saturation of absorption for a 2D material in the TD [149].

In this section, we propose and discuss two TD ADE models for SAs based on two- and four-level atomic systems. The proposed four-level system can reproduce multiple absorption peaks based on the nature of the material and the application. We integrate our material model as a proprietary ADE code in the commercial-grade solver based on the 3D FDTD method [71].

6.2.1 Two-level saturable absorption atomic model

The saturable absorbing material is modeled using a two-level system, depicted in Fig. 6.2(a). The transition between the two levels is governed by:

$$\frac{dN_1}{dt} = -\frac{N_1}{\tau} + \frac{1}{\hbar\omega_0} \mathbf{E} \cdot \frac{d\mathbf{P}}{dt}, \quad (6.2)$$

where N_1 is the population density of the excited-state carriers, N_0 is the population density of carriers in the ground state, with the total population density of absorbing carriers N_t being conserved, $N_t = N_0 + N_1$, τ is the lifetime of the material, ω_0 is the frequency of the absorbed light defined by the energy difference between the two levels, and \hbar is the reduced Planck constant.

The macroscopic polarization resulting from this transition takes a Lorentzian form with a source term being dependent on the difference of the population density in the ground and excited levels:

$$\frac{d^2\mathbf{P}_{10}}{dt^2} + \gamma_{10} \frac{d\mathbf{P}_{10}}{dt} + \omega_0^2 \mathbf{P}_{10} = \kappa(N_0 - N_1)\mathbf{E}, \quad (6.3)$$

where \mathbf{P}_{10} is the average macroscopic polarization vector and which is a function of time and space. The damping factor of this oscillator is γ_{10} , and it is a summation of all sources of damping in the material, such as dephasing, and the transition frequency is ω_0 . The coupling factor κ takes the form $\kappa = 6\pi\epsilon_0 c^3 / (\tau\omega_0^2 \sqrt{\epsilon_h})$ where ϵ_h is the permittivity of the host medium [139].

Using a standard FDTD Yee grid, the rate equation, the macroscopic polarization driving equation, and Maxwell's equations are solved numerically, providing a complete spatiotemporal description of the nonlinear interplay between the population dynamics and electromagnetic fields [105]. This description offers comprehensive insights into a detailed physical picture of the system. It gives access to numerous time-resolved functional dependencies of the internal dynamics that are not attain-

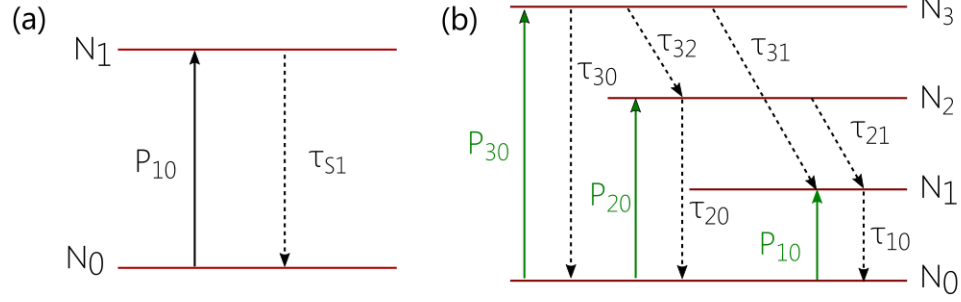


Fig. 6.2. Jablonski diagrams of (a) two-level and (b) four-level atomic systems showing the allowed transitions and the corresponding lifetimes.

able otherwise. Following the ADE technique, the macroscopic polarization vector is coupled to Maxwell's equations through:

$$\mathbf{D} = \epsilon_0 \epsilon_h \mathbf{E} + \sum_m \mathbf{P}_m, \quad (6.4)$$

where ϵ_0 is the permittivity of free-space, and \mathbf{P}_m is the polarization induced by the m^{th} oscillator.

6.2.2 Four-level saturable absorption atomic model

Some absorbing materials exhibit more than one absorption peak, which cannot be captured by either a two-level atomic model in the TD or simpler SA models in the frequency domain. For an extended representation of the absorption spectra, we expand the two-level model to four-levels and demonstrate the appearance of three different absorption peaks. Since such an expansion is very generic, it can be adjusted for an arbitrary number of peaks with an appropriate topology of levels. Such a model also has the flexibility of controlling the spectral width, position, and strength of each

absorption peak individually. The Jablonski diagram of a four-level atomic system is depicted in Fig. 6.1(b). The RE system governing these transitions are given by:

$$\begin{aligned}\frac{dN_3}{dt} &= -\frac{N_3}{\tau_{30}} - \frac{N_3}{\tau_{31}} - \frac{N_3}{\tau_{32}} + \frac{1}{\hbar\omega_{30}}\mathbf{E} \cdot \frac{d\mathbf{P}_{30}}{dt}, \\ \frac{dN_2}{dt} &= -\frac{N_2}{\tau_{20}} - \frac{N_2}{\tau_{21}} + \frac{N_3}{\tau_{32}} + \frac{1}{\hbar\omega_{20}}\mathbf{E} \cdot \frac{d\mathbf{P}_{20}}{dt}, \\ \frac{dN_1}{dt} &= -\frac{N_1}{\tau_{10}} + \frac{N_2}{\tau_{21}} + \frac{N_3}{\tau_{31}} + \frac{1}{\hbar\omega_{10}}\mathbf{E} \cdot \frac{d\mathbf{P}_{10}}{dt},\end{aligned}\tag{6.5}$$

where N_1 , N_2 , N_3 , and N_4 are the population density of carriers in the different energy levels. The system describes the absorption of the incident light at different frequencies, ω_{30} , ω_{20} , and ω_{10} , as well as the rapid decay of the excited-state population from higher levels to lower energy levels due to non-radiative relaxations. The transition lifetime between levels i and j is τ_{ij} , as shown in Fig. 6.2(b). The macroscopic polarizations induced as a result of these transitions are:

$$\frac{d^2\mathbf{P}_{ij}}{dt^2} + \gamma_{ij}\frac{d\mathbf{P}_{ij}}{dt} + \omega_{ij}^2\mathbf{P}_{ij} = \kappa_{ij}(N_j - N_i)\mathbf{E},\tag{6.6}$$

where $ij \in \{30, 20, 10\}$, \mathbf{P}_{ij} is the macroscopic polarization vector formed between levels i and j . γ_{ij} and κ_{ij} are the ij -oscillator's damping coefficient and the coupling factor, respectively. The Maxwell equations are solved using the FDTD method [105], along with the REs, Eq. 5, and the polarization densities, Eq.6 within a joint multiphysics framework as mentioned earlier.

6.3 Results and analysis

Figure 6.3 illustrates the analysis of a 200-nm SA with a dielectric constant of 2.25 using the two-level model. We use a lifetime (τ_{S1}) of 1 ps, a transition wavelength of 532 nm, a damping rate (γ_{10}) of 10^{14} rad/s, and a concentration of 10 mM. The absorption of the film decreases as the input fluence increase, as depicted in Fig. 6.3(a). The saturation fluence of the SA, defined as the fluence required to reduce the absorption to $1/e$ of its linear value, is 87 J/cm^2 . Figure 6.3(b-d) illustrates the

time dynamics of the system. We plot the internal system dynamics at different input fluences: 6 J/cm^2 where the system is unsaturated and still linear and 94 J/cm^2 in the nonlinear regime. Figure 6.3(b) illustrates a time-dependent behavior of macroscopic polarization \mathbf{P}_{10} in both linear and nonlinear cases showing the relative increase in its magnitude. Figure 6.3(c) shows the time evolution of unsaturated normalized carrier population densities in the upper and lower energy levels, N_1 and N_0 . Figure 6.3(d) shows a significant difference in the carrier population dynamics. Once the incoming light elevates more carriers to the upper energy levels, it causes a decrease in the available population pool and, hence, absorption saturation. Therefore, the two-level system gives us access to the numerous details of internal time-dynamics that help understand the physics and further engineer the response of more complex systems. Next, we study the dependence of the absorption on the SA film thickness and the concentration of absorbing carriers. Figure 6.4(a) shows the increase of the linear absorption with increasing the film thickness. The absorption increases from 0.46 for a 100-nm film to a 0.94 for a 500-nm one. The saturation intensity shifts with the thickness increase from 81 J/cm^2 for the 100 nm film to 126 J/cm^2 for the 500 nm film. The effect of the carrier concentration on absorption is also explored. As anticipated, as the carrier concentration increases, the absorption increases. Figure 6.4(b) shows the increase of the linear absorption from 0.145 for 1 mM concentration to 0.87 for 20 mM, and I_s increase from 51 J/cm^2 for 1 mM concentration to 115 J/cm^2 for 20 mM.

Using the four-level atomic system, we simulate the absorption in a 100-nm SA with a carrier concentration of 0.1 mM and the absorption central wavelengths being, $\lambda_{30} = 450 \text{ nm}$, $\lambda_{20} = 550 \text{ nm}$, and $\lambda_{10} = 650 \text{ nm}$. The damping coefficients for each Lorentzian are $\gamma_{30} = \gamma_{20} = \gamma_{10} = 2\pi \times 10^{14} \text{ rad/s}$, while the life-times are $\tau_{30} = \tau_{20} = \tau_{10} = 10 \text{ ps}$, $\tau_{32} = 1 \text{ ps} = \tau_{31} = 1 \text{ ps}$ and $\tau_{21} = 10 \text{ fs}$. Figure 6.5(a) depicts the simulated absorption spectrum showing three peaks at the selected wavelengths. The bandwidth of each peak, along with its amplitude, can be controlled using the model parameters. At 1 J/cm^2 , the time-dependent carrier population in all four levels is given in Fig.

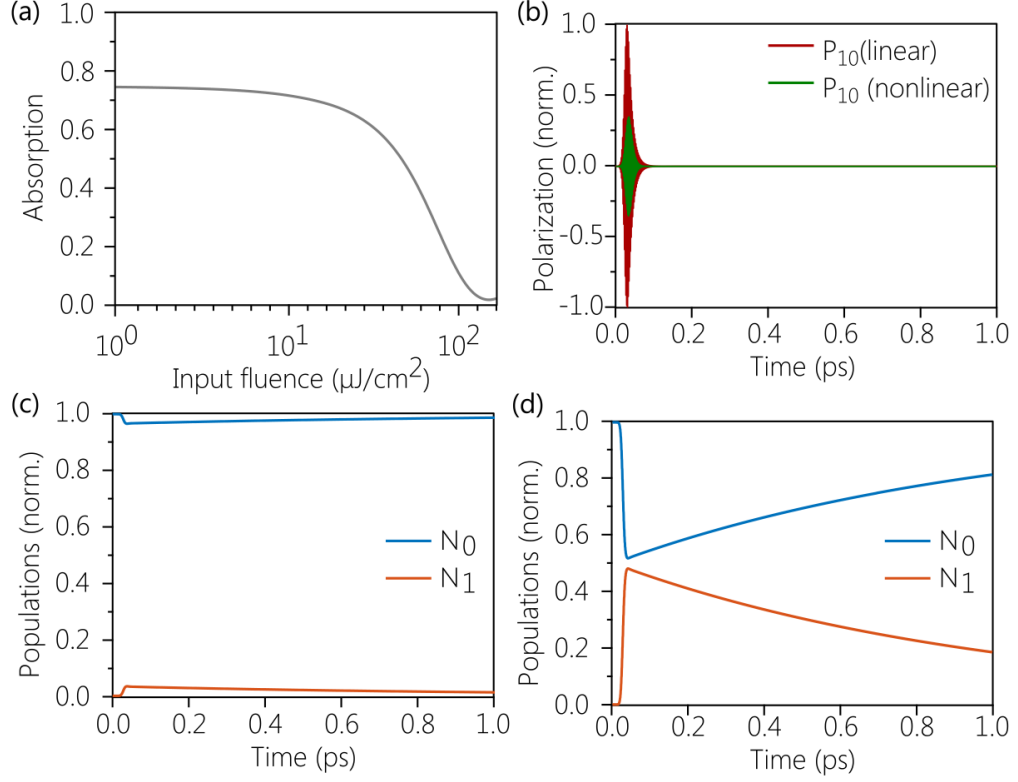


Fig. 6.3. Dynamics of a dielectric SA modeled using the two-level system. (a) Absorption vs. input fluence showing the saturation of absorption. (b) Time-dependent normalized macroscopic polarization \mathbf{P}_{10} in both linear and nonlinear cases. Time evolution of carrier population density in (c) linear ($6 \text{ J}/\text{cm}^2$) and (d) nonlinear ($94 \text{ J}/\text{cm}^2$) regimes.

6.5(b) showing the decrease in the ground state population density N_0 , which accounts for the absorption reduction. The normalized macroscopic polarization as a function of time are shown in Fig. 6.5(c) indicating the relative amplitudes of the material response.

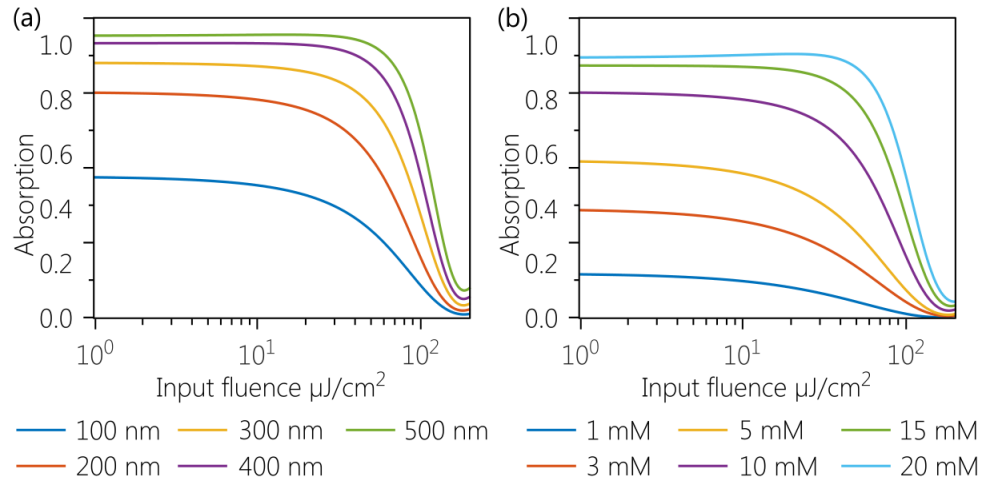


Fig. 6.4. Dependence of the absorption on the (a) film thickness and (b) carriers' concentrations.

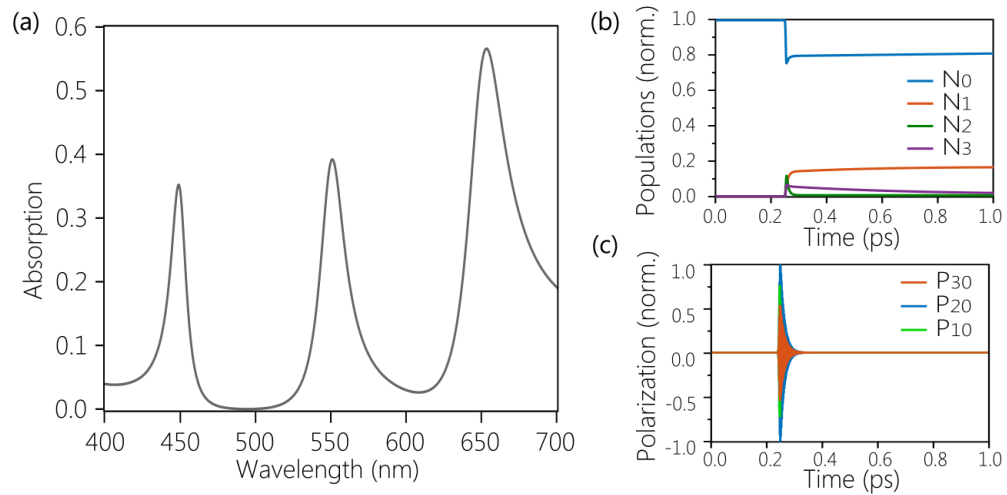


Fig. 6.5. An SA dielectric film modeled using the four-level system. (a) The absorption spectrum shows three peaks at the selected wavelengths. Time-dependent (b) carrier population densities and (c) normalized polarizations at an input fluence of $1 \text{ J}/\text{cm}^2$

6.4 Conclusions

We proposed a hybrid FDTD-RE modeling approach to explore the saturation of absorption as the interplay of the carrier population kinetics in a multilevel atomic system with classical electromagnetic fields. This versatile modeling approach is built upon the ADE technique that allows adding polarization driven by different underlying physics, accounting for multiple material dynamics. Our multiphysics framework opens up access to a complete spatiotemporal picture of the entire nonlinear system, which is not attainable otherwise. This framework could enable a further comprehensive understanding of the foundations of the materials physics and empower the accurate optimization of nonlinear photonic devices.

7. SUMMARY

This thesis deals with the engineering, localization, and modeling of light at the nanoscale.

In the first part of this thesis, we have demonstrated the formation of BICs in a hybrid photonic-plasmonic system with a realistic intrinsic loss. By engineering the interactions of two sets of modes with distinct natures, plasmonic modes and photonic modes, the strong coupling can be observed with large Rabi splitting. The destructive interference of the photonic and the plasmonic modes, the losses are significantly reduced due to suppression of radiation. Two different types of BICs are achieved in the hybrid plasmonic-photonic system due to the symmetry incompatibility with the radiation as well as the destructive reactions of resonances, the Friedrich-Wintgen BIC. A distinct characteristic of the Friedrich-Wintgen BIC realized in this thesis is that it originates from the interference of two resonances with different natures. The system studied exhibits an exquisite set of phenomena including the formation of localized states with, in principle, infinite lifetimes, strong coupling with large Rabi splitting, optical bandgap engineering and slow light with broad spectral robustness. Such resonances find a wide range of applications ranging from low-threshold lasers, sharp spectral filters, enhancement of nonlinear phenomena as well as sensors.

Following that, in a different study, we explore the interplay of electric and magnetic dipoles in arrays of dielectric nanoresonators to enhance light-matter interaction. We reported on the experimental realization of high-Q factor resonances in the visible through the collective diffractive coupling of electric and magnetic dipoles. Providing direct physical insights, we also show that coupling the Rayleigh anomaly of the array with the electric and magnetic dipoles of the individual nanoresonators can result in the formation of different types of BICs. We utilized the resonances in the visible regime to achieve lasing action at room temperature with high spatial direc-

tionality and low threshold. Besides, we experimentally demonstrated multi-mode, directional lasing and study the BIC-assisted lasing mode engineering in arrays of dielectric nanoresonators. We believe that our results enable a new range of applications in flat photonics through realizing on-chip controllable single and multi-wavelength micro-lasers.

The second part of the thesis proposes an advanced 3D full-wave framework to model the nonlinear interaction of light and matter. Using the rate equation to model the carrier kinetics inside the material, we are able to obtain a full spatio-temporal picture of the material response. This approach has been applied to model different nonlinear phenomena such as gain and net amplification, saturable absorption, and reverse saturable absorption. Such a framework will provide critical insights into the design of transformative photonic devices and their complementary optical characterization, and serve as an invaluable utility for guiding the development of synthetic absorbing materials. We believe that the developed multiphysics models are crucial enabling tools that lay a necessary foundation for numerical machinery required for the realization and optimization of nonlinear devices.

Future directions can include the utilization of the field localization provided by the various types of BICs to enhance nonlinear effects. This may lead to efficient on-chip nonlinearities at chip-compatible power levels that can be used for all-optical computing and signal processing. Another exciting direction is the exploration of BIC-assisted lasing at different types of BIC supported by a single structure and the switchability between them. This could enable a new class of on-chip controllable single and multi-wavelength micro-lasers that would be invaluable for many applications.

REFERENCES

REFERENCES

- [1] Z. F. Sadrieva, I. S. Sinev, K. L. Koshelev, A. Samusev, I. V. Iorsh, O. Takayama, R. Malureanu, A. A. Bogdanov, and A. V. Lavrinenko, “Transition from optical bound states in the continuum to leaky resonances: role of substrate and roughness,” *ACS Photonics*, vol. 4, no. 4, pp. 723–727, 2017.
- [2] C. W. Hsu, B. Zhen, A. D. Stone, J. D. Joannopoulos, and M. Soljačić, “Bound states in the continuum,” *Nature Reviews Materials*, vol. 1, no. 9, p. 16048, 2016.
- [3] L. Fonda, “Resonance reactions and continuous channels,” *Annals of Physics*, vol. 12, no. 3, pp. 476–484, 1961.
- [4] —, “Bound states embedded in the continuum and the formal theory of scattering,” *Annals of Physics*, vol. 22, no. 1, pp. 123–132, 1963.
- [5] S. I. Azzam, V. M. Shalaev, A. Boltasseva, and A. V. Kildishev, “Formation of bound states in the continuum in hybrid plasmonic-photonic systems,” *Physical Review Letters*, vol. 121, no. 25, p. 253901, 2018.
- [6] M. V. Rybin, K. L. Koshelev, Z. F. Sadrieva, K. B. Samusev, A. A. Bogdanov, M. F. Limonov, and Y. S. Kivshar, “High-Q supercavity modes in sub-wavelength dielectric resonators,” *Physical Review Letters*, vol. 119, no. 24, p. 243901, 2017.
- [7] E. N. Bulgakov and D. N. Maksimov, “Topological bound states in the continuum in arrays of dielectric spheres,” *Physical Review Letters*, vol. 118, no. 26, p. 267401, 2017.
- [8] C. W. Hsu, B. Zhen, J. Lee, S.-L. Chua, S. G. Johnson, J. D. Joannopoulos, and M. Soljačić, “Observation of trapped light within the radiation continuum,” *Nature*, vol. 499, no. 7457, pp. 188 – 191, 07 2013.
- [9] A. Kodigala, T. Lepetit, Q. Gu, B. Bahari, Y. Fainman, and B. Kanté, “Lasing action from photonic bound states in continuum,” *Nature*, vol. 541, no. 7636, p. 196, 2017.
- [10] J. Lee, B. Zhen, S.-L. Chua, W. Qiu, J. D. Joannopoulos, M. Soljačić, and O. Shapira, “Observation and differentiation of unique high-q optical resonances near zero wave vector in macroscopic photonic crystal slabs,” *Physical Review Letters*, vol. 109, no. 6, p. 067401, 2012.
- [11] A. Krasnok and A. Alú, “Embedded scattering eigenstates using resonant metasurfaces,” *Journal of Optics*, vol. 20, no. 6, p. 064002, 2018.
- [12] F. Monticone and A. Alú, “Embedded photonic eigenvalues in 3D nanostructures,” *Physical Review Letters*, vol. 112, no. 21, p. 213903, 2014.

- [13] H. Friedrich and D. Wintgen, “Interfering resonances and bound states in the continuum,” *Physical Review A*, vol. 32, no. 6, p. 3231, 1985.
- [14] A. Christ, S. G. Tikhodeev, N. A. Gippius, J. Kuhl, and H. Giessen, “Waveguide-plasmon polaritons: strong coupling of photonic and electronic resonances in a metallic photonic crystal slab,” *Physical Review Letters*, vol. 91, no. 18, p. 183901, 2003.
- [15] S. Tikhodeev, N. Gippius, A. Christ, T. Zentgraf, J. Kuhl, and H. Giessen, “Waveguide-plasmon polaritons in photonic crystal slabs with metal nanowires,” *Physica Status Solidi*, vol. 2, no. 2, pp. 795–800, 2005.
- [16] J. Bravo-Abad, S. Fan, S. G. Johnson, J. D. Joannopoulos, and M. Soljacic, “Modeling nonlinear optical phenomena in nanophotonics,” *Journal of Light-wave Technology*, vol. 25, no. 9, pp. 2539–2546, 2007.
- [17] L. Caspani, R. Kaipurath, M. Clerici, M. Ferrera, T. Roger, J. Kim, N. Kinsey, M. Pietrzyk, A. Di Falco, V. M. Shalaev *et al.*, “Enhanced nonlinear refractive index in ϵ -near-zero materials,” *Physical Review Letters*, vol. 116, no. 23, p. 233901, 2016.
- [18] M. Z. Alam, S. A. Schulz, J. Upham, I. De Leon, and R. W. Boyd, “Large optical nonlinearity of nanoantennas coupled to an epsilon-near-zero material,” *Nature Photonics*, vol. 12, no. 2, p. 79, 2018.
- [19] O. Reshef, E. Giese, M. Z. Alam, I. De Leon, J. Upham, and R. W. Boyd, “Beyond the perturbative description of the nonlinear optical response of low-index materials,” *Optics Letters*, vol. 42, no. 16, pp. 3225–3228, 2017.
- [20] R. W. Boyd, *Nonlinear optics*. Elsevier, 2003.
- [21] E. Ippen, C. Shank, and A. Dienes, “Passive mode locking of the cw dye laser,” *Applied Physics Letters*, vol. 21, no. 8, pp. 348–350, 1972.
- [22] J. A. Morris and C. R. Pollock, “Passive Q switching of a diode-pumped Nd:YAG laser with a saturable absorber,” *Optics Letters*, vol. 15, no. 8, pp. 440–442, 1990.
- [23] S. I. Azzam, J. Fang, J. Liu, Z. Wang, N. Arnold, T. A. Klar, L. J. Prokopenko, X. Meng, V. M. Shalaev, and A. V. Kildishev, “Exploring time-resolved multi-physics of active plasmonic systems with experiment-based gain models,” *Laser & Photonics Reviews*, vol. 13, no. 1, p. 1800071, 2019.
- [24] S. I. Azzam and A. V. Kildishev, “Time-domain dynamics of reverse saturable absorbers with application to plasmon-enhanced optical limiters,” *Nanophotonics*, vol. 8, no. 1, pp. 145–151, 2018.
- [25] —, “Time-domain dynamics of saturation of absorption using multilevel atomic systems,” *Optical Materials Express*, vol. 8, no. 12, pp. 3829–3834, 2018.
- [26] J. von Neumann and E. Wigner, “On some peculiar discrete eigenvalues,” *Phys. Z.*, vol. 465, 1929.
- [27] Y. Plotnik, O. Peleg, F. Dreisow, M. Heinrich, S. Nolte, A. Szameit, and M. Segev, “Experimental observation of optical bound states in the continuum,” *Physical Review Letters*, vol. 107, no. 18, p. 183901, 2011.

- [28] N. Moiseyev, “Suppression of Feshbach resonance widths in two-dimensional waveguides and quantum dots: a lower bound for the number of bound states in the continuum,” *Physical Review Letters*, vol. 102, no. 16, p. 167404, 2009.
- [29] Y. Yang, C. Peng, Y. Liang, Z. Li, and S. Noda, “Analytical perspective for bound states in the continuum in photonic crystal slabs,” *Physical Review Letters*, vol. 113, no. 3, p. 037401, 2014.
- [30] V. Liu, M. Povinelli, and S. Fan, “Resonance-enhanced optical forces between coupled photonic crystal slabs,” *Optics Express*, vol. 17, no. 24, pp. 21 897–21 909, 2009.
- [31] X. Gao, C. W. Hsu, B. Zhen, X. Lin, J. D. Joannopoulos, M. Soljačić, and H. Chen, “Formation mechanism of guided resonances and bound states in the continuum in photonic crystal slabs,” *Scientific Reports*, vol. 6, p. 31908, 2016.
- [32] E. N. Bulgakov and A. F. Sadreev, “Bound states in the continuum in photonic waveguides inspired by defects,” *Physical Review B*, vol. 78, no. 7, p. 075105, 2008.
- [33] D. C. Marinica, A. G. Borisov, and S. V. Shabanov, “Bound states in the continuum in photonics,” *Physical Review Letters*, vol. 100, no. 18, p. 183902, 2008.
- [34] J. Gomis-Bresco, D. Artigas, and L. Torner, “Anisotropy-induced photonic bound states in the continuum,” *Nature Photonics*, vol. 11, no. 4, p. 232, 2017.
- [35] F. Dreisow, A. Szameit, M. Heinrich, R. Keil, S. Nolte, A. Tünnermann, and S. Longhi, “Adiabatic transfer of light via a continuum in optical waveguides,” *Optics letters*, vol. 34, no. 16, pp. 2405–2407, 2009.
- [36] Y. V. Kartashov, V. V. Konotop, and L. Torner, “Bound states in the continuum in spin-orbit-coupled atomic systems,” *Physical Review A*, vol. 96, no. 3, p. 033619, 2017.
- [37] L. S. Li, J. Zhang, C. Wang, N. Zheng, and H. Yin, “Optical bound states in the continuum in a single slab with zero refractive index,” *Physical Review A*, vol. 96, no. 1, p. 013801, 2017.
- [38] Y.-X. Xiao, G. Ma, Z.-Q. Zhang, and C. T. Chan, “Topological subspace-induced bound state in the continuum,” *Physical Review Letters*, vol. 118, no. 16, p. 166803, 2017.
- [39] Y.-X. Xiao, Z.-Q. Zhang, and C. Chan, “A band of bound states in the continuum induced by disorder,” *Scientific Reports*, vol. 8, no. 1, p. 5160, 2018.
- [40] H. M. Döeleman, F. Monticone, W. den Hollander, A. Alù, and A. F. Koenderink, “Experimental observation of a polarization vortex at an optical bound state in the continuum,” *Nature Photonics*, vol. 12, no. 7, pp. 397–401, 2018.
- [41] L. Carletti, K. Koshelev, C. De Angelis, and Y. Kivshar, “Giant nonlinear response at the nanoscale driven by bound states in the continuum,” *Physical Review Letters*, vol. 121, p. 033903, Jul 2018.

- [42] F. Monticone, H. M. Doeleman, W. Den Hollander, A. F. Koenderink, and A. Alù, “Trapping light in plain sight: Embedded photonic eigenstates in zero-index metamaterials,” *Laser & Photonics Reviews*, vol. 12, no. 5, p. 1700220, 2018.
- [43] S. Weimann, M. Kremer, Y. Plotnik, Y. Lumer, S. Nolte, K. Makris, M. Segev, M. Rechtsman, and A. Szameit, “Topologically protected bound states in photonic parity–time-symmetric crystals,” *Nature Materials*, vol. 16, no. 4, p. 433, 2017.
- [44] S. T. Ha, Y. H. Fu, N. K. Emani, Z. Pan, R. M. Bakker, R. Paniagua-Domínguez, and A. I. Kuznetsov, “Directional lasing in resonant semiconductor nanoantenna arrays,” *Nature nanotechnology*, vol. 13, no. 11, pp. 1042–1047, 2018.
- [45] S. I. Azzam, K. Chaudhuri, V. M. Shalaev, A. Boltasseva, and A. V. Kildishev, “High q-factor all-dielectric metasurface based on bound states in the continuum,” in *CLEO: QELS_Fundamental Science*. Optical Society of America, 2019, pp. JTh2A–119.
- [46] K. Koshelev, S. Sychev, Z. F. Sadrieva, A. A. Bogdanov, and I. Iorsh, “Strong coupling between excitons in transition metal dichalcogenides and optical bound states in the continuum,” *Physical Review B*, vol. 98, no. 16, p. 161113, 2018.
- [47] B. Min, E. Ostby, V. Sorger, E. Ulin-Avila, L. Yang, X. Zhang, and K. Vahala, “High-Q surface-plasmon-polariton whispering-gallery microcavity,” *Nature*, vol. 457, no. 7228, p. 455, 2009.
- [48] B. D. Thackray, P. A. Thomas, G. H. Auton, F. J. Rodriguez, O. P. Marshall, V. G. Kravets, and A. N. Grigorenko, “Super-narrow, extremely high quality collective plasmon resonances at telecom wavelengths and their application in a hybrid graphene-plasmonic modulator,” *Nano Letters*, vol. 15, no. 5, pp. 3519–3523, 2015.
- [49] R. F. Oulton, V. J. Sorger, T. Zentgraf, R.-M. Ma, C. Gladden, L. Dai, G. Bartal, and X. Zhang, “Plasmon lasers at deep subwavelength scale,” *Nature*, vol. 461, no. 7264, p. 629, 2009.
- [50] Y. Gong and J. Vučković, “Design of plasmon cavities for solid-state cavity quantum electrodynamics applications,” *Applied Physics Letters*, vol. 90, no. 3, p. 033113, 2007.
- [51] W. Zhu, T. Xu, H. Wang, C. Zhang, P. B. Deotare, A. Agrawal, and H. J. Lezec, “Surface plasmon polariton laser based on a metallic trench fabry-perot resonator,” *Science Advances*, vol. 3, no. 10, p. e1700909, 2017.
- [52] V. J. Sorger, R. F. Oulton, J. Yao, G. Bartal, and X. Zhang, “Plasmonic fabry-pérot nanocavity,” *Nano Letters*, vol. 9, no. 10, pp. 3489–3493, 2009.
- [53] S. J. Kress, J. Cui, P. Rohner, D. K. Kim, F. V. Antolinez, K.-A. Zaininger, S. V. Jayanti, P. Richner, K. M. McPeak, D. Poulikakos *et al.*, “A customizable class of colloidal-quantum-dot spasers and plasmonic amplifiers,” *Science Advances*, vol. 3, no. 9, p. e1700688, 2017.

- [54] S. I. Azzam, V. M. Shalaev, A. Boltasseva, and A. V. Kildishev, “Strong coupling and bound states in the continuum in hybrid photonic-plasmonic structure,” in *CLEO: QELS_Fundamental Science*. Optical Society of America, 2019, pp. FF2A–6.
- [55] W. L. Barnes, T. W. Preist, S. C. Kitson, and J. R. Sambles, “Physical origin of photonic energy gaps in the propagation of surface plasmons on gratings,” *Physical Review B*, vol. 54, no. 9, p. 6227, 1996.
- [56] Z. Yu, A. Raman, and S. Fan, “Fundamental limit of nanophotonic light trapping in solar cells,” *Proceedings of the National Academy of Sciences*, vol. 107, no. 41, pp. 17 491–17 496, 2010.
- [57] E. N. Bulgakov and A. F. Sadreev, “Bloch bound states in the radiation continuum in a periodic array of dielectric rods,” *Physical Review A*, vol. 90, no. 5, p. 053801, 2014.
- [58] M. F. Limonov, M. V. Rybin, A. N. Poddubny, and Y. S. Kivshar, “Fano resonances in photonics,” *Nature Photonics*, vol. 11, no. 9, p. 543, 2017.
- [59] Z. Yu, X. Xi, J. Ma, H. K. Tsang, C.-L. Zou, and X. Sun, “Photonic integrated circuits with bound states in the continuum,” *Optica*, vol. 6, no. 10, pp. 1342–1348, 2019.
- [60] K. Koshelev, S. Kruk, E. Melik-Gaykazyan, J.-H. Choi, A. Bogdanov, H.-G. Park, and Y. Kivshar, “Subwavelength dielectric resonators for nonlinear nanophotonics,” *Science*, vol. 367, no. 6475, pp. 288–292, 2020.
- [61] A. Leitis, A. Tittl, M. Liu, B. H. Lee, M. B. Gu, Y. S. Kivshar, and H. Altug, “Angle-multiplexed all-dielectric metasurfaces for broadband molecular fingerprint retrieval,” *Science Advances*, vol. 5, no. 5, p. eaaw2871, 2019.
- [62] C. Huang, C. Zhang, S. Xiao, Y. Wang, Y. Fan, Y. Liu, N. Zhang, G. Qu, H. Ji, J. Han *et al.*, “Ultrafast control of vortex microlasers,” *Science*, vol. 367, no. 6481, pp. 1018–1021, 2020.
- [63] A. I. Kuznetsov, A. E. Miroshnichenko, M. L. Brongersma, Y. S. Kivshar, and B. Luk’yanchuk, “Optically resonant dielectric nanostructures,” *Science*, vol. 354, no. 6314, p. aag2472, 2016.
- [64] J. Van de Groep and A. Polman, “Designing dielectric resonators on substrates: Combining magnetic and electric resonances,” *Optics Express*, vol. 21, no. 22, pp. 26 285–26 302, 2013.
- [65] A. B. Evlyukhin, C. Reinhardt, and B. N. Chichkov, “Multipole light scattering by nonspherical nanoparticles in the discrete dipole approximation,” *Physical Review B*, vol. 84, no. 23, p. 235429, 2011.
- [66] V. E. Babicheva and J. V. Moloney, “Lattice effect influence on the electric and magnetic dipole resonance overlap in a disk array,” *Nanophotonics*, vol. 7, no. 10, pp. 1663–1668, 2018.
- [67] J. Li, N. Verellen, and P. Van Dorpe, “Engineering electric and magnetic dipole coupling in arrays of dielectric nanoparticles,” *Journal of Applied Physics*, vol. 123, no. 8, p. 083101, 2018.

- [68] Y. Yang, I. I. Kravchenko, D. P. Briggs, and J. Valentine, “All-dielectric meta-surface analogue of electromagnetically induced transparency,” *Nature Communications*, vol. 5, no. 1, pp. 1–7, 2014.
- [69] S. Campione, S. Liu, L. I. Basilio, L. K. Warne, W. L. Langston, T. S. Luk, J. R. Wendt, J. L. Reno, G. A. Keeler, I. Brener *et al.*, “Broken symmetry dielectric resonators for high quality factor Fano metasurfaces,” *Acs Photonics*, vol. 3, no. 12, pp. 2362–2367, 2016.
- [70] D. Wang, A. Yang, W. Wang, Y. Hua, R. D. Schaller, G. C. Schatz, and T. W. Odom, “Band-edge engineering for controlled multi-modal nanolasing in plasmonic superlattices,” *Nature Nanotechnology*, vol. 12, no. 9, p. 889, 2017.
- [71] Lumerical Inc. <http://www.lumerical.com/tcad-products/fdtd/>.
- [72] K. Yee, “Numerical solution of initial boundary value problems involving maxwell’s equations in isotropic media,” *IEEE Transactions on antennas and propagation*, vol. 14, no. 3, pp. 302–307, 1966.
- [73] S. Chang and A. Taflove, “Finite-difference time-domain model of lasing action in a four-level two-electron atomic system,” *Optics Express*, vol. 12, no. 16, pp. 3827–3833, 2004.
- [74] S. A. Maier, *Plasmonics: fundamentals and applications*. Springer Science & Business Media, 2007.
- [75] M. L. Brongersma and V. M. Shalaev, “The case for plasmonics,” *Science*, vol. 328, no. 5977, pp. 440–441, 2010.
- [76] M. I. Stockman, “The spaser as a nanoscale quantum generator and ultrafast amplifier,” *Journal of Optics*, vol. 12, no. 2, p. 024004, 2010.
- [77] M. Premaratne and M. I. Stockman, “Theory and technology of spasers,” *Advances in Optics and Photonics*, vol. 9, no. 1, pp. 79–128, 2017.
- [78] M. Noginov, V. A. Podolskiy, G. Zhu, M. Mayy, M. Bahoura, J. Adegoke, B. Ritzo, and K. Reynolds, “Compensation of loss in propagating surface plasmon polariton by gain in adjacent dielectric medium,” *Optics Express*, vol. 16, no. 2, pp. 1385–1392, 2008.
- [79] S. Wuestner, A. Pusch, K. L. Tsakmakidis, J. M. Hamm, and O. Hess, “Overcoming losses with gain in a negative refractive index metamaterial,” *Physical Review Letters*, vol. 105, no. 12, p. 127401, 2010.
- [80] D. J. Bergman and M. I. Stockman, “Surface plasmon amplification by stimulated emission of radiation: quantum generation of coherent surface plasmons in nanosystems,” *Physical Review Letters*, vol. 90, no. 2, p. 027402, 2003.
- [81] F. van Beijnum, P. J. van Veldhoven, E. J. Geluk, M. J. de Dood, W. Gert, and M. P. van Exter, “Surface plasmon lasing observed in metal hole arrays,” *Physical Review Letters*, vol. 110, no. 20, p. 206802, 2013.
- [82] M. Noginov, G. Zhu, A. Belgrave, R. Bakker, V. Shalaev, E. Narimanov, S. Stout, E. Herz, T. Suteewong, and U. Wiesner, “Demonstration of a spaser-based nanolaser,” *Nature*, vol. 460, no. 7259, p. 1110, 2009.

- [83] Z. Wang, X. Meng, A. V. Kildishev, A. Boltasseva, and V. M. Shalaev, "Nanolasers enabled by metallic nanoparticles: From spasers to random lasers," *Laser & Photonics Reviews*, vol. 11, no. 6, p. 1700212, 2017.
- [84] R. F. Oulton, V. J. Sorger, T. Zentgraf, R.-M. Ma, C. Gladden, L. Dai, G. Bartal, and X. Zhang, "Plasmon lasers at deep subwavelength scale," *Nature*, vol. 461, no. 7264, p. 629, 2009.
- [85] T. P. Sidiropoulos, R. Röder, S. Geburt, O. Hess, S. A. Maier, C. Ronning, and R. F. Oulton, "Ultrafast plasmonic nanowire lasers near the surface plasmon frequency," *Nature Physics*, vol. 10, no. 11, p. 870, 2014.
- [86] M. Khajavikhan, A. Simic, M. Katz, J. Lee, B. Slutsky, A. Mizrahi, V. Lomakin, and Y. Fainman, "Thresholdless nanoscale coaxial lasers," *Nature*, vol. 482, no. 7384, p. 204, 2012.
- [87] W. Zhou, M. Dridi, J. Y. Suh, C. H. Kim, D. T. Co, M. R. Wasielewski, G. C. Schatz, T. W. Odom *et al.*, "Lasing action in strongly coupled plasmonic nanocavity arrays," *Nature Nanotechnology*, vol. 8, no. 7, p. 506, 2013.
- [88] F. van Beijnum, P. J. van Veldhoven, E. J. Geluk, M. J. de Dood, W. Gert, and M. P. van Exter, "Surface plasmon lasing observed in metal hole arrays," *Physical Review Letters*, vol. 110, no. 20, p. 206802, 2013.
- [89] X. Meng, J. Liu, A. V. Kildishev, and V. M. Shalaev, "Highly directional spaser array for the red wavelength region," *Laser & Photonics Reviews*, vol. 8, no. 6, pp. 896–903, 2014.
- [90] R. Chandrasekar, Z. Wang, X. Meng, S. I. Azzam, M. Y. Shalaginov, A. Lagutchev, Y. L. Kim, A. Wei, A. V. Kildishev, A. Boltasseva *et al.*, "Lasing action with gold nanorod hyperbolic metamaterials," *ACS Photonics*, vol. 4, no. 3, pp. 674–680, 2017.
- [91] T. Pickering, J. M. Hamm, A. F. Page, S. Wuestner, and O. Hess, "Cavity-free plasmonic nanolasing enabled by dispersionless stopped light," *Nature communications*, vol. 5, p. 4972, 2014.
- [92] S. Wuestner, J. M. Hamm, A. Pusch, and O. Hess, "Plasmonic leaky-mode lasing in active semiconductor nanowires," *Laser & Photonics Reviews*, vol. 9, no. 2, pp. 256–262, 2015.
- [93] J. Vučković, M. Lončar, and A. Scherer, "Surface plasmon enhanced light-emitting diode," *IEEE Journal of Quantum Electronics*, vol. 36, no. 10, pp. 1131–1144, 2000.
- [94] A. Scherer, J. Vuckovic, and M. Loncar, "Surface plasmon enhanced light emitting diode and method of operation for the same," Mar. 18 2003, uS Patent 6,534,798.
- [95] H. R. Stuart, "Structure and method for processing optical energy," Dec. 28 2004, uS Patent 6,836,494.
- [96] J. Stehr, J. Crewett, F. Schindler, R. Sperling, G. Von Plessen, U. Lemmer, J. M. Lupton, T. A. Klar, J. Feldmann, A. W. Holleitner *et al.*, "A low threshold polymer laser based on metallic nanoparticle gratings," *Advanced Materials*, vol. 15, no. 20, pp. 1726–1729, 2003.

- [97] S. Azzam, N. Arnold, L. Prokopeva, Z. Kudyshev, and A. Kildishev, "Gain-assisted surface plasmon polaritons: Time domain analysis with experimentally fitted organic dye models," in *Frontiers in Optics*. Optical Society of America, 2016, pp. JW4A–132.
- [98] I. De Leon and P. Berini, "Amplification of long-range surface plasmons by a dipolar gain medium," *Nature Photonics*, vol. 4, no. 6, p. 382, 2010.
- [99] N. Meinzer, M. Ruther, S. Linden, C. M. Soukoulis, G. Khitrova, J. Hendrickson, J. D. Olitzky, H. M. Gibbs, and M. Wegener, "Arrays of ag split-ring resonators coupled to ingaas single-quantum-well gain," *Optics Express*, vol. 18, no. 23, pp. 24 140–24 151, 2010.
- [100] Z. Huang, T. Koschny, and C. M. Soukoulis, "Theory of pump-probe experiments of metallic metamaterials coupled to a gain medium," *Physical Review Letters*, vol. 108, no. 18, p. 187402, 2012.
- [101] S. Xiao, V. P. Drachev, A. V. Kildishev, X. Ni, U. K. Chettiar, H.-K. Yuan, and V. M. Shalaev, "Loss-free and active optical negative-index metamaterials," *Nature*, vol. 466, no. 7307, p. 735, 2010.
- [102] M. I. Stockman, "Spaser action, loss compensation, and stability in plasmonic systems with gain," *Physical Review Letters*, vol. 106, no. 15, p. 156802, 2011.
- [103] M. Dridi and G. C. Schatz, "Model for describing plasmon-enhanced lasers that combines rate equations with finite-difference time-domain," *JOSA B*, vol. 30, no. 11, pp. 2791–2797, 2013.
- [104] E. I. Smotrova, A. I. Nosich, T. M. Benson, and P. Sewell, "Cold-cavity thresholds of microdisks with uniform and nonuniform gain: quasi-3-d modeling with accurate 2-d analysis," *IEEE Journal of Selected Topics in Quantum Electronics*, vol. 11, no. 5, pp. 1135–1142, 2005.
- [105] A. Taflove and S. C. Hagness, *Computational electrodynamics: the finite-difference time-domain method*. Artech house, 2005.
- [106] T. Matsui and M. Kitaguchi, "Finite-difference time-domain analysis of laser action in cholesteric photonic liquid crystal," *Applied physics express*, vol. 3, no. 6, p. 061701, 2010.
- [107] A. Fang, T. Koschny, and C. M. Soukoulis, "Lasing in metamaterial nanostructures," *Journal of Optics*, vol. 12, no. 2, p. 024013, 2010.
- [108] A. Pusch, S. Wuestner, J. M. Hamm, K. L. Tsakmakidis, and O. Hess, "Coherent amplification and noise in gain-enhanced nanoplasmonic metamaterials: A maxwell-bloch langevin approach," *ACS Nano*, vol. 6, no. 3, pp. 2420–2431, 2012.
- [109] S. Wuestner, J. M. Hamm, A. Pusch, F. Renn, K. L. Tsakmakidis, and O. Hess, "Control and dynamic competition of bright and dark lasing states in active nanoplasmonic metamaterials," *Physical Review B*, vol. 85, no. 20, p. 201406, 2012.
- [110] S. Wuestner, T. Pickering, J. M. Hamm, A. F. Page, A. Pusch, and O. Hess, "Ultrafast dynamics of nanoplasmonic stopped-light lasing," *Faraday discussions*, vol. 178, pp. 307–324, 2015.

- [111] J. Trieschmann, S. Xiao, L. J. Prokopeva, V. P. Drachev, and A. V. Kildishev, "Experimental retrieval of the kinetic parameters of a dye in a solid film," *Optics Express*, vol. 19, no. 19, pp. 18 253–18 259, 2011.
- [112] B. Ding, C. Hrelescu, N. Arnold, G. Isic, and T. A. Klar, "Spectral and directional reshaping of fluorescence in large area self-assembled plasmonic–photonic crystals," *Nano Letters*, vol. 13, no. 2, pp. 378–386, 2013.
- [113] L. J. Prokopeva, J. D. Borneman, and A. V. Kildishev, "Optical dispersion models for time-domain modeling of metal-dielectric nanostructures," *IEEE Transactions on Magnetics*, vol. 47, no. 5, pp. 1150–1153, 2011.
- [114] X. Ni, Z. Liu, and A. Kildishev, "PhotonicsDB: Optical constants <http://nanohub.org/resources>," *PhotonicsDB* doi:(10.4231/D3FT8DJ4J), 2010.
- [115] P. B. Johnson and R.-W. Christy, "Optical constants of the noble metals," *Physical Review B*, vol. 6, no. 12, p. 4370, 1972.
- [116] L. Novotny and B. Hecht, *Principles of nano-optics*. Cambridge university press, 2012.
- [117] H. Raether, "Surface plasmons on gratings," in *Surface plasmons on smooth and rough surfaces and on gratings*. Springer, 1988, pp. 91–116.
- [118] R. C. Hollins, "Materials for optical limiters," *Current Opinion in Solid State and Materials Science*, vol. 4, no. 2, pp. 189–196, 1999.
- [119] B. N. S. B. P. Prem Kiran and D. N. Rao, "Nonlinear optical properties and surface-plasmon enhanced optical limiting in Ag–Cu nanoclusters co-doped in SiO₂ Sol-Gel films," *Journal of Applied Physics*, vol. 96, no. 11, pp. 6717–6723, 2004.
- [120] C. Li, L. Zhang, R. Wang, Y. Song, and Y. Wang, "Dynamics of reverse saturable absorption and all-optical switching in C₆₀," *JOSA B*, vol. 11, no. 8, pp. 1356–1360, 1994.
- [121] S. V. R. N. K. M. Naga Srinivas and D. N. Rao, "Saturable and reverse saturable absorption of Rhodamine B in methanol and water," *JOSA B*, vol. 20, no. 12, pp. 2470–2479, 2003.
- [122] L. W. Tutt and S. W. McCahon, "Reverse saturable absorption in metal cluster compounds," *Optics Letters*, vol. 15, no. 12, pp. 700–702, 1990.
- [123] U. Gurudas, E. Brooks, D. M. Bubb, S. Heiroth, T. Lippert, and A. Wokaun, "Saturable and reverse saturable absorption in silver nanodots at 532 nm using picosecond laser pulses," *Journal of Applied Physics*, vol. 104, no. 7, p. 073107, 2008.
- [124] W. Blau, H. Byrne, W. Dennis, and J. Kelly, "Reverse saturable absorption in tetraphenylporphyrins," *Optics Communications*, vol. 56, no. 1, pp. 25–29, 1985.

- [125] X. Sun, Y. Xiong, P. Chen, J. Lin, W. Ji, J. H. Lim, S. S. Yang, D. J. Hagan, and E. W. Van Stryland, "Investigation of an optical limiting mechanism in multiwalled carbon nanotubes," *Applied Optics*, vol. 39, no. 12, pp. 1998–2001, 2000.
- [126] Q. Ouyang, H. Yu, H. Wu, Z. Lei, L. Qi, and Y. Chen, "Graphene/MoS₂ organic glasses: Fabrication and enhanced reverse saturable absorption properties," *Optical Materials*, vol. 35, no. 12, pp. 2352–2356, 2013.
- [127] Z. Cheng, H. Li, H. Shi, J. Ren, Q.-H. Yang, and P. Wang, "Dissipative soliton resonance and reverse saturable absorption in graphene oxide mode-locked all-normal-dispersion Yb-doped fiber laser," *Optics Express*, vol. 23, no. 6, pp. 7000–7006, 2015.
- [128] S. Hirata, K. Totani, T. Yamashita, C. Adachi, and M. Vacha, "Large reverse saturable absorption under weak continuous incoherent light," *Nature Materials*, vol. 13, no. 10, pp. 938–946, 2014.
- [129] S. Hirata and M. Vacha, "Large reverse saturable absorption at the sunlight power level using the ultralong lifetime of triplet excitons," *The Journal of Physical Chemistry Letters*, vol. 8, no. 15, pp. 3683–3689, 2017.
- [130] M. Miscuglio, A. Mehrabian, Z. Hu, S. I. Azzam, J. George, A. V. Kildishev, M. Pelton, and V. J. Sorger, "All-optical nonlinear activation function for photonic neural networks," *Optical Materials Express*, vol. 8, no. 12, pp. 3851–3863, 2018.
- [131] C. Varin, G. Bart, R. Emms, and T. Brabec, "Saturable lorentz model for fully explicit three-dimensional modeling of nonlinear optics," *Optics Express*, vol. 23, no. 3, pp. 2686–2695, 2015.
- [132] W. S. S. C. Hill, G. Videen and Q. Fu, "Scattering and internal fields of a microsphere that contains a saturable absorber: finite-difference time-domain simulations," *Applied Optics*, vol. 40, no. 30, pp. 5487–5494, 2001.
- [133] A. Mock, "Modeling passive mode-locking via saturable absorption in graphene using the finite-difference time-domain method," *IEEE Journal of Quantum Electronics*, vol. 53, no. 5, pp. 1–10, 2017.
- [134] J. Trieschmann, S. Xiao, L. J. Prokopeva, V. P. Drachev, and A. V. Kildishev, "Experimental retrieval of the kinetic parameters of a dye in a solid film," *Optics Express*, vol. 19, no. 19, pp. 18 253–18 259, Sep 2011.
- [135] G. Y. Yang, M. Hanack, Y. W. Lee, Y. Chen, M. K. Y. Lee, and D. Dini, "Synthesis and nonlinear optical properties of fluorine-containing naphthalocyanines," *Chemistry—A European Journal*, vol. 9, no. 12, pp. 2758–2762, 2003.
- [136] D. J. H. D. I. Kovsh, S. Yang and E. W. V. Stryland, "Nonlinear optical beam propagation for optical limiting," *Applied Optics*, vol. 38, no. 24, pp. 5168–5180, 1999.
- [137] D. J. H. R. Lepkowicz, A. Kobayakov and E. W. V. Stryland, "Picosecond optical limiting in reverse saturable absorbers: a theoretical and experimental study," *JOSA B*, vol. 19, no. 1, pp. 94–101, 2002.

- [138] A. S. Nagra and R. A. York, "FDTD analysis of wave propagation in nonlinear absorbing and gain media," *IEEE Transactions on Antennas and Propagation*, vol. 46, no. 3, pp. 334–340, 1998.
- [139] S.-H. Chang and A. Taflov, "Finite-difference time-domain model of lasing action in a four-level two-electron atomic system," *Optics Express*, vol. 12, no. 16, pp. 3827–3833, 2004.
- [140] B. R. Masters, "Principles of fluorescence spectroscopy," *Journal of Biomedical Optics*, vol. 13, no. 2, p. 029901, 2008.
- [141] Q. Bao, H. Zhang, Y. Wang, Z. Ni, Y. Yan, Z. X. Shen, K. P. Loh, and D. Y. Tang, "Atomic-layer graphene as a saturable absorber for ultrafast pulsed lasers," *Advanced Functional Materials*, vol. 19, no. 19, pp. 3077–3083, 2009.
- [142] S. Yamashita, Y. Inoue, S. Maruyama, Y. Murakami, H. Yaguchi, M. Jablonski, and S. Set, "Saturable absorbers incorporating carbon nanotubes directly synthesized onto substrates and fibers and their application to mode-locked fiber lasers," *Optics Letters*, vol. 29, no. 14, pp. 1581–1583, 2004.
- [143] C. Zhao, H. Zhang, X. Qi, Y. Chen, Z. Wang, S. Wen, and D. Tang, "Ultra-short pulse generation by a topological insulator based saturable absorber," *Applied Physics Letters*, vol. 101, no. 21, p. 211106, 2012.
- [144] H. Ahmad, C. Lee, M. Ismail, Z. Ali, S. Reduan, N. Ruslan, M. Ismail, and S. Harun, "Zinc oxide (ZnO) nanoparticles as saturable absorber in passively q-switched fiber laser," *Optics Communications*, vol. 381, pp. 72–76, 2016.
- [145] D. Wu, J. Peng, Z. Cai, J. Weng, Z. Luo, N. Chen, and H. Xu, "Gold nanoparticles as a saturable absorber for visible 635 nm q-switched pulse generation," *Optics Express*, vol. 23, no. 18, pp. 24 071–24 076, 2015.
- [146] S. C. Hill, G. Videen, W. Sun, and Q. Fu, "Scattering and internal fields of a microsphere that contains a saturable absorber: finite-difference time-domain simulations," *Applied optics*, vol. 40, no. 30, pp. 5487–5494, 2001.
- [147] Y. Feng, N. Dong, G. Wang, Y. Li, S. Zhang, K. Wang, L. Zhang, W. J. Blau, and J. Wang, "Saturable absorption behavior of free-standing graphene polymer composite films over broad wavelength and time ranges," *Optics Express*, vol. 23, no. 1, pp. 559–569, 2015.
- [148] C. Varin, R. Emms, G. Bart, T. Fennel, and T. Brabec, "Explicit formulation of second and third order optical nonlinearity in the fdtd framework," *Computer Physics Communications*, vol. 222, pp. 70–83, 2018.
- [149] A. Mock, "Modeling passive mode-locking via saturable absorption in graphene using the finite-difference time-domain method," *IEEE Journal of Quantum Electronics*, vol. 53, no. 5, pp. 1–10, 2017.

APPENDICES

A. APPENDIX I

A.1 Silver optical properties

The dielectric function of sputtered polycrystalline silver on a glass substrate is retrieved from variable angle spectroscopic ellipsometry measurement (WVASE, J. A. Woollam Co., Inc.) as shown in Fig. A1. The tabulated data is fitted using multi-coefficient models (MCMs) in Lumerical FDTD [71] to allow efficient incorporation of Ag optical dispersion in the time-domain solver.

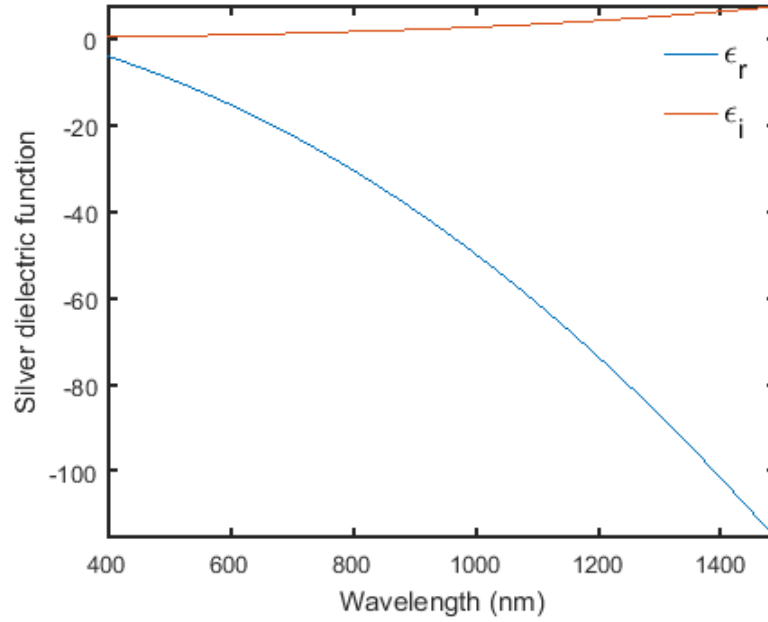


Fig. A.1. Real and imaginary parts of the polycrystalline silver permittivity as a function of the wavelength.

A.2 Numerical details

A commercial solver based on the finite-difference time-domain method is used to perform the calculations [71]. Our simulations are two-dimensional (2D) with the Bloch boundary conditions in the y -direction and perfectly matched layers (PML) along the x -direction to ensure absorption of outgoing radiated waves, see Fig. A2. The structure is illuminated with a broadband plane-wave light source incident at an angle (θ). Electric field direction is determined based on the required polarization to provide transverse electric (TE) across the grating or transverse magnetic (TM) along the grating wires.

A.3 Nature of supported modes

In this section, we simulate different variations of the structure studied in the main text to explore the nature of the interacting modes further and to confirm our results. First, the band-diagram of the silver grating covered with an extended dielectric layer is calculated and depicted in Fig. A3. Due to the absence of the mode hybridization and the strong coupling, the band-diagram of this structure shows only the dispersion of the plasmonic branch that partially appeared in the hybridized structure band-diagram. Moreover, the band-diagram of the primary studied structure consisting of a silver grating coupled to a 500-nm SiO₂ waveguide under not only TM polarized light illumination but also TE is shown in Fig. A4. In the TE case, the sharp photonic modes supported by the waveguide are excited by the additional momentum provided by the grating. Still, no hybridization is present in the system because TE polarized light cannot excite the plasmonic modes. Field distributions in the structure at an angle of incidence of 2° at six different resonances are shown in Fig. A4. All field plots confirm that only photonic modes of different orders are excited, and no plasmonic modes are present.

Furthermore, we study a titanium oxide (TiO₂) grating, with the same dimensions as silver one, on top of a 100-nm silver film coupled to a 500-nm SiO₂ waveguide.

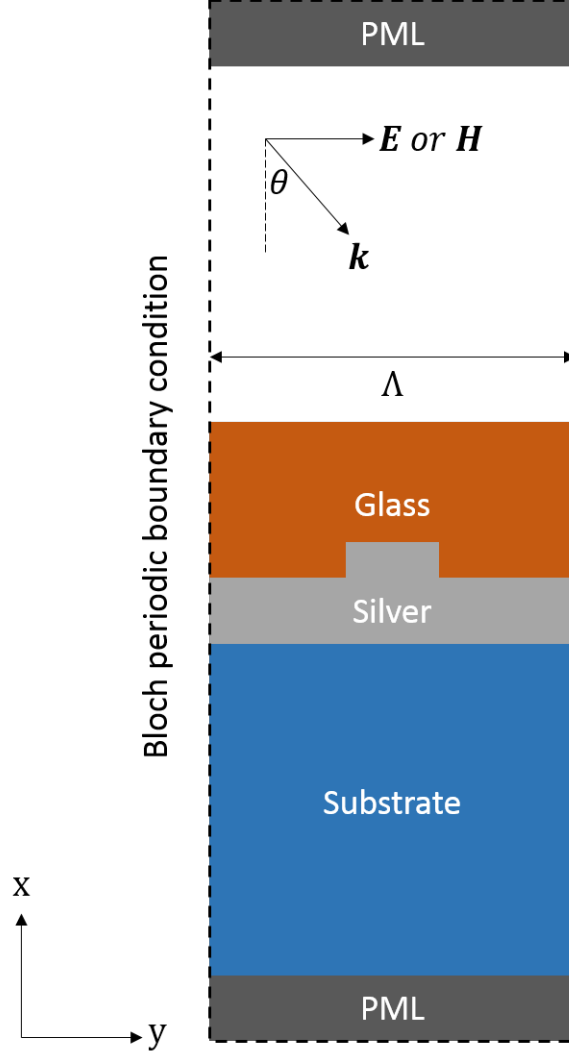


Fig. A.2. Cross-section of the hybrid plasmonic-photonic structure in the simulation domain. The simulation implements the Bloch periodic boundary conditions in the y -direction and PML in the x -direction. Dimensions are specified in the main text.

The band-diagrams under TE and TM polarizations are shown in Fig. A5. In Fig. A4(a) we can clearly observe the differences between the band-diagram under TM illumination when the metallic grating is replaced by a dielectric one. Only photonic modes, with the help of the momenta provided by the grating, are excited due to the absence of plasmonic modes. On the contrary, the band-diagrams under TE

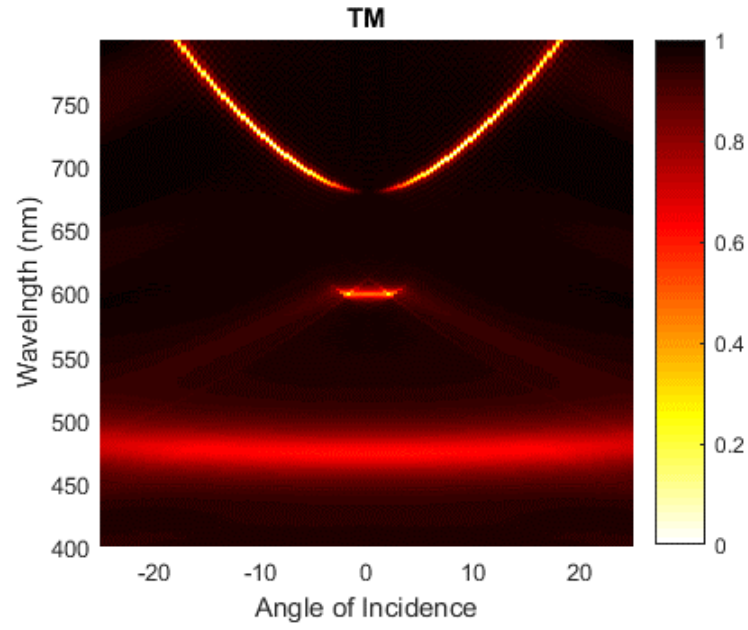


Fig. A.3. Band-diagram of the silver grating with extended SiO₂ top layer.

polarized light with both metal and dielectric gratings are, as expected, very similar due to the excitation of photonic modes only.

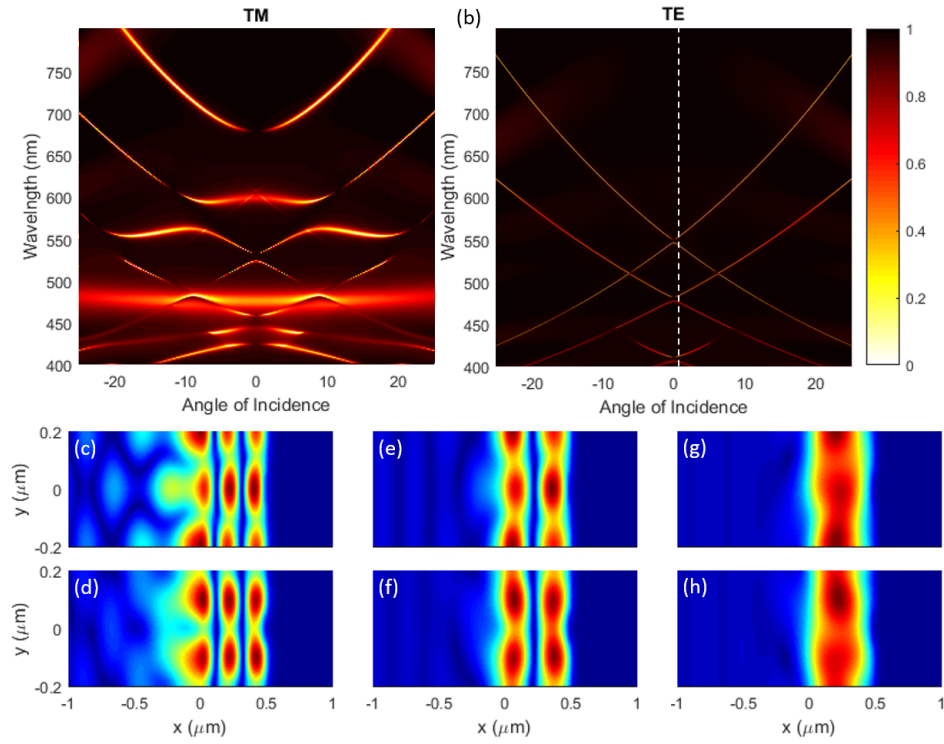


Fig. A.4. Band diagram of the hybrid silver grating-silica waveguide system under (a) TM and (b) TE light illumination. Plots of the electric field under TE illumination at the locations highlighted in (b) at an angle of incidence of 2° and wavelengths of (c) 405.6 nm, (d) 413.4 nm, (e) 475.1 nm, (f) 485.3 nm, (g) 541.6 nm, (h) 555.2 nm.

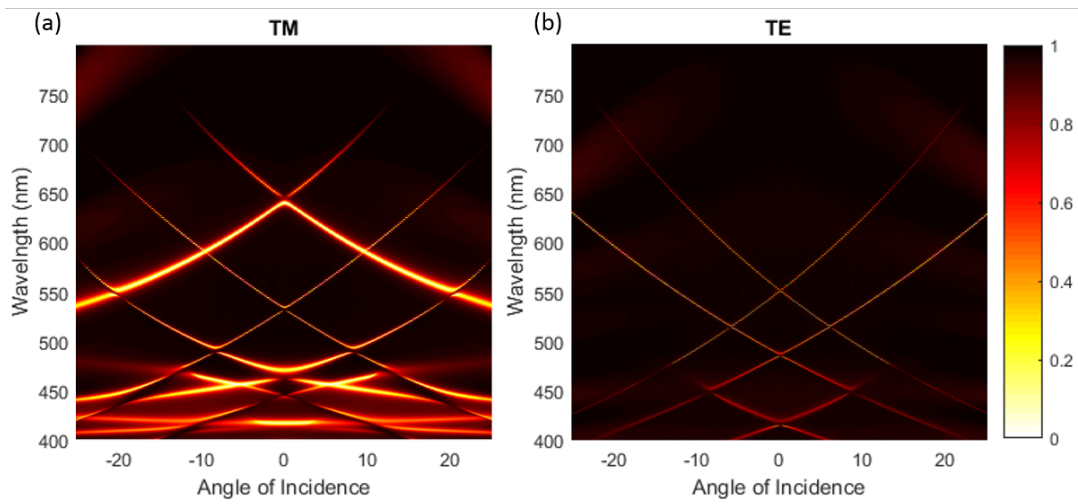


Fig. A.5. Band-diagram of a TiO₂ grating on top of a 100-nm silver film coupled to a 500-nm SiO₂ waveguide under (a) TM and (b) TE illumination. For the TiO₂ grating the same dimensions are used as for the Ag grating.

B. APPENDIX II

B.1 Nature of the supported modes in the metasurface

Simulated reflectance of a metasurface with a radius of 100 nm at normal incidence is shown in Figure B.1. At normal incidence, three resonances are observed in the reflectance spectrum, and the vector plots of electric fields show the nature of these modes. Current loops at 645.9 nm and 579.4 nm confirm the formation of magnetic dipole and quadrupole, respectively. At 621.4 nm shows the resonance is due to an electric dipole. While symmetry-protected BIC points will not appear at normal incidence, we can observe the quasi-BIC resonances under angled-illumination. Figure B.1(A) shows the reflectance spectrum of a metasurface with a radius of 100 nm at incidence angle of 2° . The resonances at 621.5 nm and 644 nm are due to electric and magnetic dipoles whilst the sharp resonance appearing at 686.3 nm is the quasi-BIC state. Cross sections of the absolute electric fields at the different resonances are given in Fig. B.2 showing the horizontal and vertical confinements at the different spectral points.

B.2 Dependence of the Electric Dipole, Magnetic Dipole and the BIC State on the Geometrical Parameters

To further investigate the nature of the dipole modes, their interplay, and how this interplay affects the BICs, we performed parametric sweeps on some of the geometrical parameters of the metasurface array. Figure B.3 shows the reflectance spectra as a function of the nanoresonator height at different values of the radius. Varying the height of the single resonator manipulates the spectral position and width of the electric and magnetic dipole modes, and the electric quadrupole mode, as can be seen

in Fig. B.3 . Moreover, similar to what we reported on in the main manuscript, symmetry-protected BIC can be observed not only with varying the radius but also the height of the single resonator, as can be noted from Fig. B.3 (B).

B.3 FDTD simulations of lasing dynamics

We utilize an in-home built framework of a multi-level system [23–25] incorporated in a commercial software finite difference time domain (FDTD) solver [71] to model nonlinear light-matter interactions [72, 73]. The multi-level framework allows for capturing the behavior of the gain materials embedded in photonic nanostructures and have accurate estimate of their threshold and spectral response. In this work, the gain medium (Rhodamine 101) is modeled using a four-level system, and the electromagnetic waves are treated classically with Maxwell’s equations [23]. The four-level atomic system used is depicted in Fig.B.5.

The rate equations describing the transition and pumping dynamics in the four-level system are given by:

$$\frac{dN_3}{dt} = -\frac{N_3}{\tau_{32}} + \frac{1}{\hbar\omega_{30}} \mathbf{E} \cdot \frac{d\mathbf{P}_{30}}{dt} \quad (\text{B.1a})$$

$$\frac{dN_2}{dt} = -\frac{N_2}{\tau_{21}} - \frac{N_3}{\tau_{32}} + \frac{1}{\hbar\omega_{21}} \mathbf{E} \cdot \frac{d\mathbf{P}_{21}}{dt} \quad (\text{B.1b})$$

$$\frac{dN_1}{dt} = -\frac{N_1}{\tau_{10}} + \frac{N_2}{\tau_{21}} + \frac{1}{\hbar\omega_{21}} \mathbf{E} \cdot \frac{d\mathbf{P}_{21}}{dt} \quad (\text{B.1c})$$

where N_3 , N_2 , are N_1 are the population density of carriers in the different energy levels. The total carrier density, N_d , is conserved such that $N_d = N_3 + N_2 + N_1 + N_0$ at any time and space point. The lifetimes of the transition between energy level $|i\rangle$ to level $|j\rangle$ is given by τ_{ij} which are shown in Figure B.5. The energies between levels $|3\rangle$ and $|0\rangle$ corresponds to the angular frequency ω_{30} and that between $|1\rangle$ and $|2\rangle$ corresponds to ω_{21} . The term $\frac{1}{\hbar\omega_0} \mathbf{E} \cdot \frac{\partial \mathbf{P}_{ij}}{\partial t}$ represents the coherent emission and

absorption between levels $|i\rangle$ and $|j\rangle$. The induced macroscopic polarizations due to the transitions satisfy the Lorentz ordinary differential equation given by:

$$\frac{\partial^2 \mathbf{P}_{ij}}{\partial t^2} + \gamma_{ij} \frac{\partial \mathbf{P}_{ij}}{\partial t} + \omega_{ij}^2 \mathbf{P}_{ij} = \kappa_{ij} (N_j - N_i) \mathbf{E} \quad (\text{B.2})$$

where γ_{ij} is the dephasing constant between levels $|i\rangle$ and $|j\rangle$. The source term in Eq. (B.2) is proportional to product of the local electric field and the difference in populations between the upper and the lower levels of this transition with a proportionality constant κ_{ij} where $ij \in \{30, 21\}$. The coupling coefficient κ_{ij} represents the dipole matrix element between levels $|i\rangle$ and $|j\rangle$ and is given by $\kappa_{ij} = 2\omega_{ij}|\mu_{ij}|^2/\hbar = 6\pi\epsilon_0 c^3/\omega_{ij}^2 \tau_{ij}$, where ϵ_0 and c are the free space permittivity and speed of light, respectively, and τ_{ij} is the decay time constant between levels $|i\rangle$ and $|j\rangle$ [73, 138].

The polarization densities are then coupled to the Maxwell equations through the electric flux using equations:

$$\nabla \times \mathbf{H}(t, \mathbf{r}) = \epsilon_0 \epsilon_h \frac{\partial \mathbf{E}(t, \mathbf{r})}{\partial t} + \frac{\partial \mathbf{P}(t, \mathbf{r})}{\partial t}, \quad (\text{B.3})$$

$$\nabla \times \mathbf{E}(t, \mathbf{r}) = -\mu_0 \frac{\partial \mathbf{H}(t, \mathbf{r})}{\partial t}, \quad (\text{B.4})$$

where μ_0 is the permeability of free space. Eqs. (B.1)-(B.4) are solved simultaneously using a full-wave solver on a staggered Yee grid by applying the classical finite-difference approximation to the spatial and time derivatives [72, 73]. The time-dependent electromagnetic fields are recorded and converted to the frequency domain using fast Fourier transform to obtain the transmission and reflection coefficients. In this study, we use experimentally-extracted model parameters for the R101 gain medium with a concentration of 10 mM: $n_h = 1.45$, $\lambda_{30} = 575$ nm, $\lambda_{21} = 605$ nm, $T_2^{30} = 9$ fs, $T_2^{21} = 25.5$ fs, $\tau_{30} = 5$ ns, $\tau_{32} = 0.3$ ps, $\tau_{21} = 3.3$ ns, and $\tau_{10} = 0.35$ ps. As evident from the results in the main manuscript, simulated and experimental data of the lasing spectra and threshold are in excellent agreement.

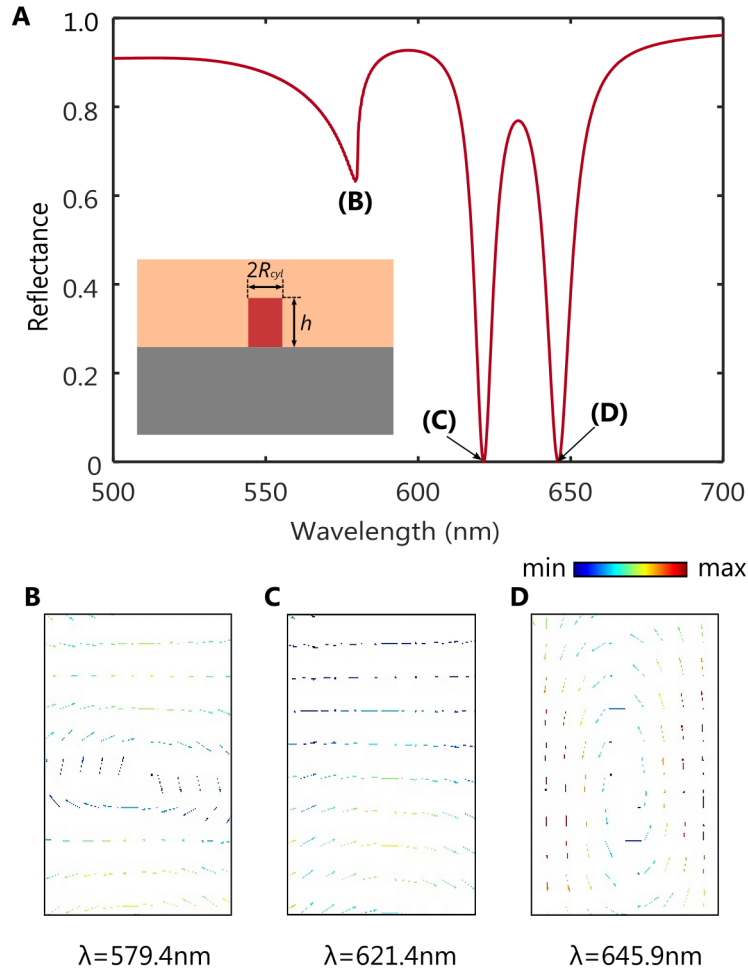


Fig. B.1. A) Simulated reflectance of a metasurface with a radius of 100 nm at normal incidence. The inset shows a schematic of the cross section of a unit cell. (B-D) Vector plots of the electric field inside a cross section of the nanoresonator at the different reflectance dips indicated in (A). Displacement current loops in (B) 579.4 nm and (D) 645.9 nm confirm the formation of magnetic quadrupole and dipole, respectively. (C) At 621.4 nm an electric dipole mode is formed.

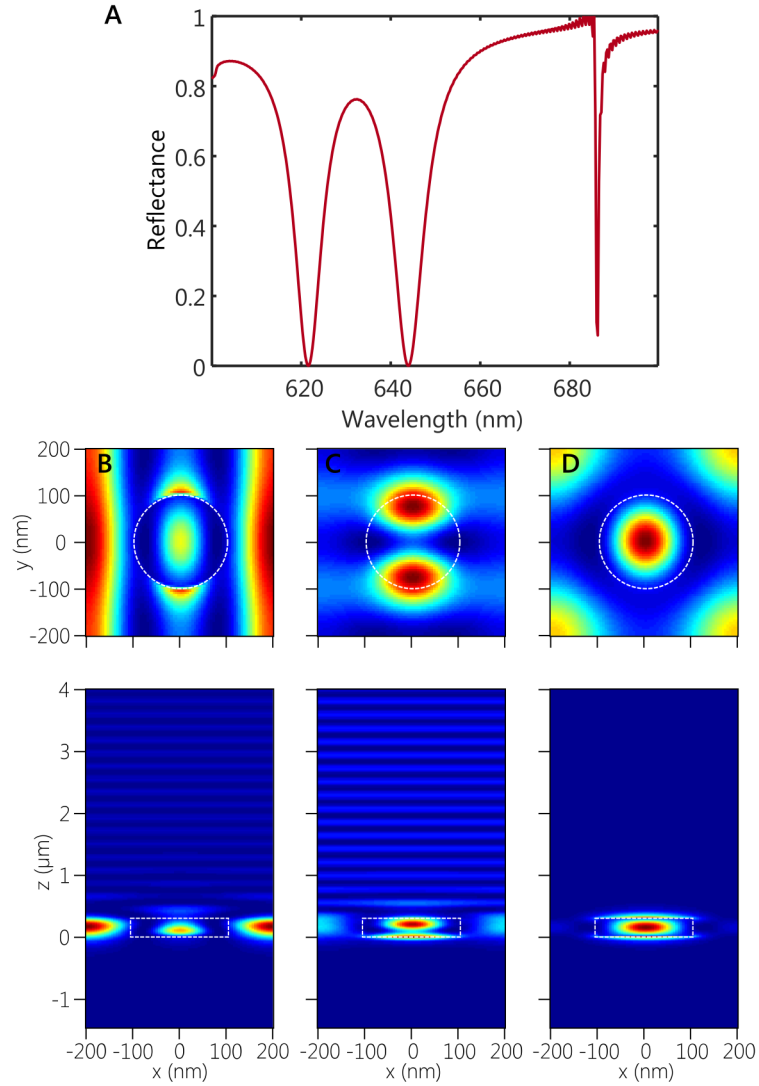


Fig. B.2. Nature of electromagnetic fields at the different modes supported by the metasurface. A) Simulated reflectance of a metasurface with $R_{cyl} = 100$ nm at an incidence angle of 2° . Horizontal (top) and vertical (bottom) cross-sections of the electric field at B) 621.5 nm, C) 644 nm, and D) 686.3 nm.

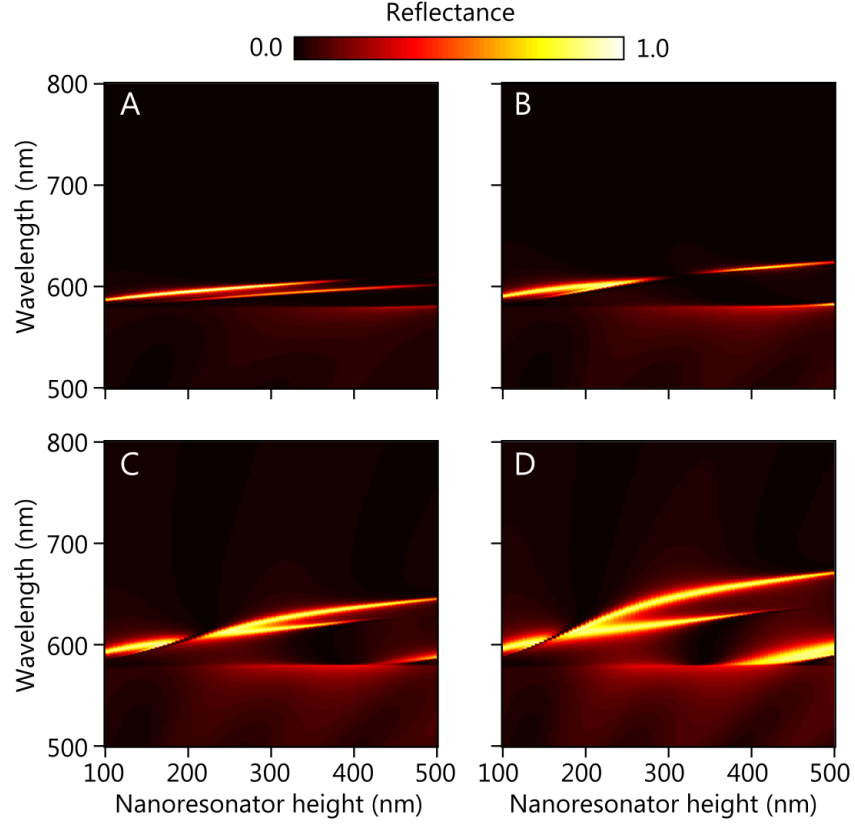


Fig. B.3. Simulated reflectance spectra of the metasurface with an array periodicity of 400 nm vs. the resonator height, with R_{cyl} of (A) 70 nm, (B) 81 nm, (C) 90 nm, and (D) 100 nm.

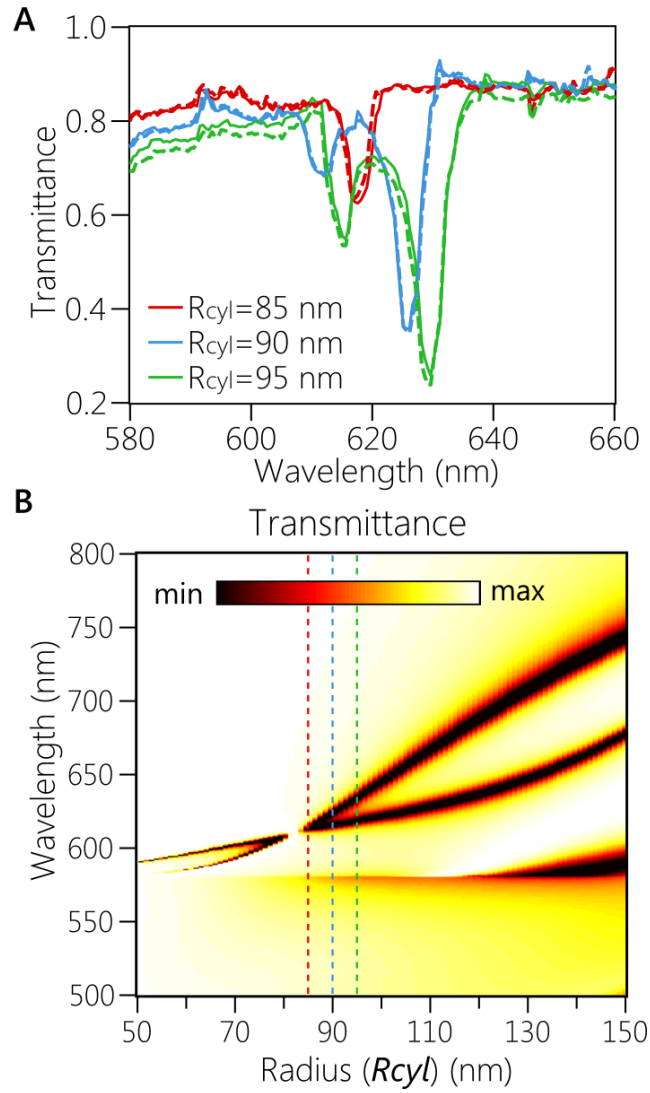


Fig. B.4. A) Transmittance of three samples with R_{cyl} of 85, 90 and 95 nm at normal incidence. Solid lines correspond to p -polarized light and dashed ones correspond to s -polarized light. B) Simulated transmittance as a function of R_{cyl} and wavelength. Dashed lines are color-coded to correspond to the measurements in (A).

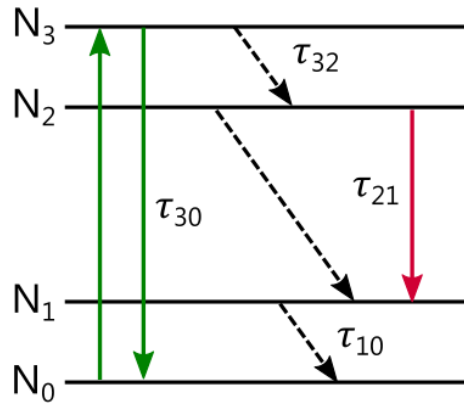


Fig. B.5. Jablonski diagram of a four-level gain medium. Solid lines indicate stimulated transmissions (absorption and emission) and dashed lines represent non-radiative transitions.

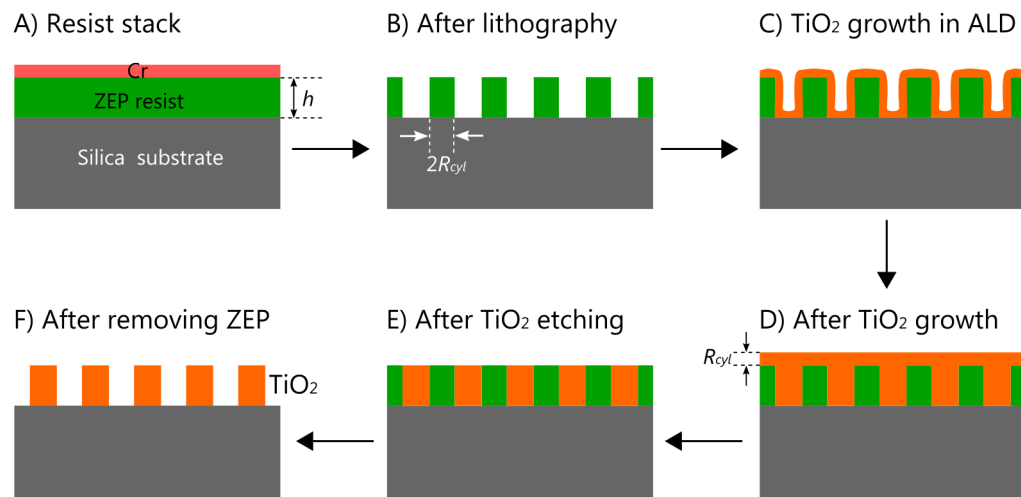


Fig. B.6. Schematic showing the different steps of the fabrication process of the metasurfaces. The process flow starts from (A) through (F).

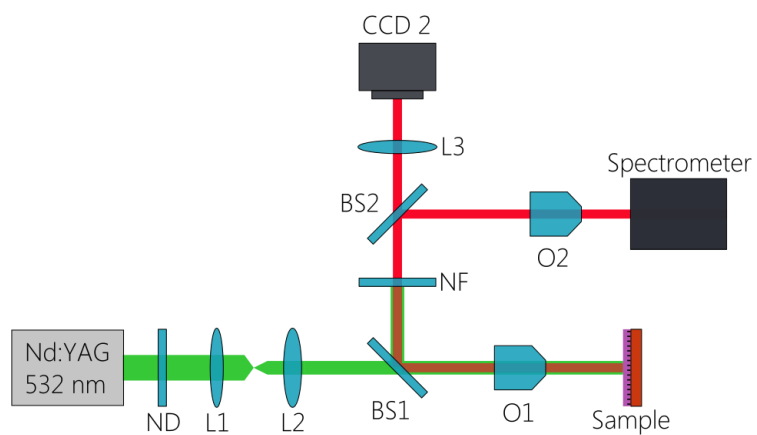


Fig. B.7. Schematic of the experimental setup used to collect the lasing emission from the metasurface samples.

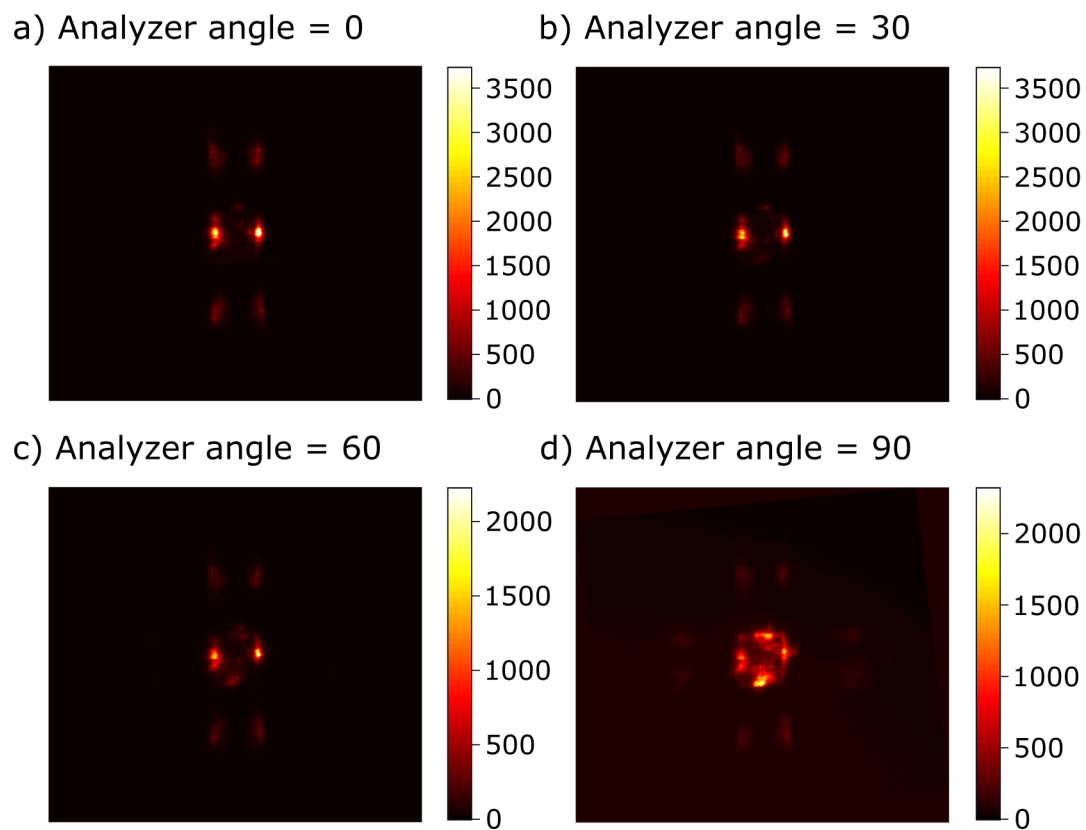


Fig. B.8. Back focal plane images at analyzer angles of (a) 0°, (b) 30°, (c) 60° and (d) 90°.

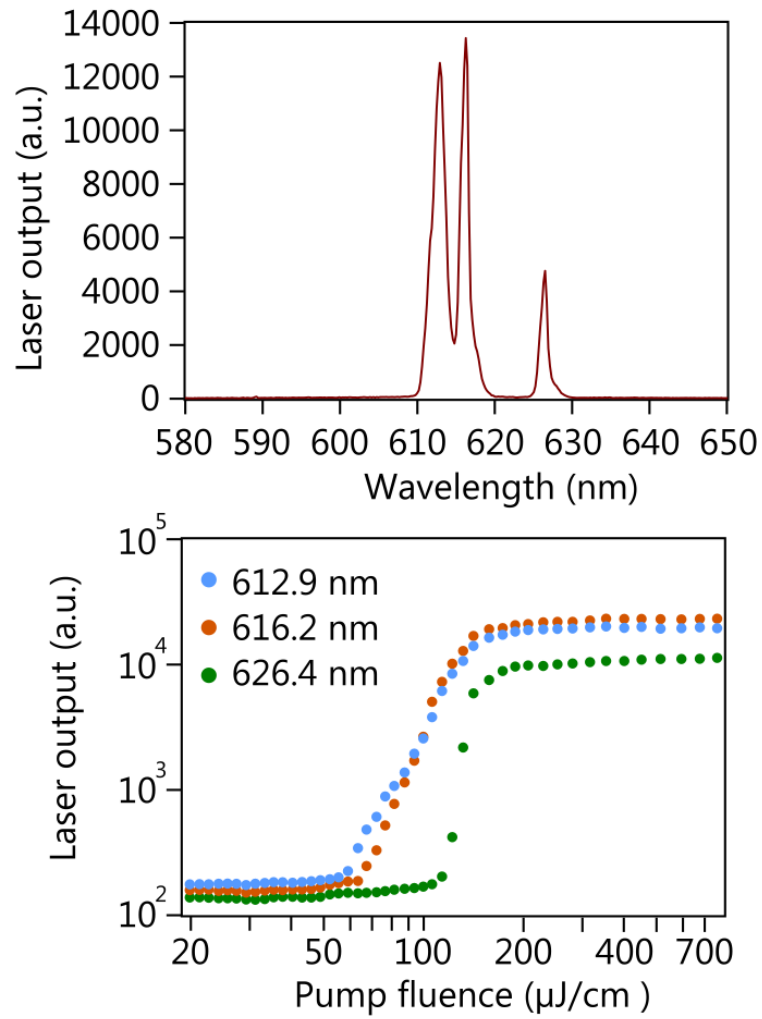


Fig. B.9. Triple-mode lasing with a BIC metasurface feedback. (Top) Laser output of an active metasurface showing three lasing peaks at 612.9 nm, 616.2 nm, and 624.4 nm. (Bottom) Evolution of each lasing peak with the pump fluence showing a sharp threshold behavior for each lasing wavelength.

VITA

VITA

Shaimaa Azzam received her bachelor's degree in Electronics and Communications Engineering from Mansoura University – Egypt in 2011. She received her master's degree in Electrical Engineering also from Mansoura University in 2014. Shaimaa joined the nanophotonics group at Purdue University in the Spring of 2016 as a Meissner PhD Fellow, where she worked on her PhD degree in nanophotonics. Her work at Purdue has focused on the modeling and optimization of the nonlinear phenomenon in nanophotonics devices. She also focused on the design and demonstration of nano- and micro-scale coherent light sources known as nanolasers. During her PhD, Shaimaa has won multiple awards and scholarships including the 2020 Outstanding Graduate Student Research Award from the College of Engineering, Purdue University and the 2019 Bilsland Dissertation Fellowship, Purdue University. Shaimaa will be joining the University of California, Santa Barbara as the Elings Prize Postdoctoral fellow to pursue her postdoctoral research.

PUBLICATIONS

PUBLICATIONS

1. **S. I. Azzam**, K. Chaudhuri, A. Lagutchev, Z. Jacob, Y. L. Kim, V. M. Shalaev, A. Boltasseva, and A. V. Kildishev, "Single and multi-mode directional lasing from arrays of dielectric nanoresonators," [arXiv:2006.16473] (2020).
2. Z. Wang, **S. I. Azzam**, X. Meng, M. Alhabeb, K. Chaudhuri, K. Maleski, Y. L. Kim, A. V. Kildishev, V. M. Shalaev, Y. Gogotsi, and A. Boltasseva, "Active metamaterials based on monolayer titanium carbide MXene for dynamic controlled random lasing," *Opt. Mater. Express*, In press (2020).
3. **S. I. Azzam**, A. V. Kildishev, R-M Ma, C-Z Ning, R. F. Oulton, V. M. Shalaev, M. I. Stockman, J-L Xu, and X. Zhang, "Ten Years of SPASERs and Plasmonic Nanolasers," *Light: Science & Applications* **9**, 90 (2020).
4. K. Chaudhuri, U. Guler, **S. I. Azzam***, H. Reddy, S. Saha, E. E. Marinero, A. V. Kildishev, V.M. Shalaev, and A. Boltasseva, "Remote sensing of high temperatures with refractory, direct-contact optical metacavity," *ACS Photonics* **7**, 472 (2020).
5. S. Murai, S. Oka, **S. I. Azzam**, A. V. Kildishev, S. Ishii, and K. Tanaka, "Enhanced absorption and photoluminescence from dye-containing thin polymer film on plasmonic array," *Opt. Express* **27**, 5083 (2019).
6. **S. I. Azzam**, J. Fang, J. Liu, Z. Wang, N. Arnold, T. A. Klar, L. J. Prokopeva, X. Meng, V. M. Shalaev, and A. V. Kildishev, "Exploring time-resolved multi-physics of active plasmonic systems with experiment-based gain models," *Laser Photonics Rev.* **13**, 1800071 (2019).

7. **S. I. Azzam** and A. V. Kildishev, “Time domain dynamics of reverse saturable absorbers with application to plasmon-enhanced optical limiters,” *Nanophotonics* **8**, 145 (2018).
8. **S. I. Azzam**, V. M. Shalaev, A. Boltasseva, and A. V. Kildishev, “Formation of bound states in the continuum in hybrid plasmonic-photonic systems,” *Phys. Rev. Lett.* **121**, 253901 (2018). [arXiv:1808.08244]
9. **S. I. Azzam** and A. V. Kildishev, “Time-domain dynamics of saturation of absorption using multilevel atomic systems,” *Opt. Mater. Express* **8**, 3829 (2018).
10. M. Miscuglio, A. Mehrabian, Z. Hu, **S. I. Azzam**, J. George, A. V. Kildishev, M. Pelton, and V. J. Sorger, “All-optical nonlinear activation function for photonic neural networks [Invited],” *Opt. Mater. Express* **8**, 3851 (2018).
11. W. Sabra, **S. I. Azzam**, M. Song, M. Povolotskyi, A. H. Aly And A. V. Kildishev, “Plasmonic metasurfaces for subtractive color filtering: Optimized nonlinear regression models,” *Opt. Lett.* **43**, 4815 (2018).
12. R. Chandrasekar, Z. Wang, X. Meng, **S. I. Azzam**, M. Y. Shalaginov, A. Lagutchev, Y. L. Kim A. Wei, A. V. Kildishev, A. Boltasseva, and V. M. Shalaev, “Lasing action with gold nanorod hyperbolic metamaterials,” *ACS Photonics* **4**, 674 (2017).
13. M. F. O. Hameed, R. Zaghoul, **S. I. Azzam**, and S. S. A. Obayya, “Ultra-short hybrid plasmonic transverse electric pass polarizer for silicon-on-insulator platform,” *Opt. Eng.* **56**, 017107 (2017).
14. **S. I. Azzam**, M. F. O. Hameed, R. E. Shehata, A. M. Heikal, and S. S. A. Obayya, “Multichannel photonic crystal fiber surface plasmon resonance based sensor,” *Opt. Quant. Electron.* **48**, 142 (2016).
15. **S. I. Azzam** and S. S. A. Obayya. “Titanium nitride-based CMOS-compatible TE-pass and TM-pass plasmonic polarizers,” *IEEE Photon. Technol. Lett.* **28**, 367 (2016).

16. **S. I. Azzam** and S. S. A. Obayya, “Ultra-compact resonant tunneling-based TE-pass and TM-pass polarizers for SOI platform,” *Opt. Lett.* **40**, 1061 (2015).
17. **S. I. Azzam**, M. A. Swillam, and S. S. A. Obayya, “Analysis of plasmonic effects in silicon nanoholes,” *Opt. Eng.* **53**, 107103 (2014).
18. **S. I. Azzam**, M. F. O. Hameed, N. F. Areed, M. M. Abd-Elrazzak, H. A. El-Mikaty, and S. S. A. Obayya, “Proposal of an ultracompact CMOS-compatible TE-/TM-pass polarizer based on SOI platform,” *IEEE Photon. Technol. Lett.* **26**, 1633 (2014).